

INFORMATION TO USERS

This manuscript has been reproduced from the microfilm master. UMI films the text directly from the original or copy submitted. Thus, some thesis and dissertation copies are in typewriter face, while others may be from any type of computer printer.

The quality of this reproduction is dependent upon the quality of the copy submitted. Broken or indistinct print, colored or poor quality illustrations and photographs, print bleedthrough, substandard margins, and improper alignment can adversely affect reproduction.

In the unlikely event that the author did not send UMI a complete manuscript and there are missing pages, these will be noted. Also, if unauthorized copyright material had to be removed, a note will indicate the deletion.

Oversize materials (e.g., maps, drawings, charts) are reproduced by sectioning the original, beginning at the upper left-hand corner and continuing from left to right in equal sections with small overlaps. Each original is also photographed in one exposure and is included in reduced form at the back of the book.

Photographs included in the original manuscript have been reproduced xerographically in this copy. Higher quality 6" x 9" black and white photographic prints are available for any photographs or illustrations appearing in this copy for an additional charge. Contact UMI directly to order.

UMI

A Bell & Howell Information Company
300 North Zeeb Road, Ann Arbor, MI 48106-1346 USA
313:761-4700 800:521-0600

**On the Simulation and Modeling of Turbulent
Reacting Flows**

by

Andrew W. Cook

A dissertation submitted in partial fulfillment of
the requirements for the degree of

Doctor of Philosophy

University of Washington

1996

Approved by _____

James A. Reay

(Chairperson of Supervisory Committee)

Program Authorized

to Offer Degree _____

MECHANICAL ENGINEERING

Date _____

5 AUGUST 1996

UMI Number: 9704480

**Copyright 1996 by
Cook, Andrew William**

All rights reserved.

**UMI Microform 9704480
Copyright 1996, by UMI Company. All rights reserved.**

**This microform edition is protected against unauthorized
copying under Title 17, United States Code.**

UMI
300 North Zeeb Road
Ann Arbor, MI 48103

© Copyright 1996
Andrew W. Cook

In presenting this dissertation in partial fulfillment of the requirements for the Doctoral degree at the University of Washington, I agree that the Library shall make its copies freely available for inspection. I further agree that extensive copying of this dissertation is allowable only for scholarly purposes, consistent with "fair use" as prescribed in the U.S. Copyright Law. Requests for copying or reproduction of this dissertation may be referred to University Microfilms, 1490 Eisenhower Place, P.O. Box 975, Ann Arbor, MI 48106, to whom the author has granted "the right to reproduce and sell (a) copies of the manuscript in microform and/or (b) printed copies of the manuscript made from microform."

Signature Andrew Cook

Date 8/5/96

University of Washington

Abstract

On the Simulation and Modeling of Turbulent Reacting Flows

by Andrew W. Cook

Chairperson of Supervisory Committee: *Prof. James J. Riley*

Mechanical Engineering

A computational algorithm is described for Direct Numerical Simulation (DNS) of a reactive plume in spatially-evolving, grid turbulence. The chemistry follows the single-step, irreversible, global reaction: $Fuel + (r)Oxidizer \rightarrow (1+r)Product + Heat$, with parameters chosen to match experimental data as far as allowed by resolution constraints. Simulation results are presented for four different cases in order to examine the effects of heat release, Damköhler number, and Arrhenius kinetics on the flow physics. Statistical data from the DNS are compared to theory and wind tunnel data and found in reasonable agreement with regard to growth of turbulent length scales, decay of turbulent kinetic energy, decay of centerline scalar concentration, decrease in scalar rms and spread of plume profile. Reactive scalar statistics are consistent with expected behavior.

In addition to the DNS, models are presented for use in Large Eddy Simulations (LES) of non-premixed, turbulent reacting flows. A new chemistry model is derived for predicting filtered chemical species and/or reaction rates. The model is based on laminar flamelet theory and assumes that the subgrid or 'Large Eddy' Probability Density Function (LEPDF) of the mixture-fraction follows a Beta-distribution. The

functional form of the scalar dissipation rate is obtained by assuming that the instantaneous local straining fields in the neighborhood of the reaction zones are laminar counterflows. Inputs to the model are the filtered mixture-fraction, its subgrid-scale variance and filtered dissipation rate. The model is evaluated by filtering DNS data to simulate the results of an LES. The DNS data show that the model is reasonably accurate and that the accuracy improves with increasing Damköhler number. Furthermore, as the activation temperature is increased, the accuracy of the model improves relative to that for a model assuming equilibrium chemistry. Finally, it is demonstrated that the assumed counterflow form for the scalar dissipation rate is acceptable and that the chemistry model is insensitive to whether or not unmixed fuel and/or oxidizer are present within an LES grid cell.

TABLE OF CONTENTS

List of Figures	iv
List of Tables	vi
Chapter 1: Introduction	1
1.1 Direct Numerical Simulation	1
1.2 Large Eddy Simulation	6
Chapter 2: Governing Equations	10
2.1 Flow Configuration	10
2.2 Nondimensionalization	11
2.3 Conservation Laws	13
2.4 Scalar Based Chemistry	14
2.5 Low Mach Number Approximation	15
I Numerical Simulations	18
Chapter 3: Numerical Algorithm	19
3.1 Third Order Adams-Bashforth Scheme	19
3.2 Pressure Projection Method	21
3.3 Sixth Order Compact Scheme	22
3.4 Boundary Conditions	23
3.4.1 Inlet	24

3.4.2	Exit	24
3.5	Conservation Checks	26
3.6	Stability	27
3.7	Parallel Computing	28
3.7.1	Optimization	28
3.7.2	Performance	29
Chapter 4:	Results	31
4.1	Simulation Parameters	31
4.2	Visualization	34
4.3	Turbulent Flow Field	34
4.4	Plume	46
4.5	Reactive Scalar	50
4.6	Extinction	54
II	Subgrid-Scale Modeling	56
Chapter 5:	Derivation of Resolvable Field Equations	57
5.1	Filtering	57
5.2	The Large-Eddy Equations	59
5.3	Closure	62
5.3.1	Modeling the Subgrid-Scale Stress Tensor	63
5.3.2	Constraint on Eddy Viscosity	66
5.3.3	Subgrid-Scale Models for Heat Flux and Scalar Transport . . .	66
Chapter 6:	Derivation of Subgrid-Scale Chemistry Model	69
6.1	Reaction Zones	69

6.2	Laminar Flamelet Model	70
6.3	Counterflow Model	71
6.4	The Case of Unity Lewis Number	72
6.5	The Large Eddy Probability Density Function	73
6.6	Modeling the Scalar Variance and Dissipation Rate	75
6.7	Summary of Methodology	77
Chapter 7: Evaluation of Subgrid-Scale Chemistry Model		79
7.1	Filtered DNS Data	79
7.2	Isothermal Turbulence	81
7.3	The Effect of Arrhenius Kinetics	83
7.4	The Dependence of χ on ξ	88
7.5	Sources of Error	89
Chapter 8: Conclusions		95
8.1	Plume Simulations	95
8.2	Chemistry Model for LES	97
8.3	Future Work	98
Bibliography		100

LIST OF FIGURES

2.1	Schematic of flow geometry.	10
3.1	3-D energy and dissipation spectra of inlet turbulence.	25
4.1	Contours of density, vorticity-magnitude, mixture-fraction and reaction rate on a centerline slice from case D.	35
4.2	Gray-scale contours of mixture-fraction on various cross-stream cuts, taken from case A.	36
4.3	Two dimensional total energy spectra at various downstream locations.	37
4.4	Longitudinal velocity autocorrelations from case A.	38
4.5	Mean density vs downstream distance.	40
4.6	Density fluctuations vs downstream distance.	41
4.7	Taylor microscales vs distance downstream.	42
4.8	Centerline decay of turbulent kinetic energy.	44
4.9	Taylor Reynolds numbers vs distance downstream.	45
4.10	Mean mixture fraction along centerline.	47
4.11	RMS of mixture fraction along centerline.	48
4.12	Standard deviation of mean scalar profile vs large eddy turnover time.	49
4.13	Mean and limiting values of fuel mass fraction along centerline.	51
4.14	Fluctuation of fuel mass fraction along centerline.	52
4.15	Mean centerline reaction rate.	53
4.16	Proximity of reaction at stoichiometric locations to the extinction limit. Data taken from case D.	55

6.1	Probability Density Functions of angle between scalar gradient vector and most compressive strain axis (θ) and angle between scalar gradient and most extensional axis (ϕ).	70
7.1	Correlation of exact and model species mass-fractions for case T1. . .	82
7.2	Correlation of exact and model species mass-fractions for case T2. . .	84
7.3	Correlation of exact and model species mass-fractions for case T3. . .	85
7.4	Correlation of exact and modeled values for product and reaction rate at various activation temperatures.	86
7.5	Comparison of the counterflow model for χ and the Beta model for the LEPDF with data from DNS cases T1 and T2.	90
7.6	Performance of equilibrium chemistry model at various stoichiometries.	93

LIST OF TABLES

4.1	Comparison of flow parameters from the wind tunnel experiment of Brown and Bilger and from the DNS case A	32
4.2	Parameters that varied from case to case in the numerical simulations	33
7.1	Turbulence and chemistry parameters of filtered DNS data fields. . .	80
7.2	Slope of straight line corresponding to least squares fit of the data for cases T4, T5 and T6.	87
7.3	Scatter of data about a straight-line fit for cases T4, T5 and T6. . . .	87

ACKNOWLEDGMENTS

This work was partially supported by a National Science and Engineering Graduate Fellowship and by NSF under grant number CTS-9415280. The simulations described herein were performed on the Connection Machine Model-5 (CM-5) at the National Center for Supercomputing Applications, University of Illinois at Urbana-Champaign. Additionally, I wish to thank Dr. D. N. Slinn for advice on the coding, Dr. W. E. Mell for use of his isothermal data fields, soon-to-be-Dr. V. Nilsen for custom making some 256^3 point velocity fields, Dr. D. L. Sandoval for discussions about density and for introducing me to Los Alamos National Lab., will-someday-be-Dr. S. de Bruyn Kops for fixing the computers, Prof. G. Kosály for his guidance and for reasoning through some half-baked schemes, Prof. R. E. Breidenthal for etching key formulas into the frontal lobes of my brain, and Prof. J. J. Riley for his tutelage, and for responding calmly when confronted with hare-brained ideas. Most of all I wish to thank my wife Ann for her patience, love and support throughout this endeavor.

Chapter 1

INTRODUCTION

1.1 *Direct Numerical Simulation*

Turbulent reacting flows occur in a wide variety of atmospheric, oceanic and biological processes and hence have generated a great deal of scientific interest. Furthermore, the need to predict the combustion efficiency and pollutant formation in a wide variety of man-made devices, from power plants to jet engines, has driven the development of various methods for computing turbulent flows with chemical reactions. The Reynolds number of flows of scientific and engineering interest is often very high; however, many physical phenomena in these flows are also observed in flows at low Reynolds number. Therefore, it is useful and practical to study turbulent reacting flows at lower Reynolds numbers, since such flows can be computed by Direct Numerical Simulation (DNS). In DNS, the exact governing equations are solved in order to gain insight into the turbulence and combustion phenomena. In performing a DNS, it is important to select the proper numerical method for treating the flow of interest. Since turbulent flows contain a wide range of length scales, spectral methods are a natural choice for DNS due to their high accuracy and their ability to correctly represent a broad range of wavenumbers. The application of spectral methods to turbulent reacting flows was initiated by Riley *et al.* [82] and was continued by McMurtry *et al.* [59], Givi *et al.* [36], Leonard and Hill [46] and others.

Spectral methods are usually employed by expanding the dependent variables in truncated series of orthogonal basis functions satisfying the required boundary conditions. Spatial derivatives are evaluated locally in the transformed domain, while nonlinear products are evaluated locally in the physical domain. The most common expansion used is Fourier series, although Chebyshev polynomials, Legendre polynomials, Jacobi polynomials and other series have sometimes been employed [40]. With Fourier and Chebyshev expansions, the mapping between physical space and spectral space can be performed efficiently using a Fast Fourier Transform (FFT) algorithm. Spectral methods have the advantages that phase errors are very small and rates of convergence are very high. They are also at least twice as accurate in each spatial dimension as typical finite-difference schemes using the same resolution [39], [74]. One drawback of spectral methods is that the class of complete basis functions, which allow matching the boundary conditions and also possess the properties of rapid convergence, is limited. The application of Fourier series is restricted to problems with periodic or free-slip boundary conditions. Chebyshev polynomials can be applied to problems with arbitrary boundary conditions but the distribution of collocation points for the method may not be ideal for many problems. Spectral methods are thus limited in their ability to treat common boundary conditions, e.g., inflow/outflow, although work on the spectral element method [43], [34] has made significant progress in removing this limitation. If spectral methods are applied to flows containing shocks, then the computational grid must be locally refined in order to fully resolve the discontinuity, otherwise Gibb's phenomenon will act to degrade the solution.

Finite-difference methods, on the other hand, have the advantage of easy application to all types of boundary conditions. They may be constructed to arbitrarily high orders of accuracy, albeit with increasing computational cost; hence, second and fourth-order schemes are most commonly used in computing complex flowfields. In

addition, finite-difference schemes have been developed which eliminate spurious oscillations around a shock without the need for smearing the discontinuity over several grid points. For example, Total Variation Diminishing (TVD) schemes [94] use a “smart” artificial viscosity which is small in regions of smooth flow but which grows at a discontinuity. The growth of the artificial viscosity near the shock reduces the scheme to first order locally, thereby preventing oscillations.

In treating turbulent reacting flows with heat release it is desirable to have at least one open boundary [38] so that the flow may expand due to chemical heat release [13], [71]. Otherwise, the temperature and pressure in the domain will continually increase and affect the rate of chemical reaction and hence the turbulence [59], [68]. This means that a method must be chosen which can accurately resolve the wide range of length scales of the turbulent field, but which can handle open boundary conditions. The Compact (Pade) scheme fits both these requirements and therefore is a good choice for computing these types of flows. The sixth-order version of the Compact scheme, in particular, provides a high degree of numerical accuracy at a low computational cost. The global nature of the Compact scheme makes it necessary to use accurate boundary conditions. Boundary conditions which may seem suitable with low order schemes (with built-in dissipation) may not perform well with Compact differencing. The Compact scheme is known to work well with nonreflecting boundary conditions [76] which may be used in conjunction with the compressible Navier-Stokes equations. Chen *et al.* [13] used nonreflecting boundary conditions in one direction of an otherwise periodic domain in order to simulate temporally decaying turbulence with an exothermic chemical reaction. Since combustion often occurs at low speeds, a low Mach number approximation is often applied to the fully-compressible Navier-Stokes equations in order to increase the maximum stable time step. The resulting equations are elliptic and nonreflecting inflow/outflow conditions can no longer be applied to such flows. One objective of the present work is to demonstrate the stability

of the Compact scheme with the turbulent inflow/outflow conditions described herein.

Compact schemes have a pure central difference form (except near the boundaries), and thus have no built-in artificial dissipation. This means that they should only be applied to flows where the shortest length scales are determined physically and not numerically, i.e., the solution should be smooth. With finite difference schemes, dispersion errors, resulting from inadequate resolution, show up in local oscillations near a shock or discontinuity. Since the Compact scheme is a global scheme, however, inadequate resolution in one part of the domain can contaminate the solution everywhere; the same is true for spectral schemes. However, with adequate resolution, the Compact scheme is suitable for high Mach number flows and has been used to investigate shock wave structure [50] and to predict shocklet formation in temporally decaying turbulence [48].

In simulating spatially developing turbulence, it is desirable to introduce a fully-developed turbulent field at the inlet. Otherwise a lengthy computational region is necessary for instabilities to grow and eventually develop into turbulent flow far downstream [11], [96]. Lee *et al.* [49] introduced a method for generating a turbulent-like flow at the inlet in which the energy spectrum of a flow variable is prescribed in terms of frequency and two transverse wave numbers. The Fourier coefficients are written in terms of the prescribed spectrum and a random phase factor. The fluctuation signal is then obtained by inverse Fourier transforms in the homogeneous (transverse) directions, followed by a sum over all frequencies. In order that the signal be nonperiodic, the phase factors are changed once in a given time interval at a random instance and by a random amount. Changing the phase factors causes the generated signal to be discontinuous in time and the frequency spectrum of the turbulence signal to differ from the target spectrum. Furthermore, the incoming flow must undergo some adjustment before the turbulence becomes fully developed. Le

and Moin [47] used a modified version of Lee's method to simulate a turbulent, wall-bounded flow over a backward-facing step. Friedrich and Arnal [29] used a different approach in their Large Eddy Simulations (LES) of turbulent flow over a backstep. They first performed a preliminary LES of fully developed channel flow with periodic boundary conditions in the streamwise direction. In the preliminary simulation, they chose a plane perpendicular to the mean flow and stored the velocity vector in that plane for all time-steps needed. The stored data were then used as inflow conditions for the backward-facing step flow. A primary motivation for the present work is to test an alternative methodology for introducing a turbulent flow at the inlet. The particular flow under investigation is a reactive plume in spatially-evolving grid turbulence. The grid turbulence is specified at the inlet by literal application of Taylor's hypothesis [91] in which a frozen turbulent field is scanned at a rate equal to the mean streamwise velocity.

In the present simulations, a local source of fuel and a coflow of oxidizer are introduced at the inlet along with a fully-developed turbulent field. The turbulent flow is designed to match wind tunnel experiments of a plume in grid-generated turbulence. Such experiments have been performed by Mickelsen [65], Gad-el-Hak and Morton [30], Nakamura, Sakai and Miyata [70], and Brown and Bilger [8]. The fuel reacts with the oxidizer and releases heat as the reactants and product are carried downstream. The nature of the computational algorithm, along with the large memory requirements of the flow configuration, make this problem a good candidate for parallel execution. Hence, a secondary goal of this work is to address key issues involved in parallelizing a DNS code for turbulent reacting flows. In Chapter 2 the flow geometry is described and the governing equations are derived. In Chapter 3 the numerical algorithm is presented in detail, including a description of the inlet boundary condition where the turbulence is introduced. Issues related to parallelizing the code are also addressed. In Chapter 4 a comparison is made between the flow parameters of the

DNS and the wind tunnel experiment of Brown and Bilger. Attention is given to the limits of DNS for matching 'real-world' flows. Results are presented for the velocity and chemical fields and comparisons are made with various theories and experimental data in order to test the validity of the DNS results. The effectiveness of the current scheme for computing spatially-developing, turbulent, reacting flows is also discussed.

1.2 Large Eddy Simulation

DNS cannot be applied to turbulent reactive flows at high Reynolds numbers due to the limited resolution available on any computational mesh. The need to treat high Reynolds number flows has led to the practice of Reynolds averaging, whereby the governing equations are ensemble averaged and solved for mean flow quantities. Averaging in this manner introduces extra 'Reynolds-stress' terms that must be modeled. The Reynolds-stress terms contain the full range of turbulent length and time scales and are difficult to model, since the large scales of turbulence depend on the particular flow configuration. This difficulty, along with the need for time-accurate information in areas such as weather prediction, has spawned the development of Large Eddy Simulation (LES), whereby the scales of motion not resolvable on the computational mesh are spatially filtered from the equations of motion. Applying a filter to the Navier-Stokes equations produces equations analogous to the Reynolds-averaged equations, only the extra terms now represent the effects of subgrid-scale motions. Models are proposed for the subgrid-scale terms and the equations are solved for the resolvable scales of motion (the large eddies). This approach, introduced by Lilly [52] and Deardorff [21], has led to considerable success in the study of a wide variety of problems [89], ranging from channel flows [66] to atmospheric boundary layer flows [22], [84].

There is strong incentive to apply LES to reacting flows due to the importance of the problem and since it is the large eddies that set the rate of mixing and therefore

the overall rate of product formation. The largest, mixing-controlling eddies in a turbulent flow contain most of the turbulent kinetic energy and their size and rotation rate depend on the particular flow configuration; on the other hand, the small eddies contain only a tiny portion of the total energy, are more isotropic than the large eddies, and are thus thought to be more universal in nature. LES is expected to be more accurate than calculations employing the Reynolds-averaged equations since the large scales are treated directly. However, there is a difficulty in extending LES to chemically-reacting flows, since, for moderate to fast reaction rates, the scale of the entire flame lies below the grid scale; hence it is necessary to model the reactions in their entirety.

Some work has been initiated utilizing LES in the study of non-premixed, turbulent, reacting flows [57], [64]. McMurtry *et al.* [60] applied the *Linear Eddy* model of Kerstein [41] as a subgrid-scale model in a two-dimensional LES of a turbulent shear layer. At each point in the flow, the model, which consists of a Monte-Carlo solution to a one-dimensional advection, mixing, and reaction model, is used to simulate the reaction on the subgrid scale. The Monte-Carlo simulations occur independently of the LES, thus an *ad-hoc* method must be used to relate the subgrid-scale computations to the large-scale fields. However, results indicate that much of the physics are being properly treated. The large computational overhead of the *Linear Eddy* model makes it impractical to implement in a three-dimensional LES, at least at the present time. An alternative approach to subgrid-scale chemistry modeling has been put forth by Gao and O'Brien [31] who formulated the equation for the Large Eddy Probability Density Function (LEPDF) of the reactant concentrations. The LEPDF equation provides theoretical insights into various effects on subgrid-scale chemistry; however, it appears difficult to solve. The solution to the equation for the LEPDF may require Monte-Carlo methods, as does the equation for the full PDF [77], and in fact the model of Kerstein could be considered as a candidate for this approach.

A successful subgrid-scale chemistry model should be computationally feasible and should directly relate the subgrid-scale statistics to the computed fields. The Laminar Flamelet Model (LFM) of Peters' [73] relates chemical species to a conserved scalar mixture-fraction. Once combined with the LEPDF of the mixture-fraction, it may be used to predict filtered chemical species and filtered reaction rates in a turbulent flow. Rather than solving an equation for the LEPDF, it may be obtained by assuming a functional form based on the first two moments of a conserved scalar [93] [28]. The assumed LEPDF approach has been demonstrated to be a viable method for LES with equilibrium chemistry [16]. Errors in the assumed form are greatly reduced upon integration (a necessary part of the modeling) to obtain the filtered chemical species [4], [45]. Frankel *et. al.* [28] showed that assumed PDF methods could be effectively used in LES of non-premixed, turbulent, reacting flows with both equilibrium and finite-rate chemistry. In treating non-equilibrium chemistry, Frankel *et. al.* employed the joint Beta distribution for the fuel and oxidizer in a reacting flow with single step chemistry. This approach requires modeling of the subgrid-scale species covariance which may be somewhat difficult to obtain. In this dissertation, finite-rate chemistry is accounted for by utilizing the filtered scalar dissipation rate, a quantity for which models are available [87], [35].

In Chapter 5 the large eddy equations are derived and models given for the subgrid-scale stress tensor as well as the subgrid-scale heat and scalar flux vectors. The models presented represent a summary of recent extensions and improvements to Germano's dynamic model [32]. In Chapter 6 a model is derived that accounts for subgrid-scale chemical reactions in an LES of nonpremixed, turbulent, reacting flow. The chemistry model uses Laminar Flamelet Theory along with assumed forms for the LEPDF and dissipation rate of a mixture-fraction. The model is termed the Large Eddy Laminar Flamelet Model (LELFM). Chapter 7 examines the accuracy of the LELFM for both isothermal and temperature dependent chemistry. The assumed counterflow form for

the scalar dissipation rate is also examined by filtering DNS data. Finally, Chapter 8 gives conclusions regarding strengths and limitations of DNS and LES applied to turbulent reacting flows. Based on the findings of this thesis, suggestions are made for future research into turbulent reacting flows.

Chapter 2

GOVERNING EQUATIONS

2.1 Flow Configuration

This Chapter lays down the nomenclature and governing equations for the flow of interest. The flow to be treated, via DNS, is that of a plume reacting in grid turbulence at low Mach number. The fuel is introduced as a small circular source with a rounded, approximately tophat profile located at the center of the inlet. The reaction progresses downstream as the turbulence decays. The numerical resolution consists of 512 points in the streamwise direction, with 128 points in each of the transverse directions. The flow is periodic at the cross-stream boundaries with inflow and outflow conditions in the streamwise direction; figure 2.1 shows the flow geometry.

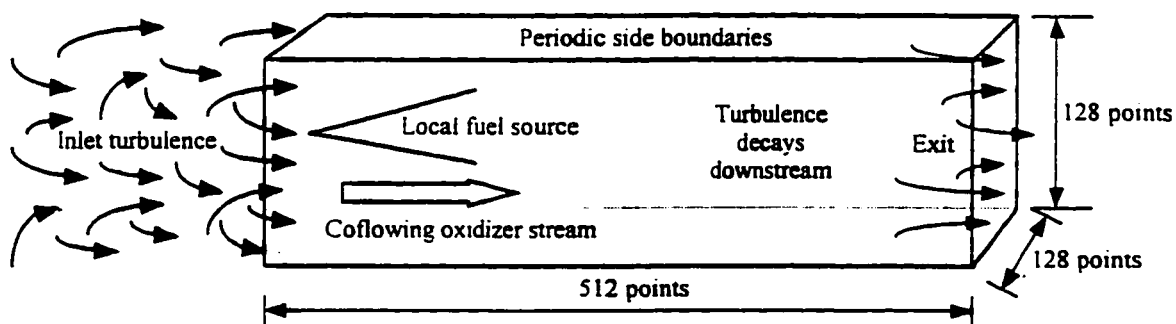


Figure 2.1: Schematic of flow geometry.

2.2 Nondimensionalization

In this work, a superscript \star denotes a dimensional quantity while a subscript ∞ denotes a free-stream or reference quantity (also dimensional). Subscripts f, o, and p denote the fuel, oxidizer, and product, respectively, in the single-step global reaction: $Fuel + (r)Oxidizer \rightarrow (1+r)Product + Heat$. Here r is the mass of oxidizer required to react with a unit mass of fuel. Reference and nondimensional quantities are defined as follows:

$$L_\infty \equiv \text{width of flow domain}$$

$$\rho_\infty \equiv \text{density at inlet}$$

$$U_\infty \equiv \text{mean streamwise velocity at inlet}$$

$$\mu_\infty \equiv \text{dynamic viscosity at inlet}$$

$$D_\infty \equiv \text{reference diffusivity}$$

$$T_\infty \equiv \text{temperature at inlet}$$

$$R_\infty \approx R_u^\star \sum_{i=1}^N \frac{Y_i}{W_i^\star} \equiv \text{mass-based ideal gas constant}$$

$$k^\star \equiv \text{thermal conductivity}$$

$$K^\star \equiv \text{reaction rate coefficient (depends on } Y_{f1} \text{ and } Y_{o2})$$

$$R_u^\star \equiv \text{universal gas constant}$$

$$E_a^\star \equiv \text{activation energy}$$

$$W_i^\star \equiv \text{molecular weight of species } i$$

$$x_i \equiv \frac{x_i^\star}{L_\infty} = \text{nondimensional distance in } i\text{th-direction}$$

$$t \equiv \frac{U_\infty t^\star}{L_\infty} = \text{nondimensional time}$$

$$\rho \equiv \frac{\rho^\star}{\rho_\infty} = \text{nondimensional density}$$

$$u_i \equiv \frac{u_i^*}{U_\infty} = \text{ith component of nondimensional velocity vector } \vec{u}$$

$$p \equiv \frac{p^*}{\rho_\infty U_\infty^2} = \text{nondimensional pressure}$$

$$T \equiv \frac{T^*}{T_\infty} = \text{nondimensional temperature}$$

$$\mu \equiv \frac{\mu^*}{\mu_\infty} = \text{nondimensional dynamic viscosity}$$

$$D_i \equiv \frac{D_i^*}{D_\infty} = \text{nondimensional diffusivity of species } i$$

$$T_a \equiv \frac{E_a^*}{R_u^* T_\infty} = \text{nondimensional activation temperature}$$

$$E \equiv \frac{p}{\rho(\gamma - 1)} + \frac{u_j u_j}{2} = \text{nondimensional total energy per unit volume}$$

$$Y_i \equiv \text{mass fraction of species } i$$

$$Y_{f1} \equiv \text{mass fraction of fuel in fuel stream}$$

$$Y_{o2} \equiv \text{mass fraction of oxidant in oxidizer stream}$$

$$\gamma \equiv \frac{c_p^*}{c_v^*} = \text{ratio of specific heats}$$

$$h_i \equiv \frac{h_i^*}{R_\infty T_\infty} = \text{nondimensional enthalpy of formation of species } i$$

$$M \equiv \frac{U_\infty}{\sqrt{\gamma R_\infty T_\infty}} = \text{Mach number}$$

$$Re \equiv \frac{\rho_\infty U_\infty L_\infty}{\mu_\infty} = \text{Reynolds number}$$

$$Pr \equiv \frac{c_p^* \mu^*}{k^*} = \text{Prandtl number (assumed constant)}$$

$$Sc \equiv \frac{\mu_\infty}{\rho_\infty D_\infty} = \text{Schmidt number}$$

$$Da \equiv \frac{\rho_\infty K^* L_\infty}{U_\infty} = \text{Damköhler number}$$

$$Pe \equiv Re Sc = \text{Peclet Number}$$

$$Le \equiv \frac{Sc}{Pr} = \text{Lewis Number}$$

2.3 Conservation Laws

The flow is described by the Navier-Stokes equations, two species transport equations, and the ideal gas law. These equations can be written in nondimensional form for a Cartesian coordinate system as:

$$\frac{\partial \rho}{\partial t} + \frac{\partial \rho u_j}{\partial x_j} = 0 \quad (2.1)$$

$$\frac{\partial \rho u_i}{\partial t} + \frac{\partial \rho u_i u_j}{\partial x_j} = -\frac{\partial p}{\partial x_i} + \frac{1}{Re} \frac{\partial \tau_{ij}}{\partial x_j} \quad (2.2)$$

$$\frac{\partial \rho E}{\partial t} + \frac{\partial (\rho E + p) u_j}{\partial x_j} = \frac{1}{Re} \frac{\partial u_i \tau_{ji}}{\partial x_j} + \frac{1}{M^2 Re Pr} \frac{\partial}{\partial x_j} \left(\frac{\mu}{\gamma - 1} \frac{\partial T}{\partial x_j} \right) + \frac{q}{\gamma M^2} \dot{w}_f \quad (2.3)$$

$$\frac{\partial \rho Y_f}{\partial t} + \frac{\partial \rho Y_f u_j}{\partial x_j} = \frac{1}{Re Sc} \frac{\partial}{\partial x_j} \left(\rho D_f \frac{\partial Y_f}{\partial x_j} \right) - \dot{w}_f \quad (2.4)$$

$$\frac{\partial \rho Y_o}{\partial t} + \frac{\partial \rho Y_o u_j}{\partial x_j} = \frac{1}{Re Sc} \frac{\partial}{\partial x_j} \left(\rho D_o \frac{\partial Y_o}{\partial x_j} \right) - r \dot{w}_f \quad (2.5)$$

$$p = \frac{\rho T}{\gamma M^2} \quad (2.6)$$

where:

$$\tau_{ij} = \mu \left(\frac{\partial u_i}{\partial x_j} + \frac{\partial u_j}{\partial x_i} - \frac{2}{3} \delta_{ij} \frac{\partial u_k}{\partial x_k} \right) \text{ is the viscous stress tensor} \quad (2.7)$$

$$\mu = C_1 \frac{T^{3/2}}{T + C_2}, \quad C_1 = 1.3702213, \quad C_2 = 0.3702213 \quad (2.8)$$

$$\dot{w}_f = D a \rho Y_f \rho Y_o e^{-(T_o/T)} \text{ is the reaction rate} \quad (2.9)$$

$$q = h_f + r h_o - (r + 1) h_p \text{ is the heat of combustion} \quad (2.10)$$

$$D_f = \frac{\mu}{\rho} \frac{Sc}{Sc_f}, \quad Sc_f \text{ is the fuel Schmidt number} \quad (2.11)$$

$$D_o = \frac{\mu}{\rho} \frac{Sc}{Sc_o}, \quad Sc_o \text{ is the oxidant Schmidt number} \quad (2.12)$$

$$Y_f + Y_o + Y_p = \text{constant} \quad (2.13)$$

Equations (2.1)-(2.3) describe the conservation of mass, momentum and energy in a fluid continuum. Equations (2.4) and (2.5) describe the advection, diffusion and

reaction of fuel and oxidizer respectively. Equation (2.6) is the perfect gas law. Here it has been assumed that the fuel, oxidizer and product are of equal molecular weight, so that a single, apparent gas constant governs the mixture. For turbulent reacting flows with large heat release (and therefore large density variations) and containing chemical species of non-equal molecular weight, the apparent gas constant must be computed as a function of space and time by summing the gas constants of the individual species times their mass fractions. Equation (2.8) is Sutherland's empirical formula for the temperature dependence of the dynamic viscosity. The constants C_1 and C_2 correspond to air; hence, it is assumed that air is the primary dilutant. Once combined with a set of boundary and initial conditions, these equations define the mathematical problem to be solved.

2.4 Scalar Based Chemistry

A mixture-fraction is defined as

$$\xi \equiv \frac{Y_f - \frac{Y_o}{r} + \frac{Y_{o2}}{r}}{Y_{f1} + \frac{Y_{o2}}{r}} . \quad (2.14)$$

The diffusivity of each of the reacting species is assumed to be equal, so that ξ is a conserved scalar and (2.5) is replaced in the mathematical problem by

$$\frac{\partial \rho \xi}{\partial t} + \frac{\partial \rho \xi u_j}{\partial x_j} = \frac{1}{ReSc} \frac{\partial}{\partial x_j} \left(\mu \frac{\partial \xi}{\partial x_j} \right) . \quad (2.15)$$

Note that with the nondimensionalization, $\mu = \rho D$. The mass fractions of oxidizer and product are related to Y_f and ξ via

$$Y_o = Y_{o2} (1 - \xi) + r (Y_f - \xi Y_{f1}) \quad (2.16)$$

$$Y_p = (r + 1)(\xi Y_{f1} - Y_f) . \quad (2.17)$$

In defining the mathematical problem, it is convenient to replace the equation for the oxidizer (2.5) with that for the mixture fraction (2.15). This switch is motivated

by the simpler form and also by theoretical work, such as Equilibrium Theory [4], the Laminar Flamelet Model [73] and the Conditional Moment Closure [5], which attempt to model average mass fractions and/or reaction rates in terms of Zeldovich parameters such as ξ . Using this approach, the resulting data more readily allow for comparison with these models. In addition, certain theoretical considerations make use of the stoichiometric surface, which is defined as

$$\xi(\vec{x}, t) = \xi_{st} \equiv \frac{Y_{o_2}}{rY_{f_1} + Y_{o_2}}. \quad (2.18)$$

2.5 Low Mach Number Approximation

Many important reacting flows, ranging from the fate of ozone in the atmosphere to the burning of fossil fuels for energy, occur at low speeds. The Mach number of these flows is small yet the density may vary due to heat release. Explicit numerical methods for computing compressible flows must be able to track the maximum speed at which information may propagate, which is equal to the maximum flow velocity plus the speed of sound. The inviscid CFL condition

$$\Delta t \leq \left(\frac{|u|}{\Delta x} + \frac{|v|}{\Delta y} + \frac{|w|}{\Delta z} + \frac{1}{M} \sqrt{\frac{1}{(\Delta x)^2} + \frac{1}{(\Delta y)^2} + \frac{1}{(\Delta z)^2}} \right)^{-1} \quad (2.19)$$

specifies an upper limit to the maximum stable time step that may be used in any explicit method for solving the compressible Navier Stokes (N-S) equations [1]. From this condition we observe that Δt approaches zero as the Mach number goes to zero. Implicit methods permit a larger Δt , but the maximum value is normally less than 5-10 times that given by (2.19) because, with larger Δt , truncation errors become unacceptable and the time accuracy is lost. This is due to the fact that Δt may not be small enough to track the relatively fast moving acoustic waves. Thus even if an implicit scheme is used, it is not practical to compute very low Mach number flows using the fully compressible N-S equations. This timestep restriction may be circumvented by applying a low Mach number approximation to the governing equations,

which effectively decouples the acoustic modes from the vorticity and entropy modes, thus permitting much larger time steps [59]. This makes it much more practical to solve problems where compressibility is primarily due to the exothermicity of chemical reactions, which is the case considered here. The low Mach number approximation is useful in reacting flows if the chemistry is not too fast. Otherwise it may be the fastest reaction, and not the fluid velocity, that sets the maximum stable timestep. Furthermore, if the reaction is too strong, a high Mach number, e.g., detonation, flow may develop.

The low Mach number equations are derived as follows: Let $\varepsilon \equiv \gamma M^2 \ll 1$ and expand the dependent variables as power series in ε :

$$\rho = \rho^{(0)} + \varepsilon \rho^{(1)} + \dots \quad (2.20)$$

$$u_i = u_i^{(0)} + \varepsilon u_i^{(1)} + \dots \quad (2.21)$$

$$T = T^{(0)} + \varepsilon T^{(1)} + \dots \quad (2.22)$$

$$p = \frac{\rho T}{\gamma M^2} = \frac{1}{\varepsilon} \rho^{(0)} T^{(0)} + \rho^{(1)} T^{(0)} + \rho^{(0)} T^{(1)} + \dots = \frac{1}{\varepsilon} p^{(0)} + p^{(1)} + \dots \quad (2.23)$$

$$\rho E = \frac{p}{\gamma - 1} + \rho \frac{u_j^2}{2} = \frac{1}{\varepsilon} \frac{p^{(0)}}{\gamma - 1} + \frac{p^{(1)}}{\gamma - 1} + \rho^{(0)} \frac{u_j^{(0)2}}{2} + \dots \quad (2.24)$$

$$\xi = \xi^{(0)} + \varepsilon \xi^{(1)} + \dots \quad (2.25)$$

$$Y_f = Y_f^{(0)} + \varepsilon Y_f^{(1)} + \dots \quad (2.26)$$

Substituting equations (2.20) - (2.26) into equations (2.1) - (2.4), (2.6) and (2.15), and collecting the lowest order terms in ε , yields the following first-order equations:

$$\frac{\partial \rho^{(0)}}{\partial t} + \frac{\partial \rho^{(0)} u_j^{(0)}}{\partial x_j} = 0 \quad (2.27)$$

$$\frac{\partial p^{(0)}}{\partial x_i} = 0 \quad (2.28)$$

$$\rho^{(0)} \frac{\partial u_j^{(0)}}{\partial x_j} = \frac{1}{T^{(0)}} \left[\frac{1}{RePr} \frac{\partial}{\partial x_j} \left(\mu \frac{\partial T^{(0)}}{\partial x_j} \right) + \frac{\gamma - 1}{\gamma} q \dot{w}_f \right] \quad (2.29)$$

$$\frac{\partial \rho^{(0)} \xi^{(0)}}{\partial t} + \frac{\partial \rho^{(0)} \xi^{(0)} u_j^{(0)}}{\partial x_j} = \frac{1}{ReSc} \frac{\partial}{\partial x_j} \left(\mu \frac{\partial \xi^{(0)}}{\partial x_j} \right) \quad (2.30)$$

$$\frac{\partial \rho^{(0)} Y_f^{(0)}}{\partial t} + \frac{\partial \rho^{(0)} Y_f^{(0)} u_j^{(0)}}{\partial x_j} = \frac{1}{ReSc} \frac{\partial}{\partial x_j} \left(\mu \frac{\partial Y_f^{(0)}}{\partial x_j} \right) - \dot{w}_f \quad (2.31)$$

$$p^{(0)} = \rho^{(0)} T^{(0)} \quad (2.32)$$

Equation (2.28) states that $p^{(0)}$, which is interpreted as the thermodynamic pressure, is uniform in space. Thus, for combustion in an open domain, $p^{(0)}$ is fixed to its value at ∞ , which is here assumed to be constant in time. Thus (2.29), the lowest order energy equation, contains no time derivative. Note that heating due to viscous dissipation drops out as a result of the approximation, and that (2.27), (2.30) and (2.31) remain unchanged.

Since all the dependent variables except $p^{(0)}$ have dropped out of the first order momentum equation, the second order momentum equation must be included in order to close the system.

$$\frac{\partial \rho^{(0)} u_i^{(0)}}{\partial t} + \frac{\partial \rho^{(0)} u_i^{(0)} u_j^{(0)}}{\partial x_j} = -\frac{\partial p^{(1)}}{\partial x_i} + \frac{1}{Re} \frac{\partial \tau_{ij}^{(0)}}{\partial x_j} \quad (2.33)$$

Here, $p^{(1)}$ is interpreted as the dynamic pressure. Since $p^{(0)}$ is a known constant, determined by its free-stream value, (2.27), (2.29), (2.30), (2.31), (2.32) and (2.33) comprise eight equations for the eight unknowns: $\rho^{(0)}$, $u^{(0)}$, $v^{(0)}$, $w^{(0)}$, $T^{(0)}$, $p^{(1)}$, $\xi^{(0)}$ and $Y_f^{(0)}$; thus the equation set is closed.

Part I

Numerical Simulations

Chapter 3

NUMERICAL ALGORITHM

3.1 Third Order Adams-Bashforth Scheme

The superscripts will now be dropped except to distinguish between the thermodynamic, $p^{(0)}$, and dynamic, $p^{(1)}$, pressures. Integrating equation (2.33) from time t to time $t + \Delta t$ gives

$$(\rho u_i)^{n+1} - (\rho u_i)^n = \int_t^{t+\Delta t} B_i dt - \Delta t \frac{\partial}{\partial x_i} \mathcal{P} \quad (3.1)$$

where:

$$n = \frac{t}{\Delta t} \quad (\text{an integer})$$
$$B_i = \frac{\partial}{\partial x_j} \left(\frac{\tau_{ij}}{Re} - \rho u_i u_j \right)$$

\mathcal{P} = dynamic pressure averaged over time interval $(t, t + \Delta t)$.

The integral on the right hand side of (3.1) is computed using a third-order, one-sided approximation

$$\int_t^{t+\Delta t} B_i dt = \frac{\Delta t}{12} (23B_i^n - 16B_i^{n-1} + 5B_i^{n-2}) \quad (3.2)$$

which, when used in (3.1), gives the Adams-Bashforth (A-B) scheme. The A-B method is numerically efficient, but requires fluxes at two previous time steps and thus has large storage requirements [24]. This scheme is well suited to the CM-5, which has 16 Gbytes of RAM. Taking the divergence of (3.1) and using (2.27) gives

$$\nabla^2 \mathcal{P} = \frac{1}{\Delta t} \left[\left(\frac{\partial \rho}{\partial t} \right)^{n+1} + \nabla \cdot (\rho \vec{u})^* \right] \quad (3.3)$$

where:

$$(\rho u_i)^* = (\rho u_i)^n + \frac{\Delta t}{12} (23B_i^n - 16B_i^{n-1} + 5B_i^{n-2}) . \quad (3.4)$$

The density time derivative in (3.3) is a potential source of instability and requires careful treatment. In practice, the second-order explicit approximation

$$\left(\frac{\partial \rho}{\partial t}\right)^{n+1} = \frac{3\rho^{n+1} - 4\rho^n + \rho^{n-1}}{2\Delta t} \quad (3.5)$$

has been found to be much more stable than either a third-order explicit approximation or the third-order compact approximation

$$\left(\frac{\partial \rho}{\partial t}\right)^{n+1} = 3F_\rho^n - 3F_\rho^{n-1} + F_\rho^{n-2} , \quad (3.6)$$

where F_ρ is defined in equation (3.8) below. This is likely due to the fact that even-ordered schemes are dissipative, whereas odd-ordered schemes are dispersive [1]. Even with an even-ordered approximation to the density time derivative, however, it was found that the third-order Adams-Bashforth scheme is only stable for maximum density variations up to about a factor of 3. Sandoval found that by decreasing the Reynolds number and performing an iteration, larger variations in ρ could be achieved [86]. Najm demonstrated that a predictor-corrector time-stepping algorithm is stable for very large density changes [69].

The momentum equation now becomes

$$(\rho u_i)^{n+1} = (\rho u_i)^* - \Delta t \frac{\partial \mathcal{P}}{\partial x_i} \quad (3.7)$$

where \mathcal{P} is the solution to (3.3) using (3.5). Finally, heat release and diffusion effects must be included by ensuring that equation (2.29) is satisfied at each instant in the calculation. There are several ways of doing this; here we will follow the technique of McMurtry *et al.* [59] by rewriting equation (2.27) as

$$\frac{\partial \rho}{\partial t} + u_j \frac{\partial \rho}{\partial x_j} + \rho \frac{\partial u_j}{\partial x_j} = 0$$

and replacing the third term on the left hand side with equation (2.29). This gives an equation for the local density,

$$\frac{\partial \rho}{\partial t} = F_\rho = -u_j \frac{\partial \rho}{\partial x_j} - \frac{1}{T} \left[\frac{1}{RePr} \frac{\partial}{\partial x_j} \left(\mu \frac{\partial T}{\partial x_j} \right) + \frac{\gamma - 1}{\gamma} q \dot{w}_f \right]. \quad (3.8)$$

3.2 Pressure Projection Method

The equations are advanced in time according to the projection method [14]. First, equation (3.8) is integrated via the third-order A-B method to obtain ρ^{n+1} , and equation (3.5) is used to compute $(\partial \rho / \partial t)^{n+1}$. Second, $(\rho u_i)^*$ is obtained from equation (3.4), $\nabla \cdot (\rho \vec{u})^*$ is taken, and the right hand side of (3.3) is computed. Third, with periodicity in the y and z directions, equation (3.3) is Fourier transformed in y and z yielding

$$\frac{\partial^2 \hat{\mathcal{P}}}{\partial x^2} - \lambda^2 \hat{\mathcal{P}} - \kappa^2 \hat{\mathcal{P}} = \widehat{rhs}(x, \lambda, \kappa)$$

where a hat, $\hat{\phi}$, denotes the Fourier transform of the function ϕ , and λ and κ are wavenumbers in the y and z directions, respectively. The flow is assumed to exit into a large ambient domain, hence a Dirichlet condition is used for the pressure at the outflow boundary. For the present simulations the exit pressure was set to zero, however, another constant could be used without affecting the results. Since the exit pressure is fixed, the pressure at the inlet must be allowed to vary in order to remain consistent with the exit condition. Therefore, a Neumann condition is supplied at the entrance [37], i.e., the pressure derivative normal to the inlet is set to zero. A fourth-order central finite difference approximation for $\partial^2 \hat{\mathcal{P}} / \partial x^2$, with a second-order approximation at the $i=2$ and $i=nx-1$ boundary nodes, results in the

following pentadiagonal matrix for $\hat{\mathcal{P}}$:

$$\begin{aligned}
-3\hat{\mathcal{P}}_1 + 4\hat{\mathcal{P}}_2 - \hat{\mathcal{P}}_3 &= 0 \\
\hat{\mathcal{P}}_1 - [2 + \Delta x^2(\lambda^2 + \kappa^2)]\hat{\mathcal{P}}_2 + \hat{\mathcal{P}}_3 &= \Delta x^2 \widehat{rhs}(2, \lambda, \kappa) \\
&\vdots \\
-\hat{\mathcal{P}}_{i-2} + 16\hat{\mathcal{P}}_{i-1} - [30 + 12\Delta x^2(\lambda^2 + \kappa^2)]\hat{\mathcal{P}}_i + 16\hat{\mathcal{P}}_{i+1} - \hat{\mathcal{P}}_{i+2} &= 12\Delta x^2 \widehat{rhs}(i, \lambda, \kappa) \\
&\vdots \\
\hat{\mathcal{P}}_{nx-2} - [2 + \Delta x^2(\lambda^2 + \kappa^2)]\hat{\mathcal{P}}_{nx-1} + \hat{\mathcal{P}}_{nx} &= \Delta x^2 \widehat{rhs}(nx - 1, \lambda, \kappa) \\
\hat{\mathcal{P}}_{nx} &= 0
\end{aligned}$$

After solving this system of equations for $\hat{\mathcal{P}}$, \mathcal{P} is then obtained by a two-dimensional inverse FFT. Next, \mathcal{P} is used in equation (3.7) to get $(\rho u_i)^{n+1}$. Finally, equations (2.30) and (2.31) are timestepped via the third-order A-B method to get $(\rho \xi)^{n+1}$ and $(\rho Y_f)^{n+1}$, and all primitive variables at time $n + 1$ are obtained by dividing by ρ^{n+1} . Note that $p^{(0)}$ is set from the initially constant density and temperature fields according to (2.32).

3.3 Sixth Order Compact Scheme

A sixth-order accurate Compact scheme is used for computing spatial derivatives. The Compact scheme is superior to finite-difference methods in treating the small scales. The resolution characteristics of a scheme can be quantified by means of a Fourier analysis of the differencing algorithm. Lele [50] has demonstrated that Compact schemes are similar to spectral schemes in accurately computing the behavior of the higher wavenumbers of a problem. This makes them good alternatives to spectral schemes if the problem has nonperiodic boundaries. The sixth-order Compact scheme also has the ability to accurately represent phase speeds at high wavenumbers. The inability of conventional finite-difference schemes to accurately compute phase speeds at high wavenumbers can lead to significant dispersion errors in the solution.

Typically the global error is dominated by the boundary error; thus it is desirable to have a high formal accuracy at the boundaries. In the present simulations, a fifth-order Compact boundary scheme has been derived for use at the inlet and exit. The fifth-order scheme is one-sided at the first boundary node and “lop-sided” at the second boundary node. Combining the sixth-order scheme for the interior points with the fifth-order boundary scheme results in the following tridiagonal matrix for the x derivative, ϕ' , of a variable, ϕ :

$$\begin{aligned}
\phi'_1 + 4\phi'_2 &= -\frac{37}{12h}\phi_1 + \frac{2}{3h}\phi_2 + \frac{3}{h}\phi_3 - \frac{2}{3h}\phi_4 + \frac{1}{12h}\phi_5 \\
\alpha\phi'_1 + \phi'_2 + \alpha\phi'_3 &= a\phi_1 + b\phi_2 + c\phi_3 + d\phi_4 + g\phi_5 \\
&\vdots \\
12\phi'_{i-1} + 36\phi'_i + 12\phi'_{i+1} &= (\phi_{i+2} + 28\phi_{i+1} - 28\phi_{i-1} - \phi_{i-2})/h \\
&\vdots \\
\alpha\phi'_{nx-2} + \phi'_{nx-1} + \alpha\phi'_{nx} &= -a\phi_{nx} - b\phi_{nx-1} - c\phi_{nx-2} - d\phi_{nx-3} - g\phi_{nx-4} \\
4\phi'_{nx-1} + \phi'_{nx} &= \frac{37}{12h}\phi_{nx} - \frac{2}{3h}\phi_{nx-1} - \frac{3}{h}\phi_{nx-2} + \frac{2}{3h}\phi_{nx-3} - \frac{1}{12h}\phi_{nx-4}
\end{aligned}$$

Here:

$$\begin{aligned}
h &= \Delta x = \Delta y = \Delta z = \text{grid spacing} \\
\alpha &= 0.2142857143 \\
a &= -0.6785714286/h \\
b &= -0.119047619/h \\
c &= 0.8571428571/h \\
d &= -0.07142857143/h \\
g &= 0.0119047619/h
\end{aligned}$$

A periodic tridiagonal solver is used to compute derivatives in the y and z directions.

3.4 Boundary Conditions

The elliptic nature of the equations presents a dilemma since boundary variables depend on uncomputed regions upstream and downstream of the computational domain; thus some error is unavoidable at the inlet and exit.

3.4.1 Inlet

All variables, except pressure, are specified at the inlet. The inlet turbulence is created by scanning through an existing 128^3 velocity field generated by Mell [61]. The rate of scan is set equal to the mean streamwise velocity at the inlet U_∞ , and cubic-spline interpolation is used to obtain velocity values which lie between data planes. It was found that linear interpolation is unacceptable since it gives functions with discontinuous derivatives. The pressure-work term in the equation for the conservation of mechanical energy is very sensitive to velocity derivatives at the inlet, and linear interpolation causes this term to oscillate.

Figure 3.1 shows the three-dimensional energy and dissipation-rate spectra of the inlet turbulence, $E(k)$ and $\epsilon(k)$, respectively, where k is the magnitude of the three-dimensional wavevector. The spectra were computed by averaging the Fourier amplitudes of the velocities over spherical shells in wavenumber space. The integral, Taylor and Kolmogorov scales at the inlet are given below:

$$l \equiv \frac{l^*}{L_\infty} = \left(\frac{3}{8}\right) \frac{\int_0^\infty \frac{E(k)}{k} dk}{\int_0^\infty E(k) dk} = 0.141$$

$$\lambda \equiv \frac{\lambda^*}{L_\infty} = \frac{1}{2\pi} \left(\frac{15u_{rms}^2}{\int_0^\infty k^2 E(k) dk} \right)^{1/2} = 0.0646$$

$$\eta \equiv \frac{\eta^*}{L_\infty} = \frac{1}{2\pi} \left(\frac{1}{15}\right)^{1/4} \left(\frac{\nu \lambda}{Re u_{rms}} \right)^{1/2} = 0.00400$$

Here u_{rms} is the root-mean-square velocity of the incoming turbulence nondimensionalized by U_∞ (i.e., the turbulence level).

3.4.2 Exit

A one-dimensional advection condition is used at the outlet such that all variables, except pressure, satisfy an equation of the form

$$\frac{\partial \phi}{\partial t} + C_e \frac{\partial \phi}{\partial x} = 0, \quad (3.9)$$

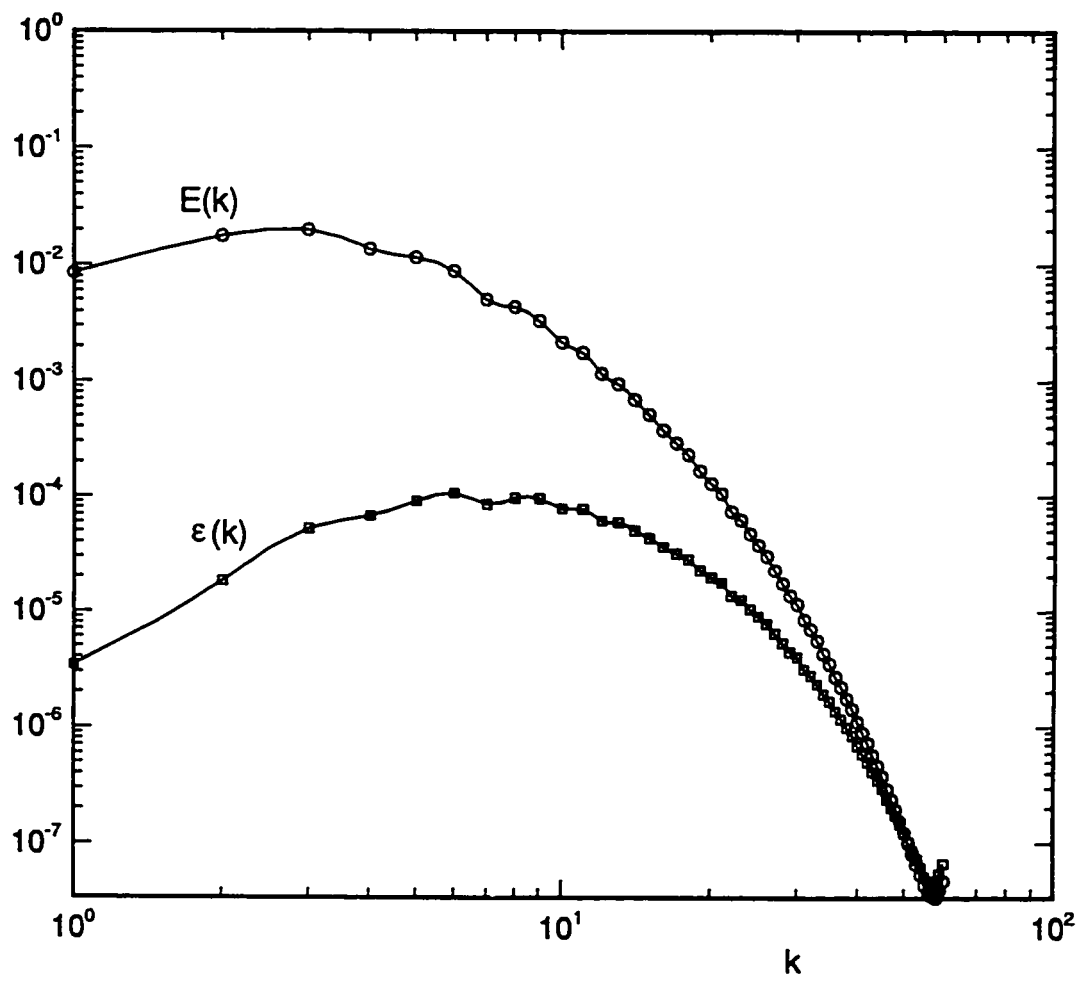


Figure 3.1: 3-D energy and dissipation spectra of inlet turbulence.

where C_e is a phase speed which should characterize the celerity of the large eddies [25], and must be positive for stability [10]. Often C_e is set to an average exit velocity [56], which is the case here, hence $C_e = \langle U \rangle_{\text{exit}}$.

3.5 Conservation Checks

Since the continuity equation (2.1) has been replaced by (3.8), a valid question arises as to whether the numerical algorithm conserves mass. In performing the simulations, conservation of mass and momentum are periodically checked by integrating the continuity and mechanical energy equations over the flow domain. The scheme was found to conserve both mass and momentum globally. The various terms monitored in the mechanical energy equation are given below:

$$\begin{aligned} \frac{\partial}{\partial t} \int_V \rho \frac{u_j u_j}{2} dV & \text{ rate of increase of energy} \\ \int_A \rho u \frac{u_j u_j}{2} \Big|_{x_1}^{x_2} dA & \text{ net energy flux through inlet and outlet} \\ \int_V u_j \frac{\partial \mathcal{P}}{\partial x_j} dV & \text{ pressure work} \\ -\frac{1}{Re} \int_V u_i \frac{\partial \tau_{ij}}{\partial x_j} dV & \text{ viscous work} \end{aligned}$$

The terms should sum to zero if momentum is conserved. If the Reynolds number is increased beyond that which allows adequate resolution, the sum of these terms will deviate from zero. This effect shows up well before the solution becomes unstable, and provides a resolution check on the simulation. Additionally, the left and right hand sides of the internal energy equation (2.29) and the Poisson equation (3.3) are periodically compared and plotted. These relations were found to be satisfied on a pointwise basis at each instant in the calculation, ensuring conservation of energy and an accurate dynamic pressure field. The agreement between the left and right hand sides of (2.29) and (3.3) was quantified by calculating a normalized difference defined

as

$$\Theta \equiv \frac{\langle (LHS - RHS)^2 \rangle}{\sqrt{\langle (LHS)^2 \rangle \langle (RHS)^2 \rangle}}$$

where the angle brackets denote an average over the entire field. The error quantity Θ must be close to zero for a well-resolved calculation.

3.6 Stability

The stability of the Compact scheme depends on the manner in which second derivatives are computed. Note that, in the viscous/diffusive terms in the governing equations, μ , ρ and D are not constants and appear inside one of the derivatives. This means that it is much simpler to compute a first derivative, multiply it by the appropriate variable(s), then take another derivative, than it is to expand the derivatives using the chain rule and then take second derivatives directly. Furthermore, expanding the viscous/diffusive terms causes the loss of their conservative form. However, Lele [50] advocates using the nonconservative approach in order to provide finite damping of grid to grid oscillations (2δ waves). The 2δ waves remain undamped if the conservative form is used with two consecutive applications of the first derivative operator. This means that tiny oscillations, possibly arising from numerical roundoff error, may gradually grow in time and eventually affect the stability of the scheme.

In the present approach the viscous/diffusive terms are solved in conservative form. Damping of the 2δ waves is accomplished by applying a fourth-order Compact filter to the primitive variables at every fifth timestep. The energy removed by the filter is compared to the other terms in the integrated mechanical energy equation and found to be negligible. Compact filters are much better low pass filters than explicit filters since they confine their effects to the highest wavenumbers. This provides the necessary damping of the 2δ waves without contaminating the computation. However, filtering in this manner will not stabilize an underresolved calculation [79].

3.7 Parallel Computing

3.7.1 Optimization

The primary task of converting a code to run on a distributed memory machine is to optimize array layouts in memory so that the computational load is well balanced among the processors. Another task is to minimize interprocessor communication which necessarily results from finite-difference operations. On the CM-5, each element of an array may reside on a different virtual processor or the entire array may reside on the front-end computer. The manner in which array elements are distributed among the processors can have tremendous impact on the performance of a DNS code. In order to achieve good performance, it is crucial that order dependent operations (do loops) be avoided wherever possible, and that they not be performed on array indices that have been distributed over multiple nodes. Such operations force all but one processor to sit idle until the operation is complete. By optimizing array layouts in memory, the execution time of the present code was decreased by over a factor of 30.

The Poisson solver described previously, as well as the Compact scheme for computing spatial derivatives, both require matrix inversions. The Gaussian reduction procedure for matrix inversion is necessarily an order dependent process. One method for parallelizing matrix operations is to split the matrix into submatrices and follow a fork-and-join model [23] where each processor is given some number of operations to perform. For the present simulations, a much simpler approach, i.e., domain decomposition, was taken. For example, in order to compute the x derivative of an array, the array is first copied into a dummy array with the x dimension laid out serially so that all elements corresponding to the x dimension reside on a single processor. The Gaussian reduction operation is then done serially on that index. Since the computational domain is three dimensional, the matrix inversion along the x direction is done

a plane at a time, i.e., the domain is partitioned into y-z planes which are operated on in parallel. This practice is most efficient if the total number of grid points in a y-z plane equals or exceeds the number of physical processors available. In such cases, no penalty is paid by executing the x index serially. The same procedure is used for computing y and z derivatives. Layout changes of this sort require extensive node communication, but this is a relatively efficient process on the CM-5, i.e., it is far faster than performing a do loop operation on an array index which has been distributed over multiple nodes. Fast Fourier Transforms (FFTs) may operate on the same principle, transforming in one direction a plane at a time. If a purely serial operation must be performed, i.e., one that cannot be parallelized in any direction, then the quickest procedure is to call a library routine which copies the array onto the front-end computer, operate on the array, then call another library routine to copy the results back to the CM. However, on the CM-5, caution must be taken to ensure that there are no array home mismatches. An array home mismatch occurs whenever an array is passed to a subroutine in which it has a different layout than in the calling routine. If this happens, the code will run, but the computed results will be in error.

3.7.2 Performance

One measure of the parallel efficiency of a code is how evenly the computational load is distributed among the processors. For the present simulations the load balance was measured as follows:

$$\text{Load Balance} = \frac{(\text{total node} + \text{communication time})}{(\text{number of processors})(\text{total elapsed time})} = 0.91$$

If all of the processors are busy all of the time, then the above ratio will be unity. If many processors sit idle while only a few are computing, then this ratio will be much lower. The ratio for the plume code of 0.91 indicates a reasonably efficient use of all processors. The efficient use of processors is aided by choosing grid dimensions which

match the number of processors in a partition. E.g., if the code is run on a 128 node partition, then a grid resolution of 128 points, or some multiple thereof in at least one direction, is optimal.

Another measure of parallel efficiency is scalability, i.e., the reduction in computing time achieved when the number of processors is doubled. If the amount of interprocessor communication of a code is very high, it will not perform well on a large processor partition. For the present code, wall clock times were measured on two different partitions (using a grid resolution of 512 X 128 X 128) to obtain the following measure of scalability:

$$\text{Scalability} = \frac{43.8 \text{ seconds per timestep on 128 node partition}}{24.3 \text{ seconds per timestep on 256 node partition}} = 1.8$$

The scalability factor of 1.8 again indicates a well parallelized code. The memory requirements of the code increase slightly as the number of processors increases. Running on a 128 node partition requires 2.75 Gbytes of RAM, whereas running on a 256 node partition requires 3 Gbytes. This may be due to the way the compiler optimizes the code for different partitions.

Using standard linear equations software, comparisons have been made of actual floating point operations per second achieved, using full optimization, on both the CM-5 and Cray C90 [23]. A Cray C90 with 16 processors with cycle times of 4.2 ns ran the computer code at 10.78 Gflops, whereas a CM-5 with 512 processors ran at 30.4 Gflops. However, the operational speed of the computers depends to a large extent on the nature and size of the computations performed, and these numbers should not be taken as an absolute measure of the machines relative performance. For the present simulations, the CM-5 was chosen for its large amount of memory.

Chapter 4

RESULTS

4.1 *Simulation Parameters*

Four different simulations were performed which will be denoted by the letters A, B, C, and D. Case A was designed to match the reactive plume experiment of Brown and Bilger [8] to the extent possible. In their experiment, the reacting species concentrations were very small so that the effects of heat release could be neglected, hence the flow was essentially incompressible and isothermal. Therefore, the heat release q and activation temperature T_a in the DNS case A were set to zero. Note that Brown and Bilger work with molar fractions whereas here mass fractions are used. Table 4.1 lists parameters for the wind tunnel experiment and for case A from the numerical simulation. In the table, d is the nozzle diameter of the fuel source (for the DNS this is defined as the diameter of a tophat source having equivalent mass flux), and Da_t and Re_t are the turbulent Damköhler and Reynolds numbers, respectively, defined at the inlet. The parameters d/l and Re_t differ due to numerical resolution requirements.

Regarding the difference in ξ_{st} , very low values of ξ_{st} act to increase the numerical resolution requirements of the chemical fields. This can be understood by considering the resolution requirements for Y_p . Y_p is zero where ξ is zero, and it attains its maximum value where $\xi = \xi_{st}$. If ξ_{st} is close to zero, then a small change in ξ corresponds to a very large change in Y_p . The same is true for Y_o , which must be adequately resolved in order to obtain accurate values for \dot{w}_f . The fact that an

Table 4.1: Comparison of flow parameters from the wind tunnel experiment of Brown and Bilger and from the DNS case A

Parameter	Experiment	DNS case A
$u_{rms} \equiv \left(\frac{\langle \tilde{u} \cdot \tilde{u} \rangle}{3} \right)^{1/2}$	0.062	0.26
$\frac{d}{l}$	0.185	0.642
r	1.6	1.6
Y_{O_2}	1.67×10^{-6}	0.2
Y_{f_1}	5.52×10^{-4}	1
$\xi_{st} \equiv \frac{Y_{O_2}}{rY_{f_1} + Y_{O_2}}$	0.00184	0.111
$Da_t \equiv \frac{K^* l^*}{u_{rms}^*}$	3.81	3.81
$Re_t \equiv \frac{u_{rms}^* l^*}{\nu^*}$	665	147
Sc	0.75	0.75

equation for Y_o is not being solved makes no difference since small errors in Y_f and ξ translate into large errors for Y_o , i.e., through equation (2.16). From another point of view, the frozen and equilibrium limits for $Y_f(\xi)$ become very close together. This is the reason for the differences in Y_{f_1} , Y_{O_2} , and hence ξ_{st} , between the experiment and the DNS. The resolution difficulties associated with very small (or very large) values of ξ_{st} are not widely recognized.

The reason for the difference in u_{rms} requires some explanation. In order to get a complete picture of the combustion process, the computation is carried far enough downstream so that the reaction reaches completion, i.e., the fuel is nearly all consumed. This requires vast computer resources and so it is desirable to shrink the required distance as much as possible. This is accomplished by making u_{rms} large (or, equivalently, U_∞ smaller compared to u_{rms}^*); however, numerical stability dictates

that there be no backflow through the inlet, which effectively sets the maximum value of u_{rms} such that, at any given time, the minimum streamwise velocity at the inlet is greater than or equal to zero. This practice results in a higher turbulence level than that found in most wind tunnel experiments. Thus some comparisons with laboratory data are made by interpreting both sets of data using a frame of reference moving with $\langle U \rangle$. This is accomplished by considering the time $t = x/\langle U \rangle$, and defining the initial large eddy turnover time as $\tau = l/u_{rms}$, so that the downstream large-eddy time is defined as $t_{le} = t/\tau = xu_{rms}/\langle U \rangle l$. The number of large eddy turnovers is thus proportional to $u_{rms}/\langle U \rangle$. Note that if this ratio is not much less than one, then the integral scale of the turbulence is of the order of the longitudinal scale of decay and hence homogeneity in the streamwise direction may not be assumed [19].

Cases B, C, and D were performed in order to examine the effects of heat release, activation temperature and the Damköhler number on the reaction physics. Table 4.2 lists the parameters that were varied from case to case. In all cases, the Prandtl

Table 4.2: Parameters that varied from case to case in the numerical simulations

Parameter	A	B	C	D
q	0	73.03	73.03	224.7
Da_t	3.81	3.81	16.3	3.81
T_a	0	0	3	3

number was equal to the Schmidt number, $Pr = Sc = 0.75$, and all other flow parameters remained as stated in Table 4.1.

4.2 Visualization

Figure 4.1, taken from case D, shows instantaneous contours of density, vorticity-magnitude, mixture-fraction and reaction rate on a planar slice down the centerline of the plume; the flow enters at the left and exits to the right. The plots were made at the end of the simulation, after all variables had reached statistical stationarity. Since the fuel is in short supply, the reaction rate is strongest near the inlet where fuel is in greatest abundance. Figure 4.2 shows instantaneous ‘head on’ views of ξ at various downstream locations including the inlet. The plots, taken from case A, demonstrate how the initially circular plume is rapidly distorted by the turbulence and eventually reaches the side boundaries.

4.3 Turbulent Flow Field

Since the domain is periodic in the transverse directions, two-dimensional energy spectra can be calculated by Fourier Transform in y and z . Figure 4.3 shows instantaneous 2-D total energy spectra of the velocity field at various downstream locations for case A, where k_2 is the magnitude of the 2-D wavevector. The spectra were computed by transforming planar (y - z) sections of u , v and w at an instant in time and averaging over annular sections in Fourier space. Two dimensional spectra are seldom measured in experiments but are sometimes computed from DNS [72] when there are only two periodic directions. The spectra provide a check on the numerical resolution, which is seen to be very good. Figure 4.4 shows longitudinal autocorrelations of velocity at various downstream locations for case A. In addition to being temporally stationary, the turbulence is spatially homogeneous in y and z ; hence averages are computed over time and over cross-stream directions. The correlation function f is defined below for the transverse components of velocity, with the averaging procedure

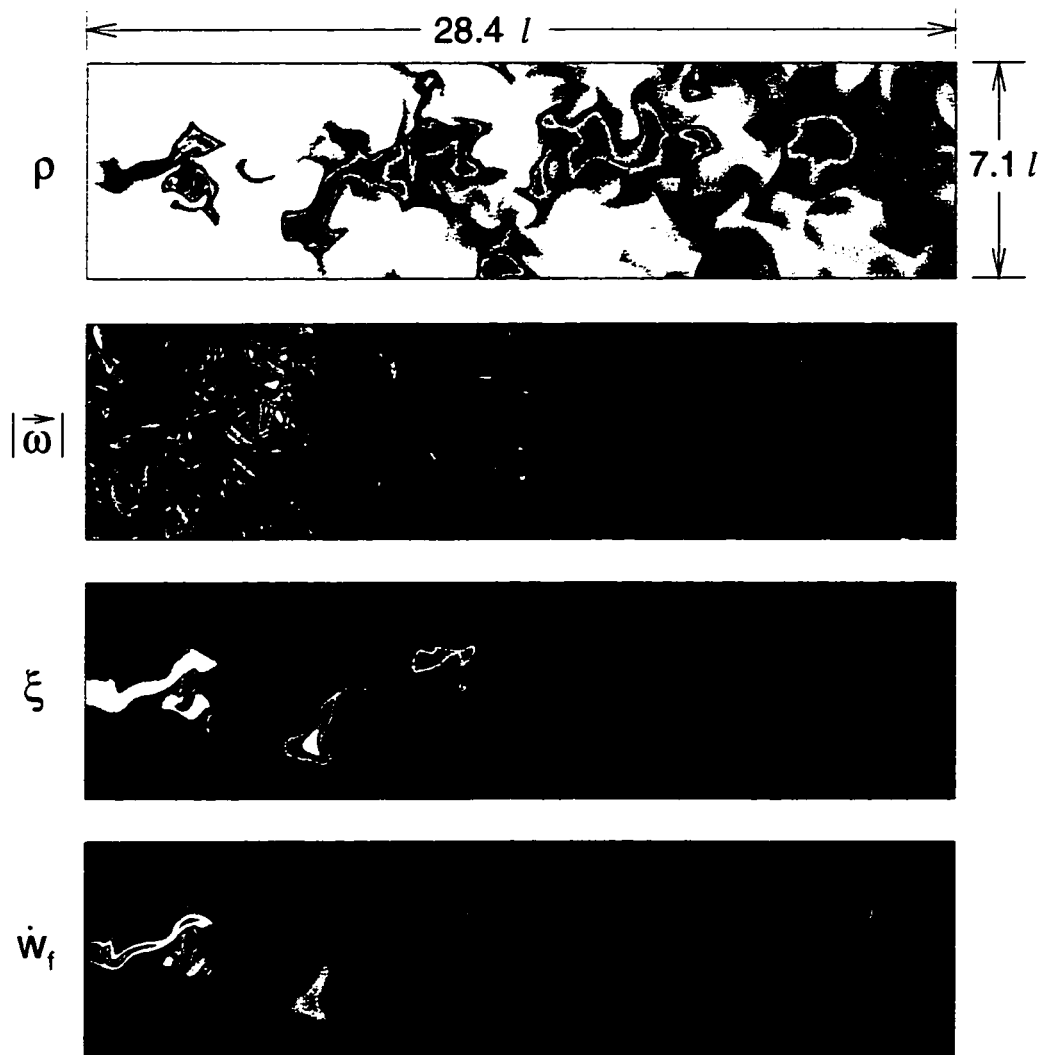


Figure 4.1: Contours of density, vorticity-magnitude, mixture-fraction and reaction rate on a centerline slice from case D.

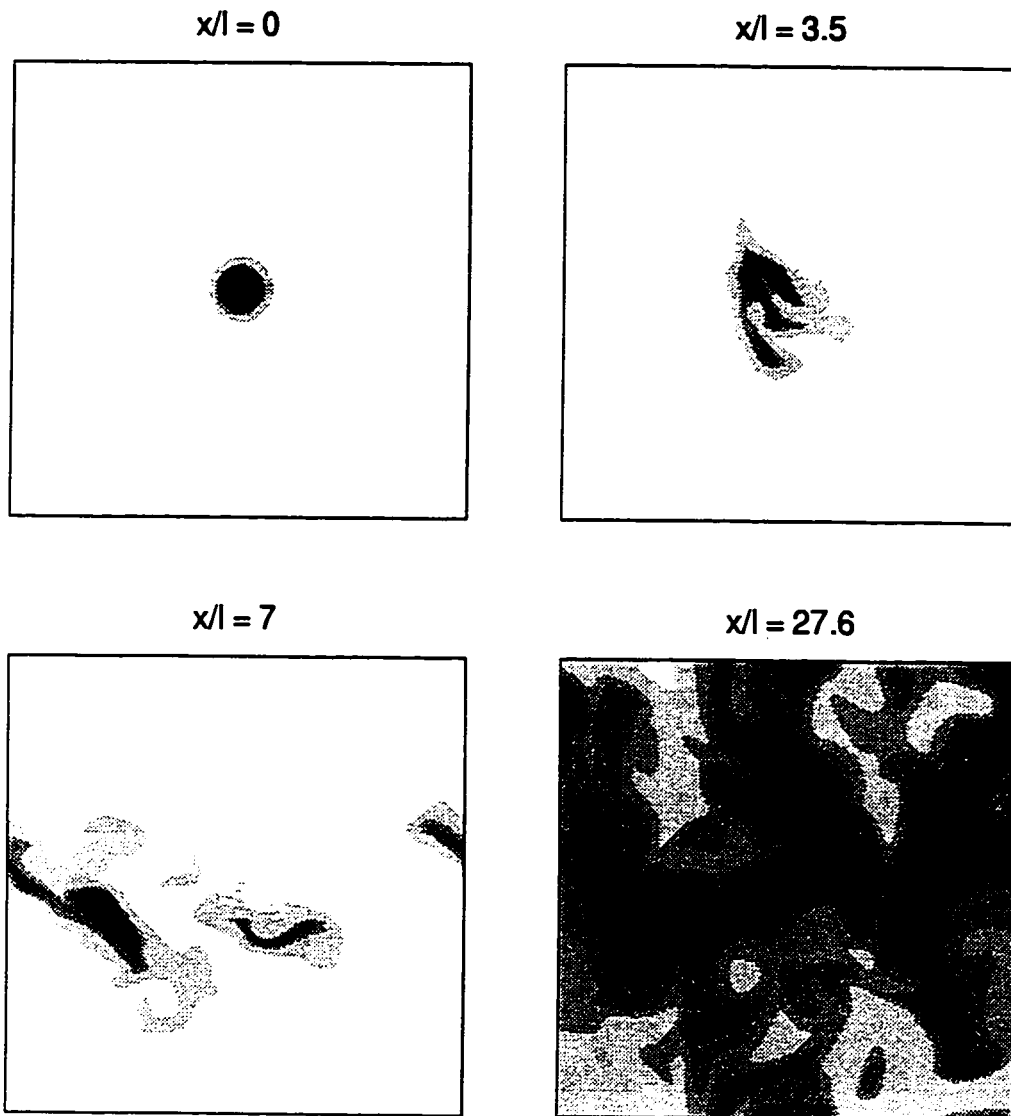


Figure 4.2: Gray-scale contours of mixture-fraction on various cross-stream cuts, taken from case A.

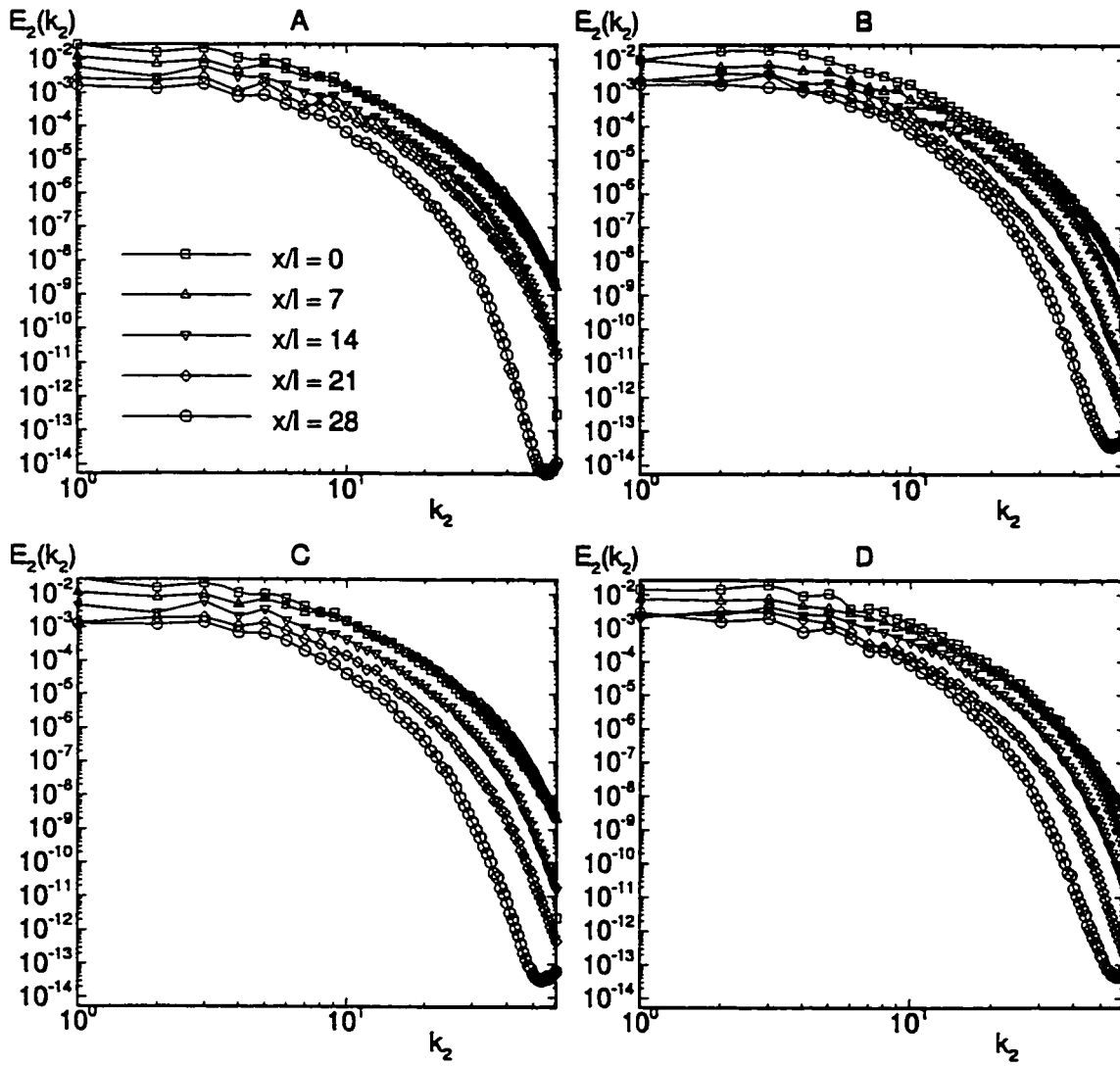


Figure 4.3: Two dimensional total energy spectra at various downstream locations.

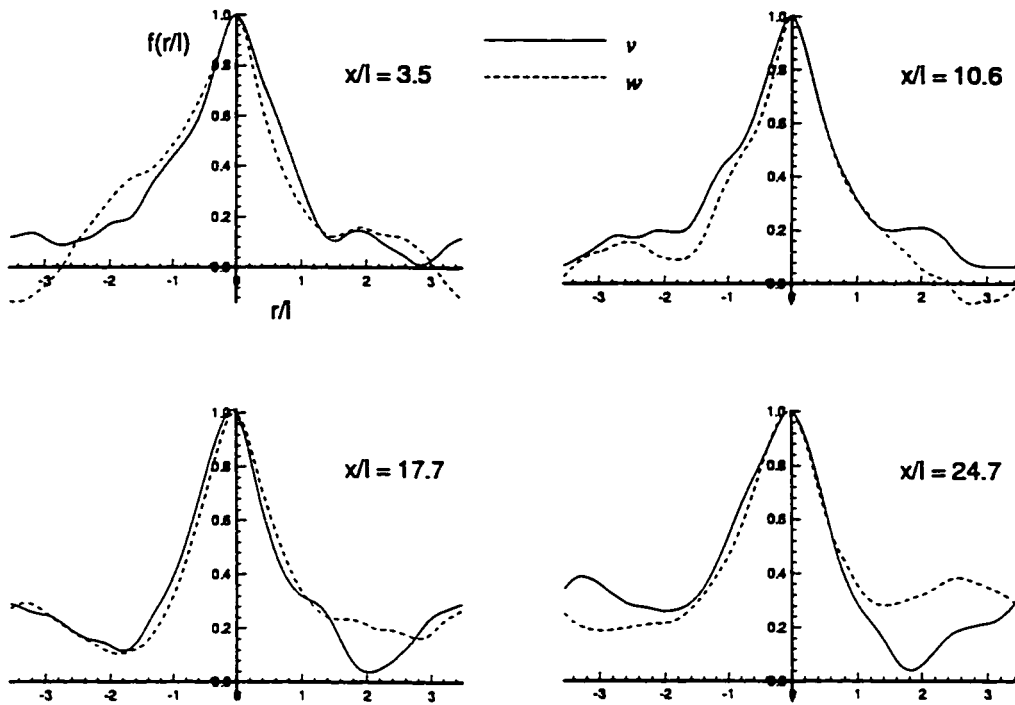


Figure 4.4: Longitudinal velocity autocorrelations from case A.

shown to the right of each equation.

$$f_v(\Delta y) = \frac{\langle v(t, x, y, z)v(t, x, y + \Delta y, z) \rangle}{\langle v(t, x, y, z)^2 \rangle}, \quad \langle () \rangle \equiv \int_0^1 \int_0^1 () dz dt \quad (4.1)$$

$$f_w(\Delta z) = \frac{\langle w(t, x, y, z)w(t, x, y, z + \Delta z) \rangle}{\langle w(t, x, y, z)^2 \rangle}, \quad \langle () \rangle \equiv \int_0^1 \int_0^1 () dy dt \quad (4.2)$$

Far downstream, the tails of the curves rise above zero as the integral scale of the turbulence, l^* , approaches the lateral length of the computational domain, L_∞ . Theoretically, the curves for v and w should be identical and symmetric. The lack of equality and symmetry gives some idea of the statistical errors. The statistical errors are due to the finite time and finite space samples of the data. Since the inlet turbulence is periodic, the time signal repeats itself and hence there is a limited number of statistically independent samples available. If the length of the turbulent field being fed through the inlet were increased, then the statistical errors would decrease.

In figure 4.5 the mean density is plotted as a function of downstream distance for the three cases with heat release. Here the density was averaged in time and over the cross-stream directions y and z . In figure 4.6 is plotted the rms density normalized by the mean density. Case B differs from cases C and D due to the difference in T_a . Higher activation temperatures slow the reaction, thereby decreasing the rate of heat release and density dilatation.

Figure 4.7 shows the downstream growth of the Taylor microscales, where a microscale in the i direction is computed as

$$\lambda_i = \left[\frac{\langle u_i^2 \rangle}{\langle \left(\frac{\partial u_i}{\partial x_i} \right)^2 \rangle} \right]^{1/2} \quad (\text{no sum on } i), \quad \langle () \rangle \equiv \int_0^1 \int_0^1 \int_0^1 () dy dz dt. \quad (4.3)$$

The length scales drop slightly, as the inlet flow adjusts to its environment, then rise steadily up to the exit. The curves show that the turbulence is roughly isotropic. By assuming high Reynolds number and a power law decay for the turbulent kinetic

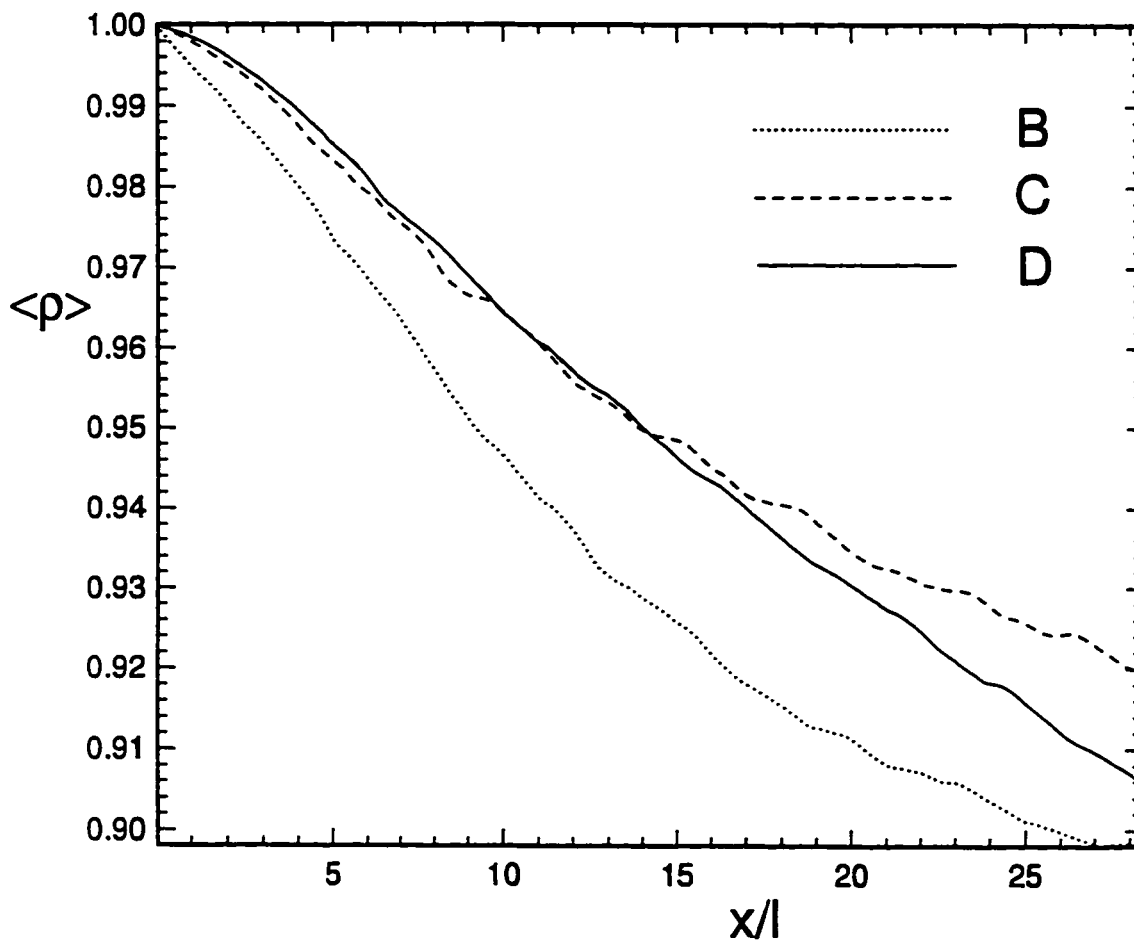


Figure 4.5: Mean density vs downstream distance.

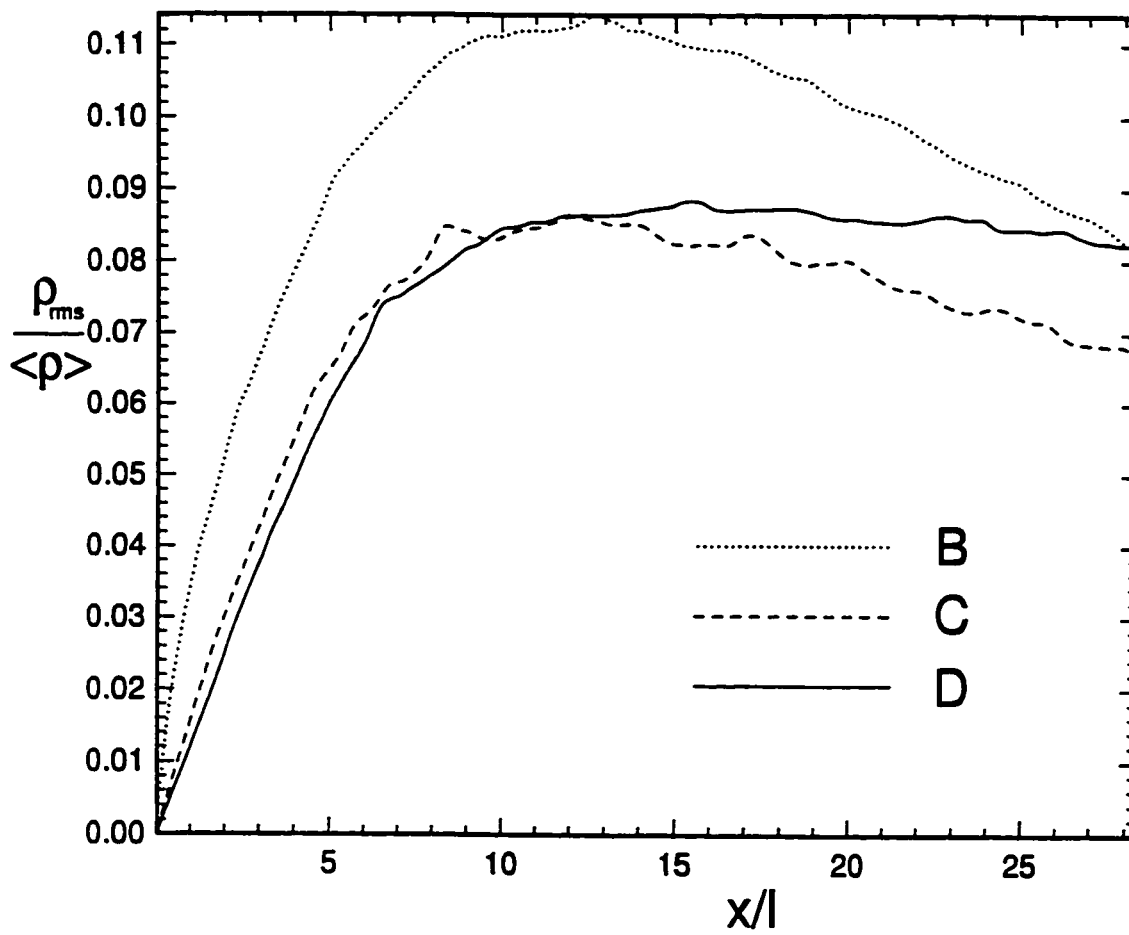


Figure 4.6: Density fluctuations vs downstream distance.

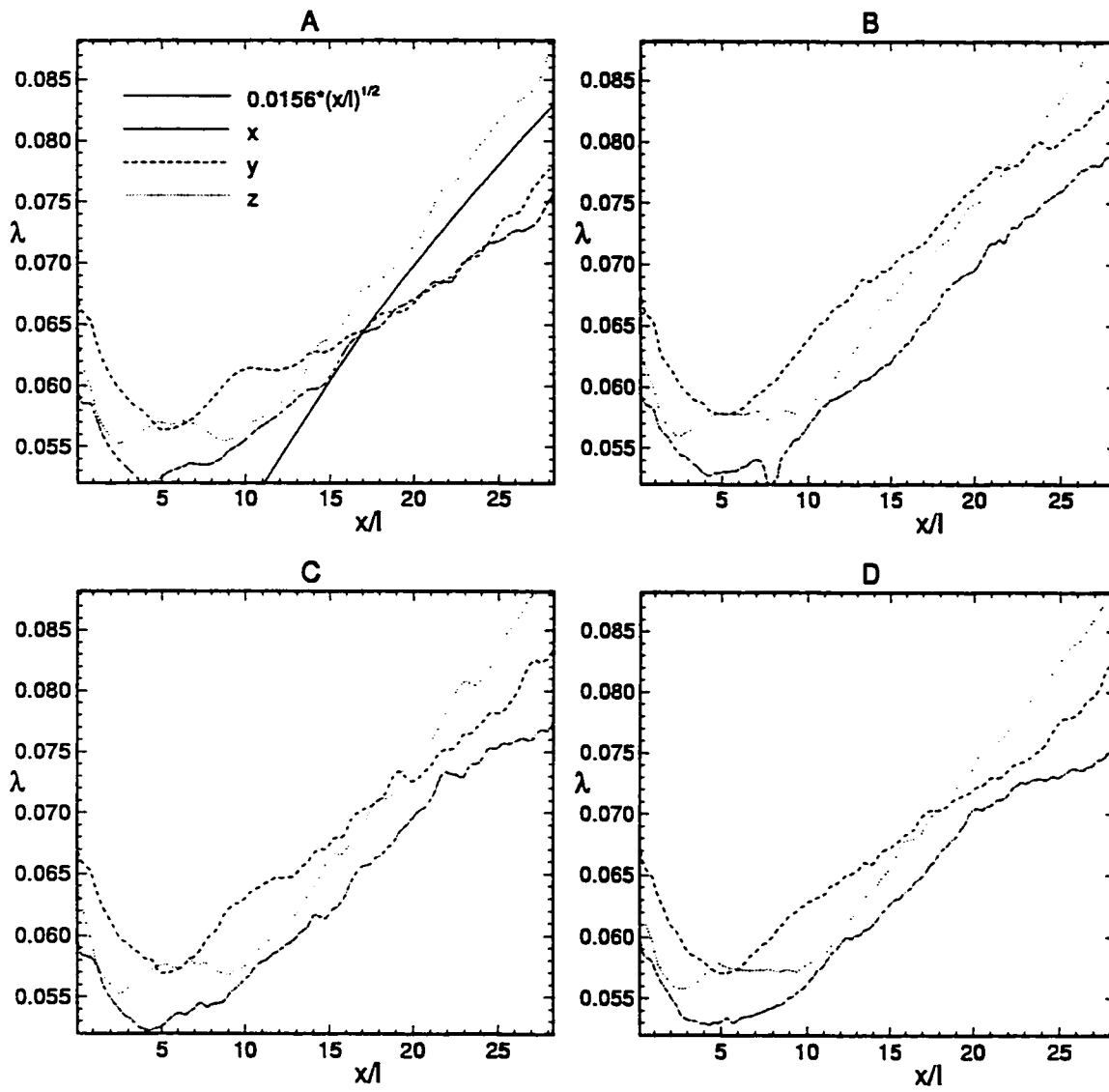


Figure 4.7: Taylor microscales vs distance downstream.

energy, the turbulence energy budget predicts that, with no heat release, all length scales should grow as $(x/l)^{1/2}$ [92]. The coefficient 0.0156, as well as coefficients for theoretical curves in subsequent plots, were determined by a visual fit to the data. It can be seen from the plots that the heat release has little effect on the growth of the Taylor microscales. There are several reasons for the peculiar behavior of the flow near the inlet. Setting the pressure derivative normal to the inlet to zero places an unphysical constraint on the eddies, i.e., the pressure gradient in the flow direction cannot adjust to balance the centrifugal force of the rotation. The viscosity of the flow is also a little different than the viscosity used to generate the inlet turbulent field; therefore, some adjustment of the energy spectrum must occur. Furthermore, the assumption of frozen turbulence is not quite correct, i.e., the velocity field being advected through the inlet represents a single instant in time of the temporal simulation. For these and possibly other reasons, the flow must undergo an adjustment near the inlet before expected decay patterns begin to occur.

Figure 4.8 shows the power law decay of turbulent kinetic energy. The straight line corresponds to the empirical decay law of $(x/l)^{1.25}$ reported by Comte-Bellot and Corrsin [15] for grid turbulence in a wind tunnel. The results show that, after some initial development, the simulated turbulent decay approximates the experimental data. Again, the decay of velocity fluctuations is nearly the same for all four cases. This insensitivity of velocity statistics to density variations was also demonstrated in Sandoval's simulations [86]. Figure 4.9 is a plot of the Taylor Reynolds numbers versus downstream distance. In the plots, R_λ is defined for each direction, i.e.,

$$R_{\lambda,i} = \frac{\lambda_i \sqrt{\langle u_i^2 \rangle}}{\nu} \quad (\text{no sum on } i) .$$

The Taylor Reynolds numbers decrease downstream but remain high enough so that each case may be considered turbulent throughout the domain [71].

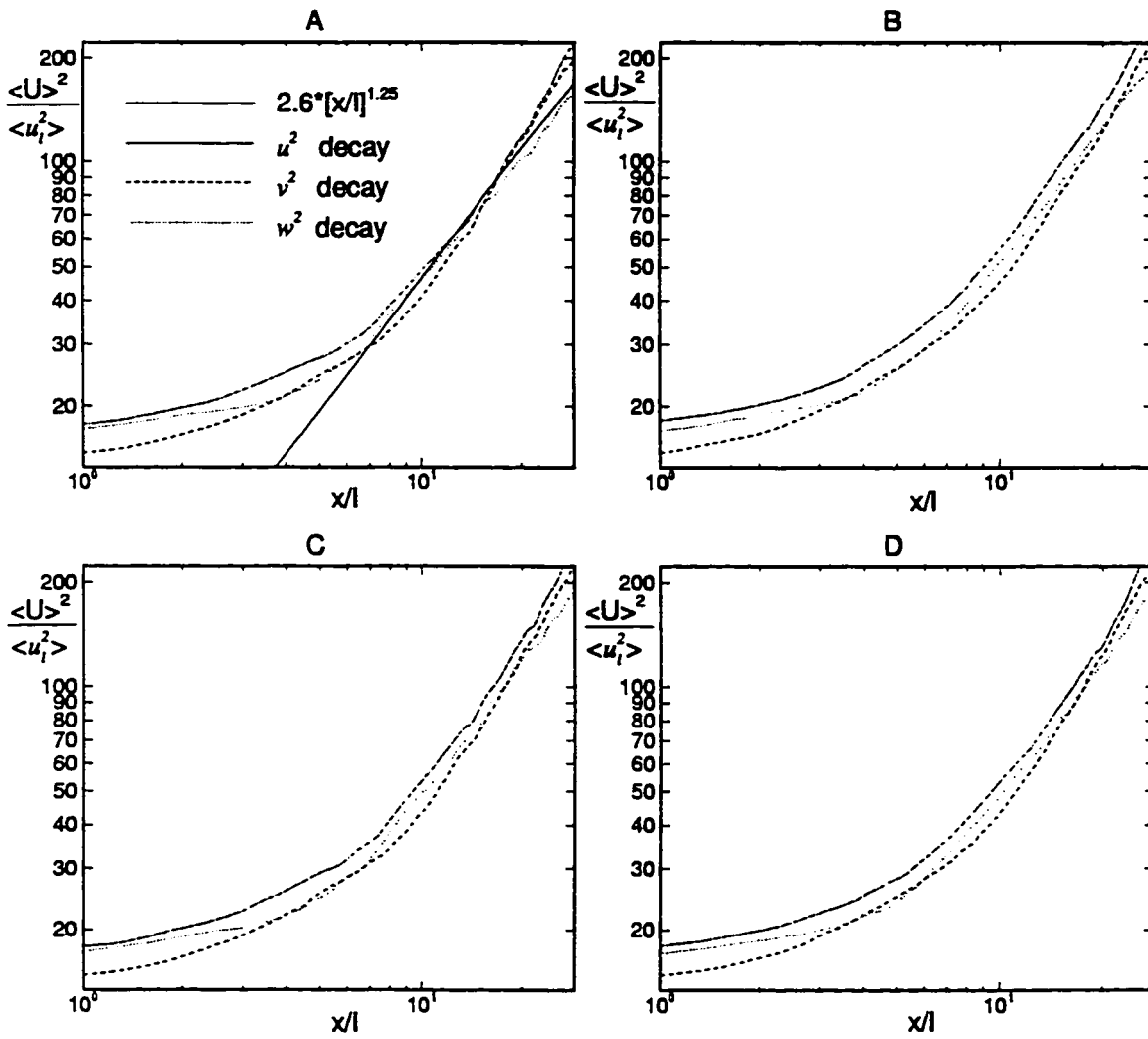


Figure 4.8: Centerline decay of turbulent kinetic energy.

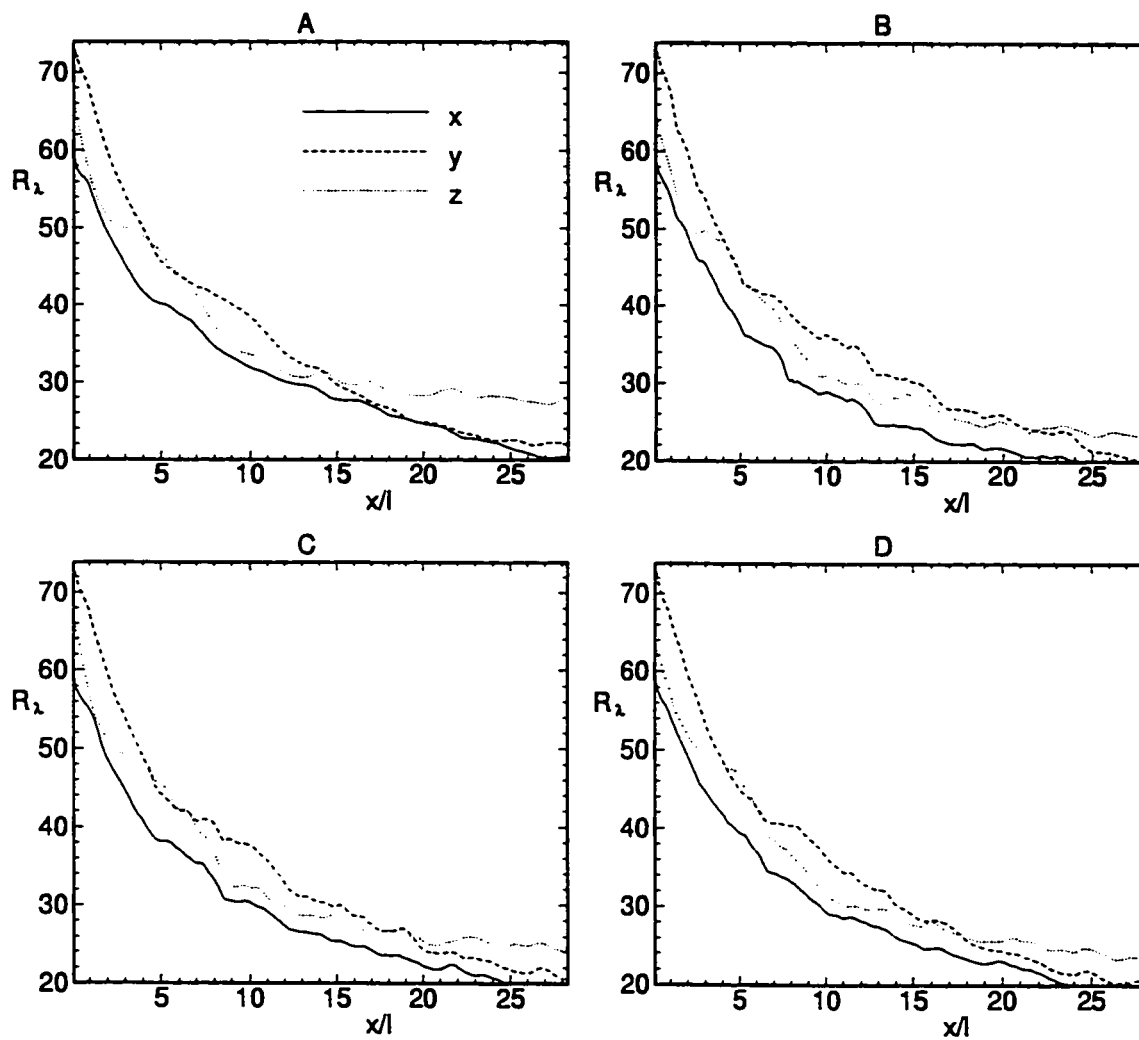


Figure 4.9: Taylor Reynolds numbers vs distance downstream.

4.4 Plume

Figure 4.10 depicts the decay of the mean value of ξ along the plume centerline as a function of initial large-eddy turnover time. The mean was computed by taking a time average over grid points within a distance of 4 grid spaces from the plume centerline. Brown and Bilger [8] report a decay law of t_{le}^{-1} and the plot shows that $\langle \xi^c \rangle$, from case A, decays as t_{le}^{-1} with an error bound of $100 \frac{|\langle \xi^c \rangle - 0.08/t_{le}|}{0.08/t_{le}} < 18\%$. The line corresponding to t_{le}^{-1} is not meant to imply that there was no scatter in the experimental data. The experimental scatter is not shown here for clarity. The other three cases appear to follow the same trends as case A, e.g., rising and falling in the same places. This is likely due to the fact that the inlet flow was the same for all four cases and heat release did not have a large effect on the flow. In figure 4.11 is plotted the decay of the root-mean-square value of ξ along the plume centerline. Brown and Bilger find an empirical decay law of $t_{le}^{-1.32}$ and from the plot it can be determined that, after one large eddy turnover, ξ_{rms}^c for case A approximates the experimental data with an error bound of $100 \frac{|\xi_{rms}^c - 0.09/t_{le}^{1.32}|}{0.09/t_{le}^{1.32}} < 37\%$. From random sampling theory, it is expected that the statistical scatter in the second moment of ξ^c will be greater than the error in the first moment.

Figure 4.12 shows the downstream growth of the standard deviation σ of the mean scalar profile, computed as follows: first, $\langle \xi(r, t_{le}) \rangle$ is computed at each downstream (eddy-time) location by averaging in time and over annular regions at specific radial positions; then σ is computed via numerical integration as

$$\sigma(t_{le}) = \left(\frac{\int_0^{L/2} r^2 \langle \xi(r, t_{le}) \rangle dr}{\int_0^{L/2} \langle \xi(r, t_{le}) \rangle dr} \right)^{1/2}.$$

The plume's spread is very close to the $t_{le}^{1/2}$ dependence expected from (i) the conservation of mixture fraction, (ii) an assumption of self-similar radial profiles for $\langle \xi \rangle$, and (iii) $\langle \xi^c \rangle$ having a decay exponent of -1. Brown and Bilger [8], Nakamura *et.*

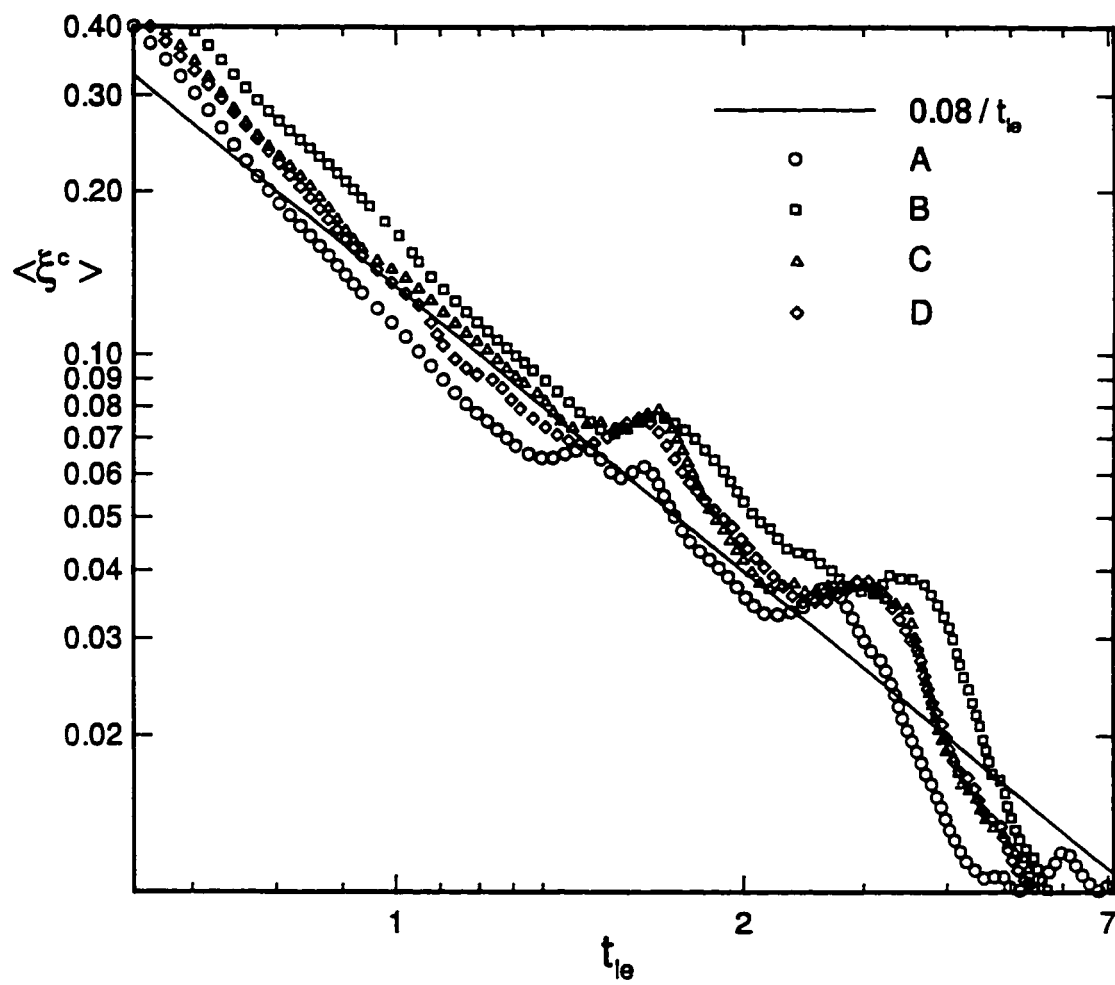


Figure 4.10: Mean mixture fraction along centerline.

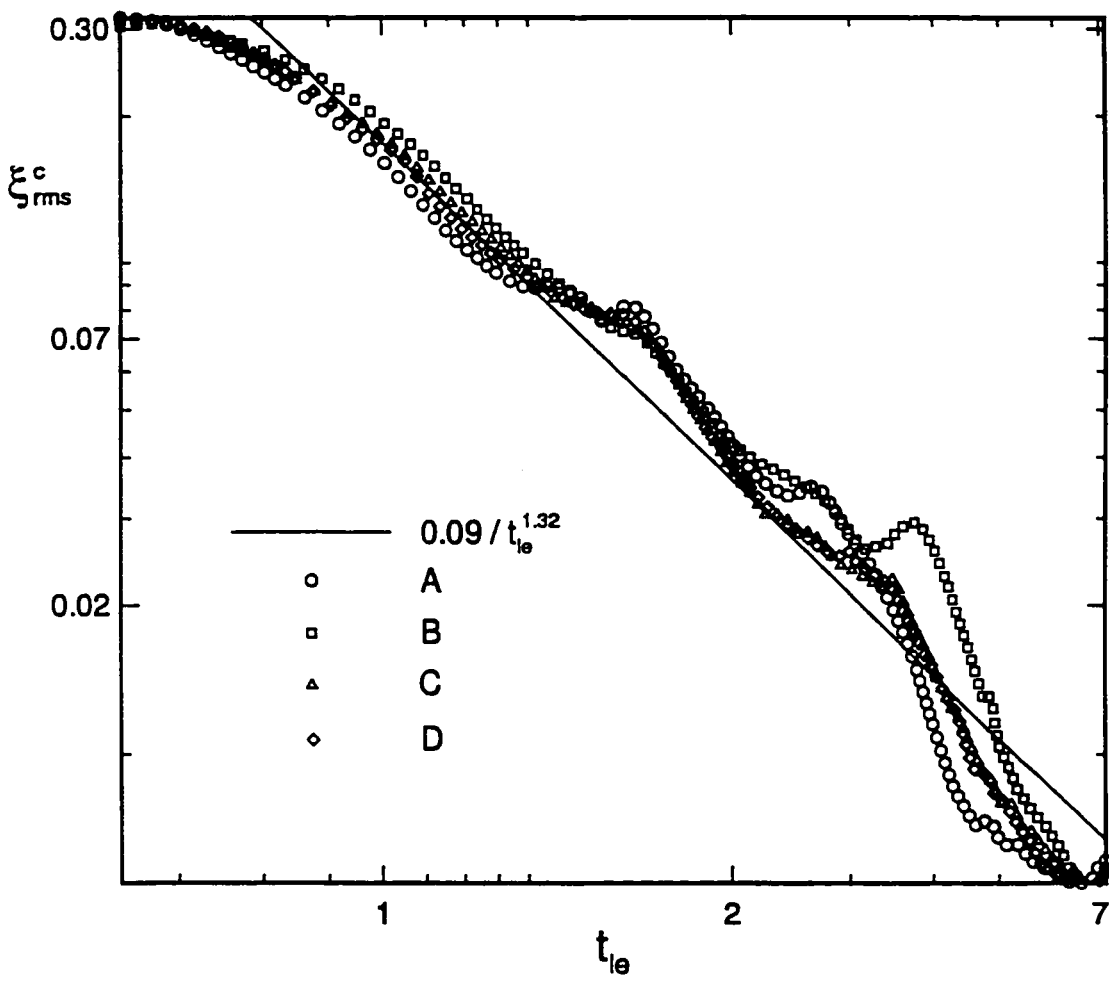


Figure 4.11: RMS of mixture fraction along centerline.

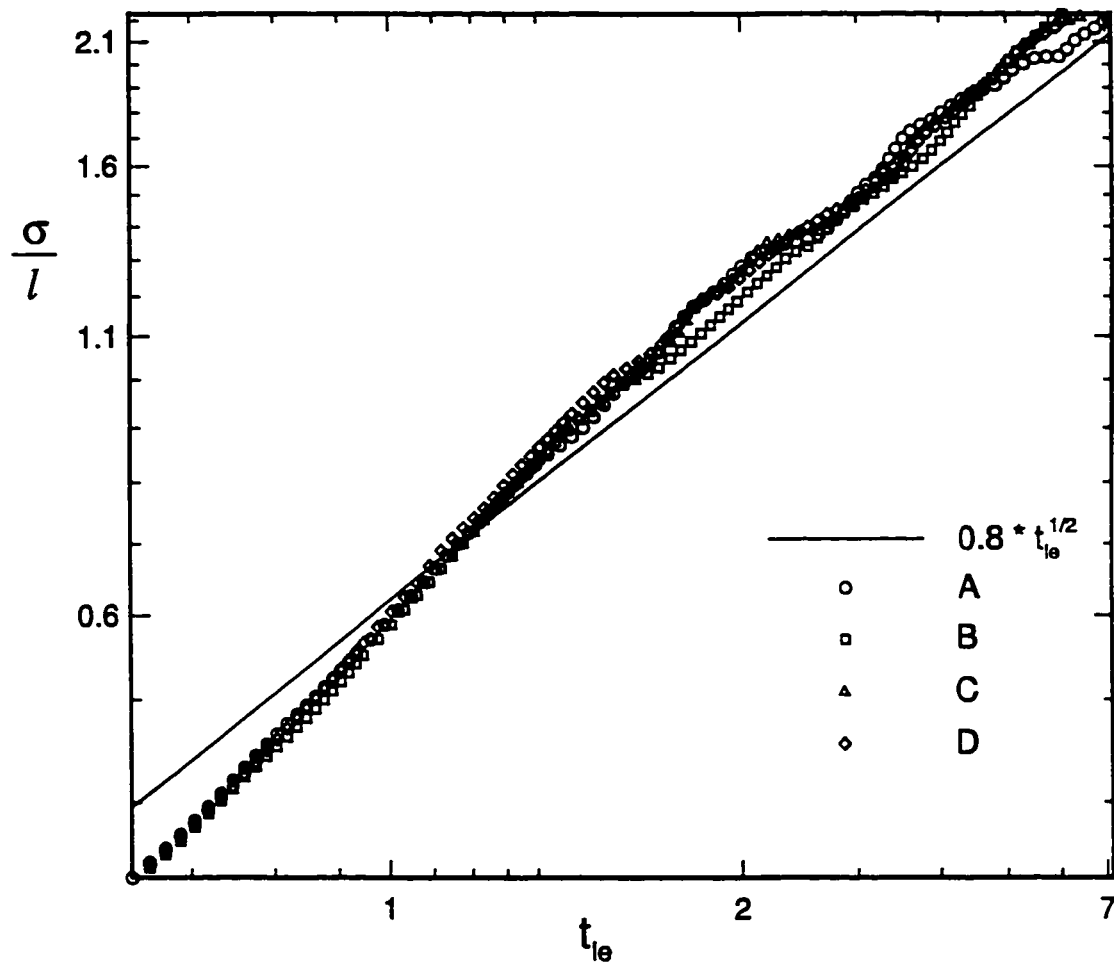


Figure 4.12: Standard deviation of mean scalar profile vs large eddy turnover time.

al. [70] and Komori and Ueda [42] all report growth exponents of 1/2. Some of the discrepancy in the plot may be due to the limited distance from the plume centerline to the side boundaries, which the plume eventually crosses.

4.5 Reactive Scalar

The centerline decay of the mean (time-averaged) fuel mass fraction is plotted in figure 4.13. Since the inlet concentrations differ from those of the Brown and Bilger experiment, a direct comparison cannot be made. For case A, the reaction is seen to occur approximately midway between the frozen and equilibrium chemistry limits. In the frozen limit $Y_f = Y_{f1}\xi$, while in the equilibrium chemistry limit

$$Y_f = \begin{cases} 0 & \text{if } \xi \leq \xi_{st} \\ Y_{f1} \frac{\xi - \xi_{st}}{1 - \xi_{st}} & \text{if } \xi > \xi_{st} \end{cases}$$

From cases C and D it can be seen how an increase in the activation temperature moves the reaction towards the frozen limit.

In figure 4.14 is plotted the root-mean-square of the centerline fuel mass fraction normalized by the mean value. It is interesting to note that the limits cross at approximately one large eddy turnover time. Unlike $\langle Y_f^c \rangle$, $Y_{f,rms}^c$ may lie outside the frozen and equilibrium limits and these limits may cross each other. This behavior is due to the triple correlation terms in the conservation equation for the scalar variance [9]. For $t_{le} > 1$ the reacting flow data lie between the frozen and equilibrium limits, but near the inlet they appear to follow the frozen chemistry curve. Case D is very near to the frozen limit until far downstream.

Figure 4.15 shows the mean centerline reaction rate versus large-eddy turnover time. For cases A, B, and C a rapid drop occurs near a time of 3 as the fuel is fully consumed. The low Damköhler number and high activation temperature of case D result in a slow rate of reaction compared to the other cases.

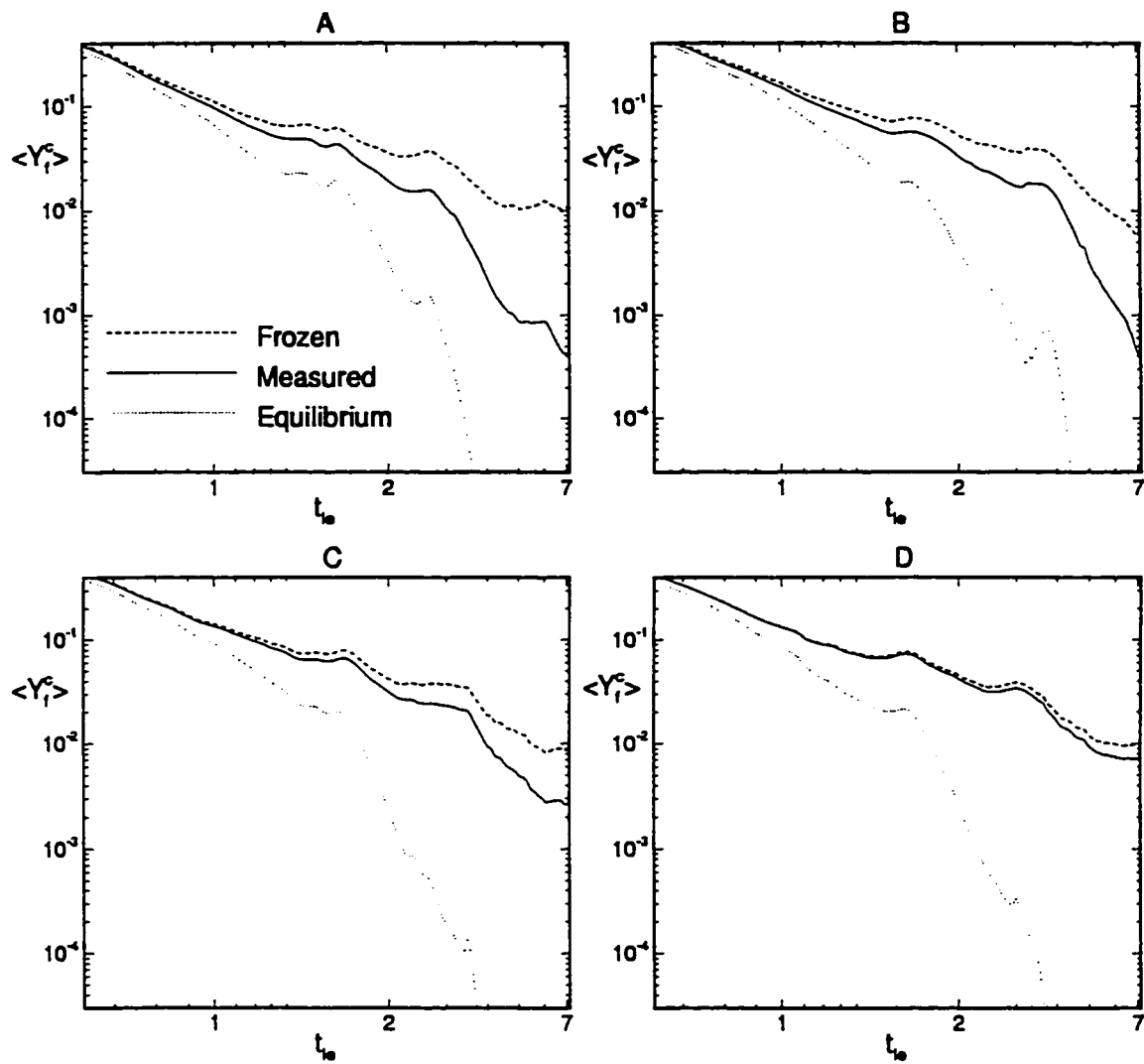


Figure 4.13: Mean and limiting values of fuel mass fraction along centerline.

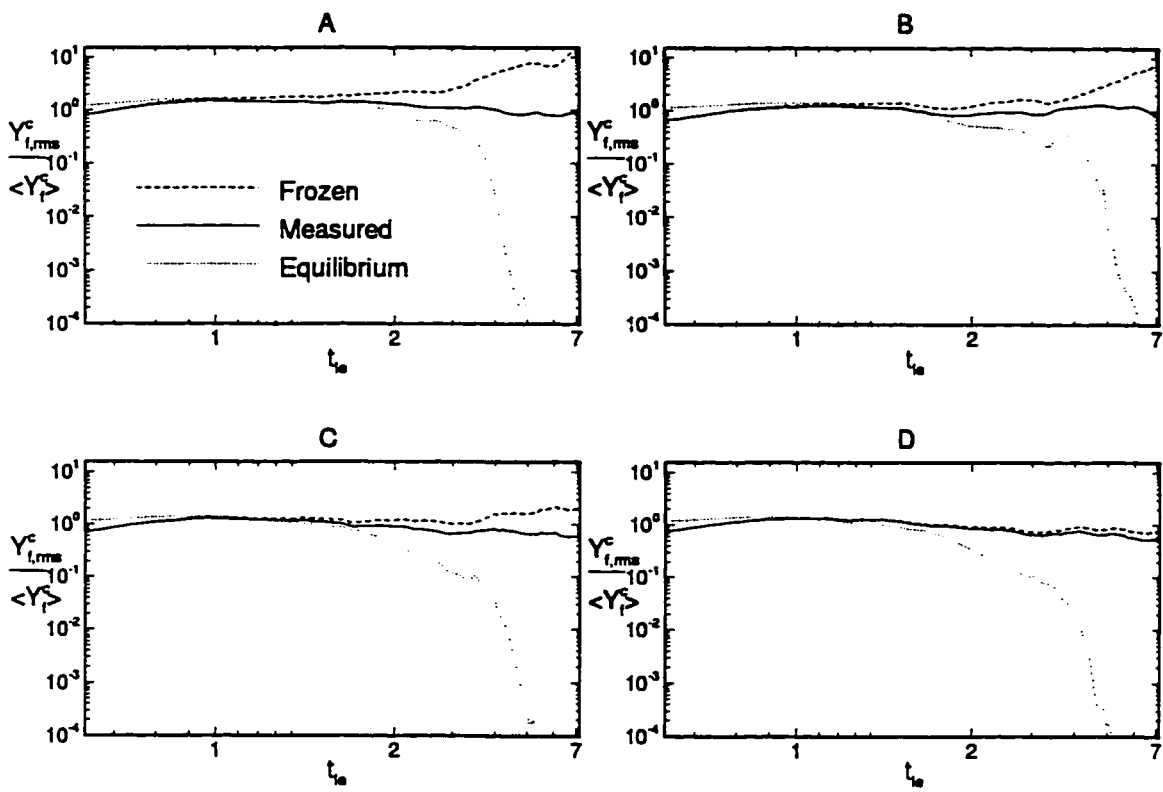


Figure 4.14: Fluctuation of fuel mass fraction along centerline.

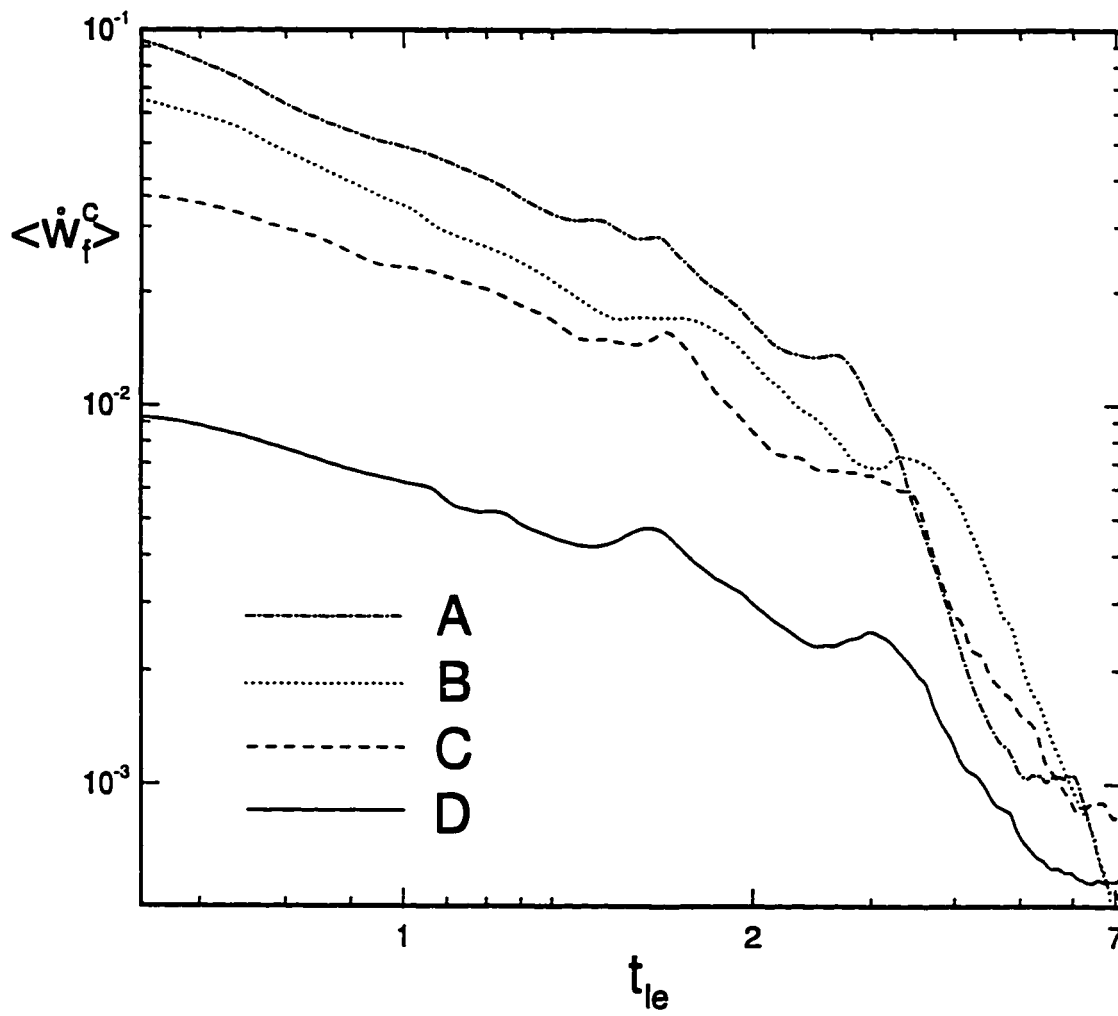


Figure 4.15: Mean centerline reaction rate.

4.6 Extinction

It is important to measure the strength of the reaction by examining its proximity to the extinction regime. The conditions for the extinction of a diffusion flame were first derived by Liñán [54] using activation-energy asymptotics. Williams [93] defines quenching criteria using a reduced Damköhler number, which is given below in terms of current variables:

$$Da_e \equiv DaPe \left(r\xi_{st} Y_{f1} e^{-\frac{T_a}{T_f}} \right) \left[\frac{T_f^2}{T_a(T_f - 1)} \right]^3 [2\xi_{st}(1 - \xi_{st})]^2 \left(\frac{\rho}{D \nabla \xi \cdot \nabla \xi} \right) |_{\xi=\xi_{st}} \quad (4.4)$$

where T_f is the adiabatic flame temperature, given by

$$T_f = \frac{Y_{o2} + rY_{f1} + Y_{f1}Y_{o2}\frac{\gamma-1}{\gamma}q}{Y_{o2} + rY_{f1}} \quad (4.5)$$

Extinction will occur when $Da_e \leq Da_E$, where

$$Da_E = \left[(1 - |\psi|) - (1 - |\psi|)^2 + 0.26(1 - |\psi|)^3 + 0.055(1 - |\psi|)^4 \right] e \quad (4.6)$$

If the temperatures of the fuel and oxidizer streams are equal, as in the present cases, then $\psi = 2\xi_{st} - 1$, thus $Da_E = 0.478$. Equations (4.4) and (4.6) provide the criteria for local flamelet extinction. The subscript $\xi = \xi_{st}$ indicates that Da_e is to be evaluated on the stoichiometric surface. It can be seen that if the quantity $\frac{D}{Pe} \nabla \xi \cdot \nabla \xi$, defined as the scalar dissipation rate, becomes too large, then extinction will occur. The scalar dissipation rate is approximately proportional to the square of the local strain rate, hence sufficiently large strain rates cause quenching of flamelets. Figure 4.16 is a scatter plot of Da_e at locations very near ξ_{st} . The data were taken from case D because the reaction for this case is closest to the extinction limit. The plot indicates that no flame quenching should be occurring.

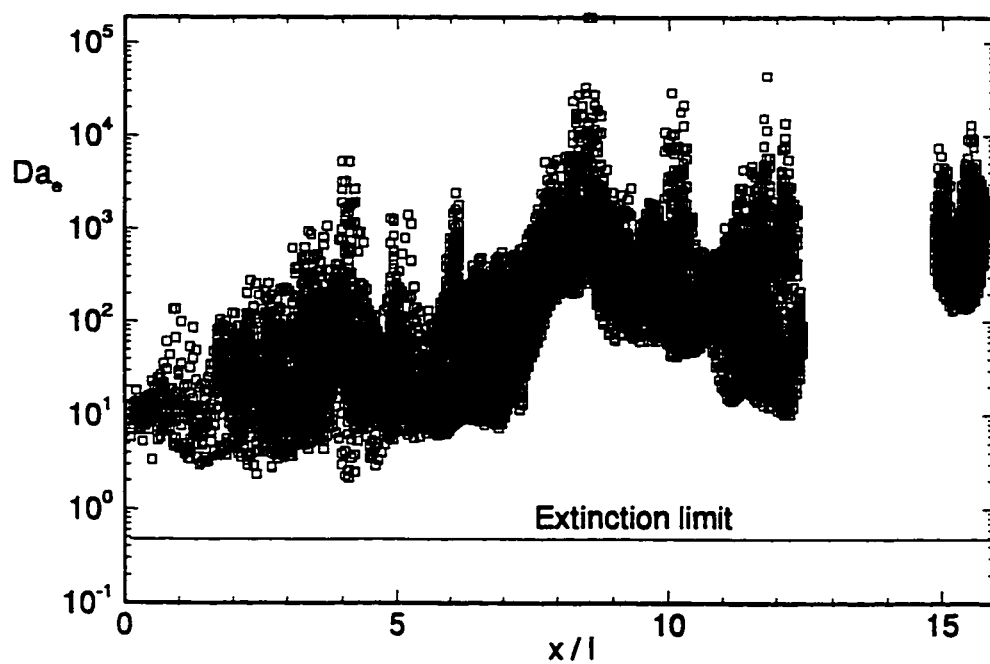


Figure 4.16: Proximity of reaction at stoichiometric locations to the extinction limit. Data taken from case D.

Part II

Subgrid-Scale Modeling

Chapter 5

DERIVATION OF RESOLVABLE FIELD EQUATIONS

5.1 Filtering

The purpose of this part of the thesis is to describe how LES may be used to compute turbulent flows with chemical reactions. In DNS, the Navier-Stokes equations are solved directly with Reynolds and Damköhler numbers low enough so that the variables of motion are fully resolved. This means that the grid spacing must be on the order of the Kolmogorov scale and the flame scale. In LES the small, unresolvable scales of motion are removed from the governing equations, thus eliminating the restrictions on Re and Da . The small scales are removed by applying a spatial filter to the governing equations [33]. The resulting ‘large eddy’ equations are then solved for the large-scale components of the primitive variables. The effects of small (subgrid-scale) motions on the large scales are modeled. A homogeneous filter operator is defined by the convolution integral

$$\bar{\phi}(\vec{x}) \equiv \int_{\mathcal{D}} G(|\vec{x} - \vec{x}'|; \Delta) \phi(\vec{x}') d\vec{x}' \quad (5.1)$$

where the subscript \mathcal{D} indicates that the integration is to be performed over the entire computational domain. The filter kernel G is normalized,

$$\int_{-\infty}^{\infty} G(r; \Delta) dr = 1 \quad (5.2)$$

and has a characteristic width Δ , which is directly related to the grid spacing of the LES computational mesh.

The manner of LES to be performed, and the definition of what is being solved for, depend on the way in which (5.1) is applied to the governing equations. As an example, consider a Cartesian coordinate system in which (5.1) is applied to an x derivative term. If G is chosen as a ‘top-hat’ function, then (5.1) may be applied as follows:

$$\begin{aligned}\frac{\overline{\partial\phi}}{\partial x} &= \int_y^{y+\Delta} \int_z^{z+\Delta} \int_x^{x+\Delta} \frac{\partial\phi}{\partial x'} dx' dy' dz' \\ &= \int_y^{y+\Delta} \int_z^{z+\Delta} [\phi(x = i + 1, y', z') - \phi(x = i, y', z')] dy' dz'\end{aligned}$$

Here, $x = i$ and $x = i + 1$ refer to the i and $i + 1$ grid nodes along the x direction. This approach, in which the equations are integrated between grid nodes, leads directly to a set of discretized equations and has been referred to as Schumann’s control volume method [88]. The variables are defined only at the grid nodes, and hence, this procedure can be thought of as ‘discrete’ filtering. This approach introduces four different types of averages: averages over the three types of faces on a grid cell and volume averages. A drawback to this method is the conceptual difficulty of relating surface to volume averages. This method was first introduced in the atmospheric sciences and is occasionally applied to engineering flows [2], [29].

A more common approach is to introduce a filter function that commutes with derivative operators. Such a procedure is sometimes called a ‘sliding’ filter. Taking the derivative of (5.1) with respect to x_j gives

$$\begin{aligned}\frac{\partial}{\partial x_j} \overline{\phi(\vec{x})} &= \int_{\mathcal{D}} \phi(\vec{x}') \frac{\partial}{\partial x_j} G(|\vec{x} - \vec{x}'|; \Delta) d\vec{x}' = - \int_{\mathcal{D}} \phi \frac{\partial G}{\partial x_j} d\vec{x}' \\ &= \int_{\mathcal{D}} G \frac{\partial\phi}{\partial x_j'} d\vec{x}' - \phi(\vec{x}') G(|\vec{x} - \vec{x}'|; \Delta) \Big|_{\text{boundaries}}\end{aligned}\quad (5.3)$$

since the limits of integration are considered fixed. In order that $\frac{\partial\overline{\phi}}{\partial x_j} = \overline{\frac{\partial\phi}{\partial x_j}}$, the last term on the right hand side of (5.3) must be zero. If the domain extends to infinity then this must be the case in order that (5.2) be satisfied. If the flow is bounded by

walls, then G may be imagined to take on some inhomogeneous form near the wall such that $\phi(\vec{x}')G(\vec{x}, \vec{x}'; \Delta)|_{boundaries} = 0$.

A convenient filter kernel is the Gaussian,

$$G(r; \Delta) = Ae^{-6r^2/\Delta^2}, \quad A = 1/\int_{-\infty}^{\infty} e^{-6r^2/\Delta^2} dr \quad (5.4)$$

since its shape is the same in both physical and wavenumber space. The numerical factors in (5.4) are such that the second moment of this filter is the same as that of a box filter of width Δ . Another filter, which plays an important role in theoretical considerations, is a sharp cutoff in Fourier space. The Fourier transform of (5.1) is

$$\widehat{\phi}(\vec{k}) = \widehat{G}(|\vec{k}|; \Delta)\widehat{\phi}(\vec{k}) . \quad (5.5)$$

For a spectral truncation filter,

$$\widehat{G}(|\vec{k}|; \Delta) = \begin{cases} 1 & \text{if } |\vec{k}| < k_c \\ 0 & \text{if } |\vec{k}| \geq k_c \end{cases}$$

where k_c is a cutoff wavenumber. In physical space this has the form of a damped sine wave.

5.2 The Large-Eddy Equations

For the subgrid-scale model to be discussed, it is convenient to recast (2.3) in terms of internal energy. Using the continuity and momentum equations, (2.3) can be rewritten as [1],

$$\frac{\partial \rho e}{\partial t} + \frac{\partial \rho e u_i}{\partial x_i} = -p \frac{\partial u_i}{\partial x_i} + \frac{1}{Re} \tau_{ij} \frac{\partial u_i}{\partial x_j} + \frac{1}{M^2 Re Pr} \frac{\partial}{\partial x_i} \left(\frac{\mu}{(\gamma - 1)} \frac{\partial T}{\partial x_i} \right) + \frac{q \dot{w}_f}{\gamma M^2} \quad (5.6)$$

where

$$T = \gamma M^2 (\gamma - 1) e \quad (5.7)$$

Applying the spatial filter (5.1) to equations (2.1), (2.2), (5.6), (2.15) and (2.6) gives

$$\frac{\partial \bar{p}}{\partial t} + \frac{\partial \overline{\rho u_i}}{\partial x_i} = 0 \quad (5.8)$$

$$\frac{\partial \overline{\rho u_i}}{\partial t} + \frac{\partial \overline{\rho u_i u_j}}{\partial x_j} = -\frac{\partial \bar{p}}{\partial x_i} + \frac{1}{Re} \frac{\partial \bar{\tau}_{ij}}{\partial x_j} \quad (5.9)$$

$$\frac{\partial \overline{\rho e}}{\partial t} + \frac{\partial \overline{\rho e u_i}}{\partial x_i} = -\bar{p} \frac{\partial \bar{u}_i}{\partial x_i} + \frac{1}{Re} \overline{\tau_{ij} \frac{\partial u_i}{\partial x_j}} + \frac{1}{M^2 Re Pr} \frac{\partial}{\partial x_i} \left(\frac{\mu}{\gamma - 1} \frac{\partial T}{\partial x_i} \right) + \frac{\overline{q \dot{w}_f}}{\gamma M^2} \quad (5.10)$$

$$\frac{\partial \overline{\rho \xi}}{\partial t} + \frac{\partial \overline{\rho \xi u_i}}{\partial x_i} = \frac{1}{Re Sc} \frac{\partial}{\partial x_i} \left(\mu \frac{\partial \xi}{\partial x_i} \right) \quad (5.11)$$

$$\bar{p} = \frac{\overline{\rho T}}{\gamma M^2} \quad (5.12)$$

These equations are simplified by recasting the variables as Favre-filtered quantities.

A Favre-filtered, i.e., density-weighted, variable is defined as

$$\tilde{\phi} = \frac{\overline{\rho \phi}}{\bar{\rho}}. \quad (5.13)$$

The flow field is thus decomposed into Favre-filtered (resolved) and subgrid-scale (unresolved) components, i.e., $\phi = \tilde{\phi} + \phi''$. Note that, in general, $\tilde{\tilde{\phi}} \neq \tilde{\phi}$ and therefore $\tilde{\phi}'' \neq 0$. Additionally, there are five terms that require special treatment: these are the viscous term in the momentum equation; the pressure-dilatation term, dissipation function, and conduction term in the energy equation; and the diffusive term in the scalar equation. Since viscosity is only a weak function of temperature, e.g., $\mu \sim T^{1/2}$, it is assumed that

$$\mu \approx \bar{\mu} \approx C_1 \frac{\tilde{T}^{3/2}}{\tilde{T} + C_2}, \quad C_1 = 1.3702213, \quad C_2 = 0.3702213. \quad (5.14)$$

This leads to the following approximations:

$$\bar{\tau}_{ij} \approx \bar{\mu} \left(\frac{\partial \tilde{u}_i}{\partial x_j} + \frac{\partial \tilde{u}_j}{\partial x_i} - \frac{2}{3} \delta_{ij} \frac{\partial \tilde{u}_k}{\partial x_k} \right) \quad (5.15)$$

$$\frac{\overline{\mu \frac{\partial T}{\partial x_i}}}{(\gamma - 1) \partial x_i} \approx \frac{\bar{\mu}}{(\gamma - 1)} \frac{\partial \tilde{T}}{\partial x_i} \quad (5.16)$$

$$\overline{\mu \frac{\partial \xi}{\partial x_i}} \approx \bar{\mu} \frac{\partial \tilde{\xi}}{\partial x_i} \quad (5.17)$$

Using (5.12) the pressure-dilatation term can be written

$$\overline{p \frac{\partial u_i}{\partial x_i}} = \frac{\bar{p}}{\gamma M^2} \tilde{T} \frac{\partial \tilde{u}_i}{\partial x_i} + \frac{\bar{p}}{\gamma M^2} \left[T \frac{\partial \tilde{u}_i}{\partial x_i} - \tilde{T} \frac{\partial \tilde{u}_i}{\partial x_i} \right]. \quad (5.18)$$

It has been argued that, in many flows of interest, the fluctuation Mach number of the small scales is small. The dilatation of the small scales is therefore negligible and the term in brackets may be dropped [26]. This assumption has been justified by examination of isotropic DNS data at various Mach numbers [67]. However, for reacting flows with a very large enthalpy of combustion, heat released at the small scales may result in significant small-scale temperature variations. Therefore, in order to neglect the term in brackets, it is probably necessary that q not be too large. Similarly, the dissipation function is written as

$$\overline{\tau_{ij} \frac{\partial u_i}{\partial x_j}} = \bar{\tau}_{ij} \frac{\partial \tilde{u}_i}{\partial x_j} + \left[\tau_{ij} \frac{\partial u_i}{\partial x_j} - \bar{\tau}_{ij} \frac{\partial \tilde{u}_i}{\partial x_j} \right]. \quad (5.19)$$

The term in brackets is typically neglected; however, such an approximation has yet to be investigated for reacting flows with heat release.

The above approximations lead to the following Favre-filtered equations:

$$\frac{\partial \bar{p}}{\partial t} + \frac{\partial \bar{\rho} \tilde{u}_i}{\partial x_i} = 0 \quad (5.20)$$

$$\frac{\partial \bar{\rho} \tilde{u}_i}{\partial t} + \frac{\partial \bar{\rho} \tilde{u}_i \tilde{u}_j}{\partial x_j} = -\frac{\partial \bar{p}}{\partial x_i} + \frac{1}{Re} \frac{\partial \bar{\tau}_{ij}}{\partial x_j} - \frac{\partial \sigma_{ij}}{\partial x_j} \quad (5.21)$$

$$\frac{\partial \bar{\rho} \tilde{e}}{\partial t} + \frac{\partial \bar{\rho} \tilde{e} \tilde{u}_i}{\partial x_i} = -\bar{p} \frac{\partial \tilde{u}_i}{\partial x_i} + \frac{1}{Re} \bar{\tau}_{ij} \frac{\partial \tilde{u}_i}{\partial x_j} + \frac{1}{M^2 Re Pr} \frac{\partial}{\partial x_i} \left(\frac{\bar{\mu}}{\gamma - 1} \frac{\partial \tilde{T}}{\partial x_i} \right) + \frac{q \bar{w}_f}{\gamma M^2} - \frac{\partial \alpha_i}{\partial x_i} \quad (5.22)$$

$$\frac{\partial \bar{\rho} \tilde{\xi}}{\partial t} + \frac{\partial \bar{\rho} \tilde{\xi} \tilde{u}_i}{\partial x_i} = \frac{1}{Re Sc} \frac{\partial}{\partial x_i} \left(\frac{\bar{\mu}}{\mu} \frac{\partial \tilde{\xi}}{\partial x_i} \right) - \frac{\partial \zeta_i}{\partial x_i} \quad (5.23)$$

$$\bar{p} = \frac{\bar{\rho} \tilde{T}}{\gamma M^2} \quad (5.24)$$

where:

$$\sigma_{ij} = \bar{\rho} (\overline{u_i u_j} - \tilde{u}_i \tilde{u}_j) \quad (5.25)$$

$$\alpha_i = \bar{\rho} (\overline{u_i e} - \tilde{u}_i \tilde{e}) \quad (5.26)$$

$$\zeta_i = \bar{\rho} (\overline{u_i \xi} - \tilde{u}_i \tilde{\xi}) \quad (5.27)$$

It should be noted that highly exothermic reactions may result in significant radiation transport. This may also restrict the range of q for which (5.22) is valid.

5.3 Closure

In order to close the set of large-eddy equations, models are needed for σ_{ij} , α_i , ζ_i and $\overline{\tilde{w}_f}$. In addition, a method is needed for predicting filtered values of the chemical species present in the flow, i.e., $\overline{Y_i}$. In turbulent combustion, large temperatures, and hence large viscosities, may result in partially laminar flow in various regions. Models for σ_{ij} , α_i and ζ_i should vanish in such locations. The dynamic model of Germano [32] utilizes spectral information in the large-scale field to extrapolate the small-scale stresses. A nice result of this is that the model gives 0 for laminar flows. Also, the dynamic model has the correct limiting behavior near walls and, except for problems of numerical instability, is capable of producing backscatter. Recently, a Lagrangian form [63] of the dynamic model has been shown to accurately predict the flux of turbulent kinetic energy toward the subgrid scales in DNS of compressible reacting flows with both constant and temperature dependent viscosity [81]. Hence, the dynamic model appears to be a promising candidate for use in reacting LES. In the next few sections, closures for σ_{ij} , α_i and ζ_i are presented that utilize recent improvements and extensions to the dynamic model. A new model for predicting $\overline{\tilde{w}_f}$ and $\overline{Y_i}$ is derived in the following chapter.

5.9.1 Modeling the Subgrid-Scale Stress Tensor

Taking the approach of Moin et al. [67], σ_{ij} is recast in terms of spatially filtered variables, i.e.,

$$\sigma_{ij} = \overline{\rho u_i u_j} - \frac{\overline{\rho u_i} \overline{\rho u_j}}{\overline{\rho}} \quad (5.28)$$

Applying a second 'test' filter to (5.9) gives rise to the test filtered stresses,

$$\psi_{ij} = \widehat{\overline{\rho u_i u_j}} - \frac{\widehat{\overline{\rho u_i}} \widehat{\overline{\rho u_j}}}{\widehat{\overline{\rho}}} . \quad (5.29)$$

An overbrace is here used to denote a quantity that has been filtered using a test filter of width $\widehat{\Delta} > \Delta$. The width of the first filter Δ is set by the grid spacing of the LES and hence is termed the 'grid' filter. For an anisotropic grid, Δ is usually chosen as $\Delta = (\Delta x \Delta y \Delta z)^{1/3}$ [27], although other types of averages have also been used [80]. Germano [32] found the optimum ratio of test and grid scales to be $\widehat{\Delta} / \Delta = 2$. Applying the test filter to (5.28) and subtracting it from (5.29) leads to [58]

$$L_{ij} = \psi_{ij} - \widehat{\sigma}_{ij} = \widehat{\left(\frac{\overline{\rho u_i} \overline{\rho u_j}}{\overline{\rho}} \right)} - \frac{\widehat{\overline{\rho u_i}} \widehat{\overline{\rho u_j}}}{\widehat{\overline{\rho}}} = \widehat{\overline{\rho u_i \tilde{u}_j}} - \frac{\widehat{\overline{\rho u_i}} \widehat{\overline{\rho u_j}}}{\widehat{\overline{\rho}}} \quad (5.30)$$

which may be directly calculated from the resolved fields. The dynamic model assumes a prescribed functional form for the small scales, and furthermore assumes that this form is independent of the filter width. Thus the grid and test scales are required to be in the inertial range. The prescribed function is usually a Smagorinsky model, although recently it has been demonstrated that Kolmogorov's model may be used, in conjunction with Smagorinsky's formula, to generate a family of dynamic models [12].

Using the trace-free Smagorinsky eddy viscosity model for both σ_{ij} and ψ_{ij} gives

$$\sigma_{ij} - \frac{1}{3} \delta_{ij} k_e = -C \overline{\rho} \Delta^2 |\tilde{S}| \left(\tilde{S}_{ij} - \frac{1}{3} \delta_{ij} \tilde{S}_{nn} \right) \quad (5.31)$$

$$\psi_{ij} - \frac{1}{3} \delta_{ij} K_e = -C \widehat{\overline{\rho}} \widehat{\Delta}^2 \left| \widehat{\tilde{S}} \right| \left(\widehat{\tilde{S}}_{ij} - \frac{1}{3} \delta_{ij} \widehat{\tilde{S}}_{nn} \right) \quad (5.32)$$

where

$k_e = \sigma_{kk}$ is twice the subgrid-scale, turbulent kinetic energy

$K_e = \psi_{kk}$ is twice the test-scale, turbulent kinetic energy

$$\begin{aligned}\tilde{S}_{ij} &= \frac{1}{2} \left(\frac{\partial \tilde{u}_i}{\partial x_j} + \frac{\partial \tilde{u}_j}{\partial x_i} \right) \\ |\tilde{S}| &= \left(2\tilde{S}_{lm}\tilde{S}_{lm} \right)^{1/2} \\ \widehat{\tilde{S}}_{ij} &= \frac{1}{2} \left(\frac{\partial \widehat{\tilde{u}}_i}{\partial x_j} + \frac{\partial \widehat{\tilde{u}}_j}{\partial x_i} \right) \\ \left| \widehat{\tilde{S}} \right| &= \left(2\widehat{\tilde{S}}_{lm}\widehat{\tilde{S}}_{lm} \right)^{1/2}\end{aligned}$$

The second term on the left hand side of (5.31) assures that the subgrid stress tensor is isotropic in the absence of shear. Note that $\tilde{S}_{kk} = 0$ in an incompressible flow. The 'constant' C is allowed to be a function of space and time and is determined by inserting (5.31) and (5.32) into (5.30) to get

$$L_{ij} - \frac{1}{3}\delta_{ij}L_{kk} = \widehat{CM}_{ij} - CZ_{ij} \quad (5.33)$$

where

$$M_{ij} = \Delta^2 \bar{\rho} |\tilde{S}| \left(\tilde{S}_{ij} - \frac{1}{3}\delta_{ij}\tilde{S}_{nn} \right) \quad (5.34)$$

$$Z_{ij} = \widehat{\Delta}^2 \widehat{\bar{\rho}} \left| \widehat{\tilde{S}} \right| \left(\widehat{\tilde{S}}_{ij} - \frac{1}{3}\delta_{ij}\widehat{\tilde{S}}_{nn} \right). \quad (5.35)$$

It is difficult to solve (5.33) for C , since it appears in the argument of the test filter integral. Therefore a means of approximating the C that appears under the overbrace in (5.33) is desirable. Piomelli and Liu [75] note that by filtering out the smallest scales of motion, the highest frequencies are also removed from the LES. Therefore, C is a slowly-varying function of time and may be estimated at timestep n via a first-order backward extrapolation, i.e.,

$$C \approx C_g = C^{n-1} + \Delta t \frac{\partial C}{\partial t} \approx C^{n-1} + \frac{t^n - t^{n-1}}{t^{n-1} - t^{n-2}} (C^{n-1} - C^{n-2}). \quad (5.36)$$

The C appearing under the overbrace in (5.33) is replaced by C_g , which is known. At this point (5.33) represents nine equations (five independent) in one unknown. This situation, in which C is over determined, is ironically opposite to the original closure problem. There are many ways in which (5.33) may be used to pick a value (or values) for C . Lilly [53] advocates a least squares fit that minimizes the error in (5.33). In this approach E_c is defined to be the square of the error in (5.33), i.e.,

$$E_c = (L_{ij} - \frac{1}{3}\delta_{ij}L_{kk} - \overbrace{C_g M_{ij}} + CZ_{ij})^2 \quad (5.37)$$

Setting $\partial E_c/\partial C = 0$ and solving for C gives

$$C = -\frac{\left(L_{ij} - \frac{1}{3}\delta_{ij}L_{kk} - \overbrace{C_g M_{ij}}\right) Z_{ij}}{Z_{mn}Z_{mn}} \quad (5.38)$$

This represents the minimum of E_c , since $\partial^2 E_c/\partial C^2 = 2Z_{ij}^2 > 0$.

In incompressible flows, k_e may be absorbed into the pressure and need not be modeled. This may also be done for low Mach number flows by absorbing k_e into the second-order or dynamic pressure, the first-order or thermodynamic pressure being constant. In these cases, a modified pressure is computed while the real pressure remains unknown. In high Mach number flows, however, the actual pressure must be computed in order to solve the energy equation. In this case, it is necessary to model k_e explicitly. The subgrid-scale kinetic energy may be parameterized using Yoshizawa's expression [95], i.e.,

$$k_e = C_I \bar{\rho} \Delta^2 |\tilde{S}|^2 . \quad (5.39)$$

Similarly, the test scale kinetic energy may be written as

$$K_e = C_I \widehat{\bar{\rho}} \widehat{\Delta}^2 \left| \widehat{\tilde{S}} \right|^2 . \quad (5.40)$$

Test filtering (5.39) and subtracting it from (5.40) yields

$$L_{ii} = K_e - \widehat{k_e} = \widehat{\bar{\rho} \tilde{u}_i \tilde{u}_i} - \frac{\widehat{\bar{\rho} \tilde{u}_i} \widehat{\bar{\rho} \tilde{u}_i}}{\widehat{\bar{\rho}}} . \quad (5.41)$$

Using (5.39) and (5.40) in (5.41) and solving for C_I leads to

$$C_I = \frac{\overline{\overline{\rho u_i \tilde{u}_i}} - (1/\overline{\overline{\rho}}) \overline{\overline{\rho u_i}} \overline{\overline{\rho \tilde{u}_i}} + \Delta^2 C_G \overline{\overline{\rho}} |\overline{\overline{\tilde{S}}}|^2}{\overline{\overline{\Delta}}^2 \overline{\overline{\rho}} |\overline{\overline{\tilde{S}}}|^2} \quad (5.42)$$

where

$$C_G = C_I^{n-1} + \frac{t^n - t^{n-1}}{t^{n-1} - t^{n-2}} (C_I^{n-1} - C_I^{n-2}), \quad (5.43)$$

again employing the suggestion of Piomelli and Liu.

5.3.2 Constraint on Eddy Viscosity

In the current modeling, the eddy viscosity is defined as

$$\mu_T = \frac{1}{2} C \overline{\overline{\rho}} \Delta^2 |\overline{\overline{\tilde{S}}}|. \quad (5.44)$$

The total viscosity is defined as $\mu_{tot} = \overline{\mu} + \mu_T$. Since negative total viscosities correlated over long times can lead to numerical instabilities, μ_{tot} must be constrained in an LES to be non-negative. By placing the stability constraint on μ_{tot} , rather than on C , the model is capable of producing a small amount of backscatter [75].

5.3.3 Subgrid-Scale Models for Heat Flux and Scalar Transport

In low Mach number flows, the second term on the left hand side of (5.10) is negligible and hence, no model is necessary for α_i [17]; however, in high Mach number flows α_i must be modeled. In order to derive a model for subgrid-scale heat flux, α_i is recast in terms of spatially filtered variables, i.e.,

$$\alpha_i = \overline{\overline{\rho u_i e}} - \frac{\overline{\overline{\rho u_i}} \overline{\overline{\rho e}}}{\overline{\overline{\rho}}}. \quad (5.45)$$

Now let Q_i denote the heat flux at the test filter scale, i.e.,

$$Q_i = \overline{\overline{\rho u_i e}} - \frac{\overline{\overline{\rho u_i}} \overline{\overline{\rho e}}}{\overline{\overline{\rho}}}. \quad (5.46)$$

Each is assumed to obey an eddy diffusivity model, i.e.,

$$\alpha_i = -\frac{C\bar{\rho}\Delta^2}{Pr_t} |\bar{S}| \frac{\partial \bar{e}}{\partial x_i} \quad (5.47)$$

$$Q_i = -\frac{C\widehat{\rho}\widehat{\Delta}^2}{Pr_t} \left| \widehat{S} \right| \frac{\partial \widehat{e}}{\partial x_i}, \quad (5.48)$$

where Pr_t is a turbulent Prandtl number and C is defined in (5.38). Let

$$\mathcal{L}_i = Q_i - \widehat{q}_i = \overbrace{\left(\frac{\widehat{\rho u_i} \widehat{\rho e}}{\widehat{\rho}} \right)} - \frac{\widehat{\rho u_i} \widehat{\rho e}}{\widehat{\rho}} = \widehat{\rho u_i} \widehat{e} - \frac{\widehat{\rho u_i} \widehat{\rho e}}{\widehat{\rho}} \quad (5.49)$$

which is directly computable from the LES variables. Pr_t is determined by substituting (5.47) and (5.48) into (5.49) to get

$$\mathcal{L}_i = \mathcal{R}_i - \frac{\Lambda_i}{Pr_t} \quad (5.50)$$

where

$$\mathcal{R}_i = \Delta^2 \frac{C\bar{\rho}}{Pr_g} |\bar{S}| \frac{\partial \bar{e}}{\partial x_i} \quad (5.51)$$

$$\Lambda_i = \widehat{\Delta}^2 C \widehat{\rho} \left| \widehat{S} \right| \frac{\partial \widehat{e}}{\partial x_i} \quad (5.52)$$

$$Pr_g = Pr_t^{n-1} + \frac{t^n - t^{n-1}}{t^{n-1} - t^{n-2}} (Pr_t^{n-1} - Pr_t^{n-2}). \quad (5.53)$$

Let Υ be defined as the square of the error in (5.50), i.e.,

$$\Upsilon = \left(\mathcal{L}_i + \frac{\Lambda_i}{Pr_t} - \mathcal{R}_i \right)^2 \quad (5.54)$$

Setting $\partial\Upsilon/\partial Pr_t = 0$ and solving for Pr_t gives

$$Pr_t = \frac{\Lambda_j \Lambda_j}{(\mathcal{R}_i - \mathcal{L}_i) \Lambda_i}. \quad (5.55)$$

A model for ζ_i is derived in the same way as the model for α_i , leading to

$$\zeta_i = -\frac{C\bar{\rho}\Delta^2}{Sc_t} |\tilde{S}| \frac{\partial \tilde{\xi}}{\partial x_i}. \quad (5.56)$$

Here Sc_t is a turbulent Schmidt number, given by

$$Sc_t = \frac{J_j J_j}{(N_i - L_i) J_i} \quad (5.57)$$

where

$$N_i = \Delta^2 \frac{C\bar{\rho}}{Sc_g} \overbrace{|\tilde{S}| \frac{\partial \tilde{\xi}}{\partial x_i}} \quad (5.58)$$

$$J_i = \widehat{\Delta}^2 \widehat{C} \widehat{\bar{\rho}} \left| \widehat{\tilde{S}} \right| \frac{\partial \widehat{\tilde{\xi}}}{\partial x_i} \quad (5.59)$$

$$Sc_g = Sc_t^{n-1} + \frac{t^n - t^{n-1}}{t^{n-1} - t^{n-2}} (Sc_t^{n-1} - Sc_t^{n-2}). \quad (5.60)$$

and C is given by (5.38).

Chapter 6

DERIVATION OF SUBGRID-SCALE CHEMISTRY MODEL

6.1 Reaction Zones

In order to construct models for $\overline{w_f}$ and $\overline{Y_i}$, it is first necessary to obtain an accurate physical description of the small scale reaction zones. Consider an LES grid cell in which chemical reactions are possibly taking place. Assume that the reactions occur in thin flames that are locally one-dimensional, and that the flow field is locally counterflow. The existence of a thin flame (a laminar flamelet) has been argued by Peters [73] based upon Da being large. The thin flame is located in the vicinity of the stoichiometric surface, defined by (2.18). Due to the dynamics of the scalar gradient vector, there is a strong tendency for the surfaces of constant ξ to align orthogonal to the most compressive principle axis of the strain rate field [71]. The most compressive strain axis is defined by the eigenvector that corresponds to the most negative eigenvalue of the rate-of-strain tensor. Similarly, the most extensional axis is defined by the eigenvector corresponding to the most positive eigenvalue. Let θ be the angle between the scalar gradient vector and the most compressive strain axis. Assuming that the scalar gradient is initially randomly oriented, i.e., that it is not aligned with the compressive strain axis, then by assuming a two-dimensional or axisymmetric straining field, it can be shown that θ goes to zero exponentially in time [83]. Using data from the temporal simulations of Mell [62], the PDF's of alignment for fully-developed turbulent and scalar fields are plotted in figure 6.1. In the figure, ϕ is the angle between the scalar gradient and the most extensional axis.

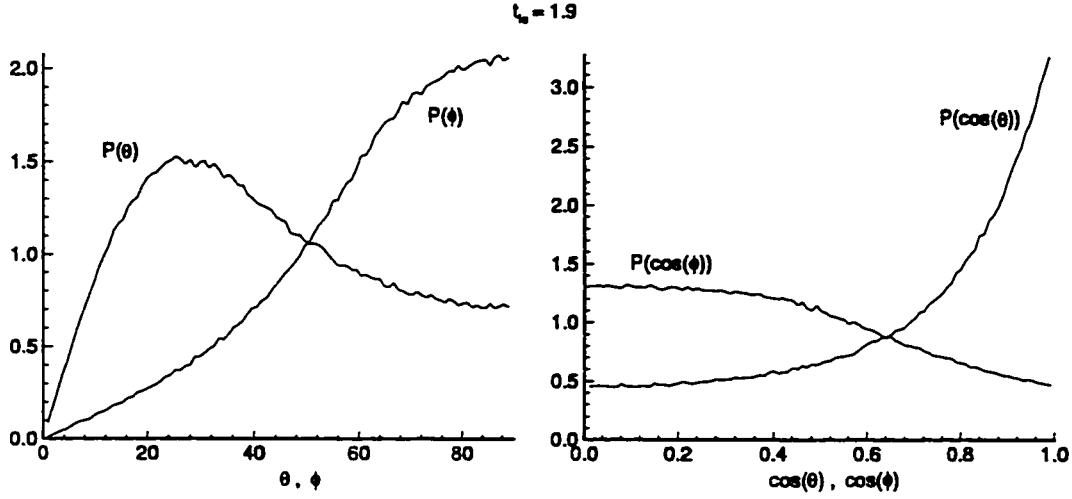


Figure 6.1: Probability Density Functions of angle between scalar gradient vector and most compressive strain axis (θ) and angle between scalar gradient and most extensional axis (ϕ).

The plots show a tendency for the scalar gradient vector to align orthogonal to the most extensional axis and parallel to the most compressive axis.

6.2 Laminar Flamelet Model

Recent experimental data have indicated that, for high Reynolds numbers and for Peclet numbers of order one and larger, the ξ -field consists of very thin regions of large χ , separated by regions of more uniform ξ [20]. Here χ is the scalar dissipation rate, which has been defined as $\chi = \frac{D}{P_e} \nabla \xi \cdot \nabla \xi$.

Assuming the flame is locally steady and that ξ is a monotonic function of the local coordinate normal to the flame, Y_f can be expressed in terms of ξ , and (2.4)

and (2.15) combine to give [73]

$$\rho\chi \frac{d^2 Y_f}{d\xi^2} = \dot{w}_f. \quad (6.1)$$

The effects of the local turbulent straining field are contained in ξ and χ . Four terms originally present in (6.1) have been neglected. The removal of these terms is based on the assumption that Da or T_a is large, which causes the reaction zone width in ξ -space to be small. In such cases, the second derivative and reaction rate terms dominate the equation. Some evidence suggests that the unsteady term $\rho\partial Y_f/\partial t$, which has been neglected, may be important during the early stages of mixing or when turbulent stirring is vigorous. Possible errors resulting from dropping the time derivative are discussed in a later section.

6.3 Counterflow Model

Before (6.1) can be solved, it is first necessary to assume a form for the ξ dependence of χ . By examining a small region downstream in a turbulent jet, Southerland and Dahm [90] have shown that mixing takes place in thin, strained layers where the scalar dissipation rate χ takes on the form

$$\chi = \chi_o F(\xi) \quad (6.2)$$

where F is given by the one-dimensional counterflow expression

$$F(\xi) = \begin{cases} \exp(-2[\operatorname{erf}^{-1}(2\frac{\xi-\xi^-}{\xi^+-\xi^-} - 1)]^2) & \text{if } \xi^- \leq \xi \leq \xi^+ \\ 0 & \text{if } \xi < \xi^- \text{ or } \xi > \xi^+ \end{cases} \quad (6.3)$$

Here χ_o is the local peak value of $\frac{D}{P_e} \nabla \xi \cdot \nabla \xi$ within the layer, erf^{-1} is the inverse error function (not the reciprocal), and ξ^- and ξ^+ represent local minimum and maximum values of ξ across the layer, i.e., locations in the flow where $\nabla \xi = 0$. Using DNS data, it will be argued in Section 7.4 that it is acceptable to choose $\xi^- = 0$ and $\xi^+ = 1$, and hence to disregard the dependence of F on ξ^- and ξ^+ .

6.4 The Case of Unity Lewis Number

In cases where $Le = 1$, the number of parameters in (6.1) can be reduced by relating T , and hence ρ and D , to ξ and Y_f . This is accomplished by using the definition of total enthalpy

$$H = \frac{\gamma}{\gamma - 1} T + \sum_{i=1}^N h_i Y_i \quad (6.4)$$

where N is the total number of chemical species present in the flow. For the present case, $N = 3$ and the summation is over the fuel, oxidizer and product. If the flow is in an open domain and if the Mach number is low, then H satisfies the equation [51],

$$\frac{\partial \rho H}{\partial t} + \frac{\partial \rho H u_j}{\partial x_j} = \frac{1}{Re Pr} \frac{\partial}{\partial x_j} \left(\mu \frac{\partial H}{\partial x_j} \right). \quad (6.5)$$

Also neglected in (6.5) are radiant heat transfer and work due to body forces. If $Pr = Sc$ then (6.5) is identical to (2.15) and therefore, H is linearly related to ξ , assuming that the initial or inflow conditions are consistent. The relationship between H and ξ is given by

$$H = \left[\frac{\gamma}{\gamma - 1} (T_{f1} - T_{o2}) + h_f Y_{f1} - h_o Y_{o2} \right] \xi + \frac{\gamma}{\gamma - 1} T_{o2} + h_o Y_{o2} \quad (6.6)$$

where T_{f1} is the temperature of the fuel feed and T_{o2} is the temperature of the oxidant feed. Using (2.10), (2.14), (2.16) and (6.6), T can be expressed as a function of Y_f and ξ

$$T = \frac{(\gamma - 1)}{\gamma} q (Y_{f1} \xi - Y_f) + T_{o2} + (T_{f1} - T_{o2}) \xi \quad (6.7)$$

For low Mach number combustion in an open domain, ρ is related to T through (2.32) (the thermodynamic pressure is constant). Also, in the absence of differential diffusion, $D = \nu$, therefore the diffusivity is related to T through (2.8). Hence, D , ρ and T are known in terms of ξ and Y_f .

Using (6.2) and (6.3) and the boundary conditions:

$$Y_f(\xi = 0, \chi_o) = 0 \quad (6.8)$$

$$Y_f(\xi = 1, \chi_o) = Y_{fi} \quad (6.9)$$

equation (6.1) can be solved to obtain $Y_f(\xi, \chi_o)$. Equations (6.8) and (6.9) apply to both the equilibrium and frozen chemistry functions for $Y_f(\xi)$. They are assumed to be appropriate for the current model even if fresh fuel and/or oxidizer are not present within the LES grid cell.

6.5 The Large Eddy Probability Density Function

By assuming that reactions occur in thin regions of one-dimensional counterflow, the ξ dependence of χ is known (see equations (6.2) and (6.3)). Furthermore, by assuming that $\xi^- = 0$ and $\xi^+ = 1$, χ_o then represents the value of χ where $\xi = 0.5$. The modeling thus implies that χ_o is independent of ξ , therefore $\overline{Y_f}$ can be expressed as

$$\overline{Y_f} = \int_0^1 \int_{\chi_o^{\min}}^{\chi_o^{\max}} Y_f(\xi, \chi_o) P(\chi_o) P(\xi) d\chi_o d\xi \quad (6.10)$$

where χ_o^{\min} and χ_o^{\max} are the minimum and maximum values of χ_o within the grid cell. Gao and O'Brien [31] refer to $P(\xi)$ as a 'Large Eddy Probability Density Function' (LEPDF) since it gives the frequency distribution of ξ within an LES grid cell.

At this point it is necessary to make use of an observation similar to one made by Kuznetsov and Sabel'nikov [44] which is that, within the interval of integration $\chi_o^{\min} \leq \chi_o \leq \chi_o^{\max}$, Y_f is a weak, approximately linear, function of χ_o . Therefore, $Y_f(\xi, \chi_o)$ can be approximated by the first two terms in the Taylor series expansion about the average of χ_o , i.e.,

$$Y_f(\xi, \chi_o) \approx Y_f(\xi, \overline{\chi_o}) + \left. \frac{\partial Y_f}{\partial \chi_o} \right|_{\overline{\chi_o}} (\chi_o - \overline{\chi_o}) . \quad (6.11)$$

Inserting (6.11) into (6.10) and integrating over χ_o gives

$$\overline{Y_f} = \int_0^1 Y_f(\xi, \overline{\chi_o}) P(\xi) d\xi . \quad (6.12)$$

Similar relationships can be obtained for \overline{Y}_o and for \overline{Y}_p . Note that \overline{Y}_f is obtained by integrating over χ_o rather than χ . The model is therefore likely to be sensitive only to the range of peak dissipation rates within a grid cell. The range of χ_o within an LES grid cell should be much lower than the range of χ , thus it is likely that (6.11) is a good assumption.

The integral in (6.12) is performed by assuming a Beta-distribution for $P(\xi)$, i.e.,

$$P(\xi) = \frac{\xi^{a-1}(1-\xi)^{b-1}}{B(a,b)}, \quad a = \bar{\xi} \left[\frac{\bar{\xi}(1-\bar{\xi})}{\xi_v^2} - 1 \right], \quad b = a/\bar{\xi} - a, \quad \xi_v^2 = \bar{\xi}^2 - \bar{\xi}^2 \quad (6.13)$$

where $B(a,b)$ is the Beta function and ξ_v^2 is the subgrid-scale variance. Note that $\overline{\xi^2} \equiv \overline{(\xi - \bar{\xi})^2} = \bar{\xi}^2 - 2\bar{\xi}\bar{\xi} + \bar{\xi}^2$ is not necessarily equal to ξ_v^2 . In filtering DNS fields, in order to simulate LES data, the subgrid variance should be computed as the mean-of-the-square minus the square-of-the-mean, rather than as the mean-square of the fluctuation. The latter approach is incompatible with the Beta model for the LEPDF and has been found to cause errors in the results. Furthermore, in the Beta-PDF model, $\bar{\xi}$ and ξ_v^2 represent the first two moments of a random variable. This means that the filter kernel $G(r; \Delta)$ should be positive definite in physical space [31], [16]. For example, a Fourier truncation filter is not appropriate for evaluating the present model, since Gibb's phenomenon may cause $\bar{\xi}$ to lie outside the range $0 \leq \bar{\xi} \leq 1$.

It is assumed that (6.12) and (6.13) remain unchanged if $\tilde{\xi}$, $\tilde{\xi}^2$ and $\tilde{\chi}_o$ are used in place of $\bar{\xi}$, $\bar{\xi}^2$ and $\bar{\chi}_o$. In this case, it may be assumed that \tilde{Y}_f rather than \overline{Y}_f is being modeled. Finally, $\tilde{\chi}_o$ must be related to $\bar{\chi}$ in order to make use of existing models. This is done by averaging (6.2) to get

$$\tilde{\chi}_o = \frac{\bar{\chi}}{\int_0^1 F(\xi)P(\xi)d\xi}. \quad (6.14)$$

6.6 Modeling the Scalar Variance and Dissipation Rate

The assumed forms for $\chi(\xi)$ and $P(\xi)$, i.e., (6.2) and (6.13), require $\bar{\xi}$, $\bar{\xi}^2$ and $\bar{\chi}$ (or $\tilde{\xi}$, $\tilde{\xi}^2$ and $\tilde{\chi}$) as inputs. In an LES, (5.23) is solved for $\tilde{\xi}$. There are several different ways of obtaining $\bar{\xi}^2$, or equivalently ξ_v^2 . One method is to use a similarity [3], [55], [16] or dynamic model. Following the same procedure as that used to model k_e yields

$$\xi_v^2 = C_\xi \bar{\rho} \Delta^2 |\tilde{\mathcal{Z}}|^2 \quad (6.15)$$

where

$$C_\xi = \frac{\overline{\bar{\rho} \tilde{\xi}^2} - (1/\overline{\bar{\rho}}) \left(\overline{\bar{\rho} \tilde{\xi}} \right)^2 + \Delta^2 \overline{C_s \bar{\rho}} |\tilde{\mathcal{Z}}|^2}{\overline{\Delta^2 \bar{\rho}} \left| \overline{\tilde{\mathcal{Z}}} \right|^2}$$

$$C_s = C_\xi^{n-1} + \frac{t^n - t^{n-1}}{t^{n-1} - t^{n-2}} (C_\xi^{n-1} - C_\xi^{n-2})$$

$$|\tilde{\mathcal{Z}}|^2 = \nabla \tilde{\xi} \cdot \nabla \tilde{\xi}$$

$$\left| \overline{\tilde{\mathcal{Z}}} \right|^2 = \nabla \overline{\tilde{\xi}} \cdot \nabla \overline{\tilde{\xi}} .$$

Another approach would be to integrate the governing equation for $\tilde{\xi}^2$. Multiplying (2.15) by ξ and Favre filtering leads to

$$\frac{\partial \overline{\bar{\rho} \xi^2}}{\partial t} + \frac{\partial \overline{\bar{\rho} \tilde{u}_i \xi^2}}{\partial x_i} = \frac{1}{Pe} \frac{\partial}{\partial x_i} \left(\overline{\bar{\mu} \frac{\partial \xi^2}{\partial x_i}} \right) - 2 \overline{\bar{\rho} \tilde{\chi}} - \frac{\partial \eta_i}{\partial x_i} \quad (6.16)$$

where

$$\overline{\bar{\rho} \tilde{\chi}} = \frac{1}{Pe} \overline{\bar{\rho} D \frac{\partial \xi}{\partial x_i} \frac{\partial \xi}{\partial x_i}} \approx \frac{\bar{\mu}}{Pe} \overline{\frac{\partial \xi}{\partial x_i} \frac{\partial \xi}{\partial x_i}} \quad (6.17)$$

$$\eta_i = \bar{\rho} \left(\overline{u_i \xi^2} - \tilde{u}_i \xi^2 \right) . \quad (6.18)$$

In solving (6.16), η_i could be modeled in the same manner as ζ_i . If (6.16) is used to obtain $\bar{\xi}^2$, then, depending on the flow, it may be useful to employ (6.15) to set the initial condition. In this case C_s , and hence C_ξ , would be determined by iteration.

The filtered scalar dissipation rate is commonly approximated using a model proposed by Schmidt and Schumann [87], i.e.,

$$\bar{\chi} = C_d \frac{\xi_v^2}{\Delta} \sqrt{\frac{k_e}{2\bar{\rho}}}, \quad C_d \approx 1. \quad (6.19)$$

Recently, Girimaji and Zhou [35] have pointed out that (6.19) acts as a sink of ξ^2 energy at all wavenumbers and at all times. They show that this property is inconsistent with results from DNS data. They furthermore note that (6.19) makes no use of the additional information about the supergrid scalar field available in an LES. Using the fact that the net energy transfer is local in wavenumber space, they derived a model for $\bar{\chi}$ that is local in physical space. In their approach, the filtered scalar dissipation is decomposed into three parts as follows:

$$\bar{\mu} \frac{\overline{\partial \xi}}{\partial x_i} \frac{\overline{\partial \xi}}{\partial x_i} = \bar{\mu} \frac{\overline{\partial \xi}}{\partial x_i} \frac{\overline{\partial \xi}}{\partial x_i} + \bar{\mu} \frac{\overline{\partial \xi'}}{\partial x_i} \frac{\overline{\partial \xi'}}{\partial x_i} + 2\bar{\mu} \frac{\overline{\partial \xi}}{\partial x_i} \frac{\overline{\partial \xi'}}{\partial x_i}. \quad (6.20)$$

The first term on the RHS of (6.20) is the scalar dissipation rate due to interactions among the resolved scales and is directly computable from the resolved field. The second term on the RHS of (6.20) represents the scalar dissipation caused by interactions among the small scales. This term is always positive and may be modeled as

$$\bar{\mu} \frac{\overline{\partial \xi'}}{\partial x_i} \frac{\overline{\partial \xi'}}{\partial x_i} = \mu_T \frac{\overline{\partial \xi}}{\partial x_i} \frac{\overline{\partial \xi}}{\partial x_i} \quad (6.21)$$

where μ_T is given by (5.44). The last term on the RHS of (6.20) represents the dissipation due to interactions between resolved and unresolved scales. This term can be either positive or negative and is responsible for backscatter of ξ energy from small to large scales. Girimaji and Zhou proposed modeling the backscatter term as

$$2\bar{\mu} \frac{\overline{\partial \xi}}{\partial x_i} \frac{\overline{\partial \xi'}}{\partial x_i} = -C_{\beta\bar{\rho}} \frac{[k_e/(2\bar{\rho})]^3}{\epsilon^2} \left(\frac{\overline{\partial \xi}}{\partial x_i} \frac{\overline{\partial^2(\bar{u}_j \bar{\xi})}}{\partial x_i \partial x_j} - \frac{\overline{\partial \xi}}{\partial x_i} \frac{\overline{\partial^2(\bar{u}_j \bar{\xi}')}}{\partial x_i \partial x_j} \right) \quad (6.22)$$

where ϵ is the mechanical dissipation rate, which may be modeled as [87]

$$\epsilon = C_e \frac{[k_e/(2\bar{\rho})]^{3/2}}{\Delta}, \quad C_e \approx 0.845. \quad (6.23)$$

In (6.22), C_β is a constant yet to be determined. It is assumed that filtered quantities in (6.20), (6.21) and (6.22) may be replaced by their Favre-filtered counterparts.

6.7 Summary of Methodology

The model is applied in an LES by first constructing tables for \overline{Y}_f and \overline{w}_f based on $\overline{\xi}$, ξ_v^2 and $\overline{\chi}$. The steps in constructing the model libraries are as follows:

1. Use (2.8), (2.32) and (6.7) to relate D , ρ and T to ξ and Y_f .
2. Choose a value for $\overline{\chi}_o$.
3. Plug (6.3) into (6.2) and (6.2) into (6.1) and use the boundary conditions (6.8) and (6.9) to solve for $Y_f(\xi, \overline{\chi}_o)$. This can be accomplished numerically using either a shooting or a relaxation scheme [78].
4. Use $Y_f(\xi, \overline{\chi}_o)$ along with equations (2.32), (2.16) and (6.7) to compute $\dot{w}_f(\xi, \overline{\chi}_o)$.
5. Choose values for $\overline{\xi}$ and ξ_v^2 .
6. Use (6.13) to solve for $P(\xi)$.
7. Insert $F(\xi)$ and $P(\xi)$ into (6.14) and solve for $\overline{\chi}$ (assuming $\xi^- = 0$ and $\xi^+ = 1$).
8. Plug $Y_f(\xi, \overline{\chi}_o)$ and $P(\xi)$ into (6.12) and integrate numerically to obtain $\overline{Y}_f(\overline{\xi}, \xi_v^2, \overline{\chi})$.
9. Obtain the filtered reaction rate in a similar fashion from the integral

$$\overline{w}_f = \int_0^1 \dot{w}_f(\xi, \overline{\chi}_o) P(\xi) d\xi . \quad (6.24)$$

10. Repeat steps 2-9 for the full range of $\overline{\xi}$, ξ_v^2 and $\overline{\chi}$ expected from the LES, in order to construct tables for \overline{Y}_f and \overline{w}_f .

Steps 1-10 represent a fairly lengthy but one-time process. The tables for $\overline{Y}_f(\overline{\xi}, \xi_v^2, \overline{\chi})$ and $\overline{w}_f(\overline{\xi}, \xi_v^2, \overline{\chi})$ will depend on the parameters: $p^{(0)}$, T_{f1} , T_{o2} , T_a , r , Y_{f1} , Y_{o2} , Pe , and Da of the flow to be simulated. Once the tables are constructed, the model may be applied in an LES by using $\overline{\xi}$, ξ_v^2 , and $\overline{\chi}$ at each LES grid point to look up \overline{Y}_f and \overline{w}_f by tri-interpolation. \overline{Y}_o and \overline{Y}_p are linearly related to \overline{Y}_f and $\overline{\xi}$, i.e.,

$$\overline{Y}_o = Y_{o2} (1 - \overline{\xi}) + r (\overline{Y}_f - \overline{\xi} Y_{f1}) \quad (6.25)$$

$$\overline{Y_p} = (r + 1)(Y_{f1}\overline{\xi} - \overline{Y_f}) . \quad (6.26)$$

It is not necessary to model $\overline{w_f}$ if the flow is incompressible. However, if there is density dilatation due to heat release, the chemical and velocity fields are coupled through the source term in the energy equation; in this case, $\overline{w_f}$ must be modeled.

For reacting flows with multi-step chemistry it is often necessary to track multiple chemical species. This is the case, e.g., if a prediction of pollutant formation is being sought. For multi-step chemistry, a laminar flamelet equation may be derived for each species mass fraction. This leads to a series of second-order, ordinary differential equations, coupled through the reaction rate terms. This system of equations may be solved, and the preceding steps followed, to construct tables for each of the chemical species based on $\overline{\xi}$, ξ_v^2 , and $\overline{\chi}$. Then in an LES, all of the chemical species and reaction rates are modeled through table look-ups.

Chapter 7

EVALUATION OF SUBGRID-SCALE CHEMISTRY MODEL

7.1 Filtered DNS Data

Data sets from high resolution, Direct Numerical Simulations of chemically-reacting, turbulent flows were used to investigate the accuracy of the chemistry model. The DNS fields were filtered to obtain exact values for $\overline{Y_f}$, $\overline{Y_o}$, $\overline{Y_p}$, $\overline{w_f}$, $\overline{\xi}$, ξ_v^2 , and $\overline{\chi}$ at each point of a hypothetical LES mesh. The latter three quantities were then used to obtain model values for $\overline{Y_f}$, $\overline{Y_o}$, $\overline{Y_p}$ and $\overline{w_f}$ via trilinear interpolation of the look-up tables. The DNS data are from temporal simulations of isotropic, decaying turbulence. Six cases are presented, denoted by T1, T2, T3, T4, T5, and T6. Cases T1 - T3 were taken from Mell's (128)³ point simulations [62], and cases T4 - T6 were taken from (256)³ point simulations using a spectral code written by V. Nilsen. In all six cases, the DNS fields were filtered onto an LES mesh consisting of 16 X 16 X 16 grid points. Therefore, in cases T1 - T3, each data point in the LES grid represents a box average of 8 X 8 X 8 DNS grid points and in cases T4 - T6, each LES point represents a box average of 16 X 16 X 16 DNS points. Table 7.1 lists the important parameters for each case. In table 7.1, Y_f^o refers to the manner in which the fuel field was initialized, i.e., as frozen or fast chemistry. Δ represents the filter width, i.e., the LES grid spacing. The integral, Taylor and Kolmogorov microscales of the turbulence [92] are denoted by l , λ and η respectively. Quantities in angle brackets, $\langle \rangle$, represent averages over the entire flowfield. ξ_{st} is the stoichiometric value of the mixture-fraction. Sc is the global Schmidt number and Da_t and Re_t are the turbulent Damköhler and Reynolds

Table 7.1: Turbulence and chemistry parameters of filtered DNS data fields.

	T1	T2	T3	T4	T5	T6
Y_f^o	froz	froz	froz	fast	fast	fast
T_a	0	0	0	0	4	8
T_f	1	1	1	8.14	8.14	8.14
Δ/l	0.445	0.366	0.445	0.347	0.347	0.347
Δ/λ	1.33	0.990	1.33	1.59	1.59	1.59
Δ/η	18.5	11.9	18.5	29.8	29.8	29.8
$\langle \xi \rangle$	0.25	0.25	0.25	0.25	0.25	0.25
ξ_{st}	0.25	0.25	0.25	0.25	0.25	0.25
$Sc \equiv \frac{\nu^*}{D^*}$	1.0	1.0	1.0	0.72	0.72	0.72
$Da_t \equiv \frac{K^* l^*}{u_{rms}^*}$	2.1	4.54	8.4	11.2	11.2	11.2
$Re_t \equiv \frac{u_{rms}^* l^*}{\nu^*}$	148	101	148	417	417	417
t_{le}	0.27	1.9	0.27	1.0	1.0	1.0
$\frac{\langle \xi^2 \rangle - \langle \xi \rangle^2}{\langle \xi \rangle - \langle \xi \rangle^2}$	0.824	0.183	0.824	0.533	0.533	0.533

numbers, respectively. In the definitions for Sc , Da_t and Re_t , ν^* is the kinematic viscosity and u_{rms}^* is the root-mean-square of the velocity fluctuations. The rms velocity is computed by averaging over the entire data set. The quantity $\langle \xi \rangle - \langle \xi \rangle^2$ defines the maximum possible value of the global variance $\langle \xi^2 \rangle - \langle \xi \rangle^2$, so that, in the last row of the table, a value of 1 would correspond to completely segregated reactants and a value of 0 would mean that the reactants are completely mixed. Cases T1 and T2 are taken from the same simulation, T1 at 0.27 large-eddy turnover times, and T2 at 1.9 large-eddy turnover times. Case T3 was taken from a simulation with a faster reaction rate. Mell used variable timestepping for cases T1 - T3 and computed the large-eddy turnover time by integrating the instantaneous large-eddy turnover time from the start of the simulation, i.e.,

$$t_{le} = \int_0^t \frac{u_{rms}}{l} d\tau . \quad (7.1)$$

For cases T4 - T6, t_{le} was computed using the initial turnover time, i.e., $t_{le} = u_{rms}^{\circ} t / l^{\circ}$, where a superscript (\circ) denotes a value at $t = 0$.

7.2 Isothermal Turbulence

Figure 7.1 shows the correlation of exact and model values for the fuel, oxidizer and product for case T1. Each point in the plot represents \bar{Y}_i at a particular LES grid point. The plots on the left show the predictions of the Large Eddy Laminar Flamelet Model (LELFM) discussed in the previous Chapter. The plots on the right show the results of assuming frozen (no reaction) and equilibrium (infinite Damköhler number) chemistry. These limits provide a reference for judging the model's performance. In the frozen limit the filtered fuel is $\bar{Y}_f = Y_{f1} \bar{\xi}$, while in the equilibrium limit it is modeled as [16]

$$\frac{\bar{Y}_f}{Y_{f1}} = \int_{\xi_{st}}^1 \left(\frac{\xi - \xi_{st}}{1 - \xi_{st}} \right) \frac{\xi^{a-1} (1 - \xi)^{b-1}}{B(a, b)} d\xi = \frac{a I_{1-\xi_{st}}(b, a+1)}{(a+b)(1-\xi_{st})} - \frac{\xi_{st} I_{1-\xi_{st}}(b, a)}{(1-\xi_{st})} , \quad (7.2)$$

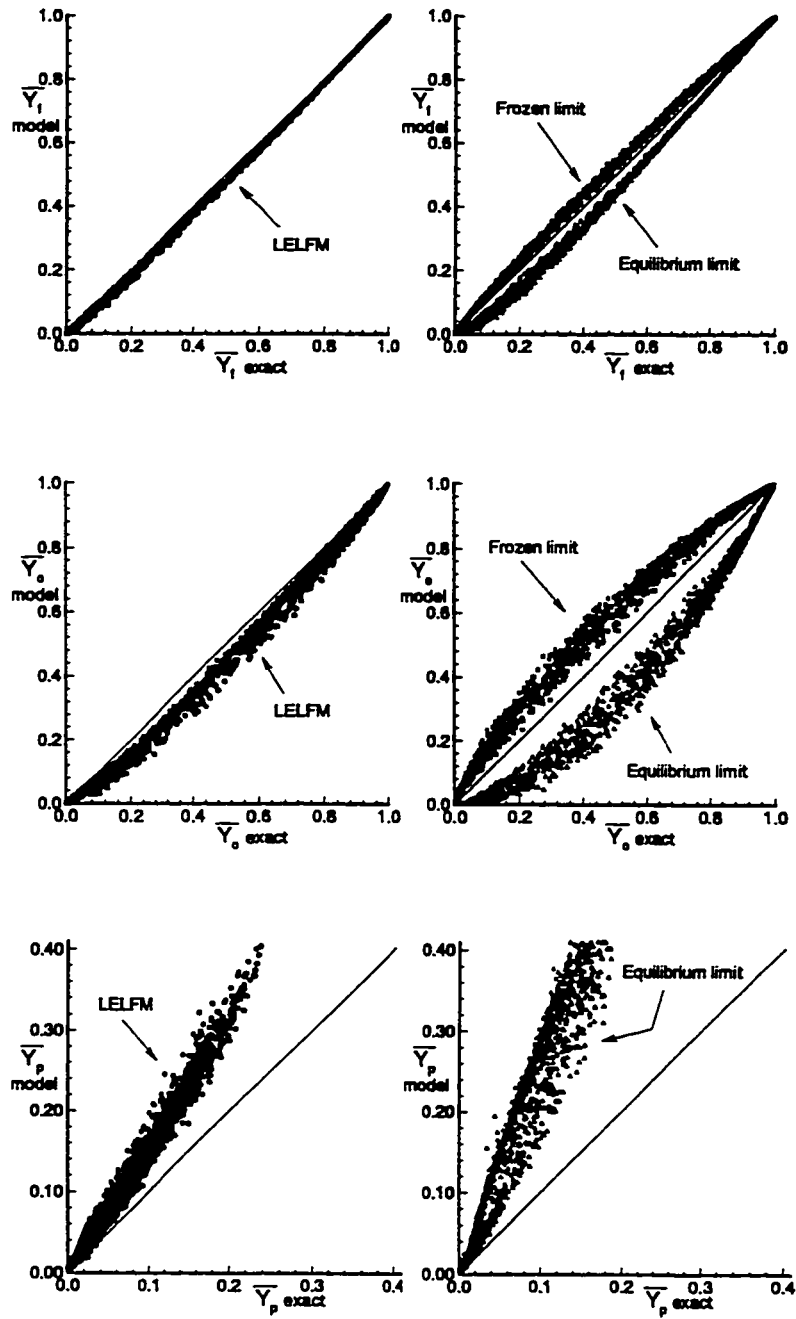


Figure 7.1: Correlation of exact and model species mass-fractions for case T1.

where a and b are given in equation (6.13) and $I_\lambda(\alpha, \beta)$ is the Incomplete beta function. Since $\xi_{st} < 0.5$, the limits for the fuel are closer together than the limits for the oxidizer. Figure 7.2 shows the model's performance at a later time in the same simulation, where the Damköhler number has increased by about a factor of 2. The predictions are significantly improved. Figure 7.3 shows results at the same point in time as case T1, but with a Damköhler number of 8.4. Note the improvement of both the LELFM and the equilibrium predictions.

7.3 The Effect of Arrhenius Kinetics

In cases T4, T5 and T6, D and ρ were kept constant; however, the reaction rate was allowed to vary with temperature according to

$$\dot{w}_f = DaY_fY_o e^{-T_a/T}$$

Cases T4, T5 and T6 are all identical, except for the activation temperature, which was assigned values of 0, 4 and 8 respectively. In order to initiate the reaction, the initial fuel field was set to the equilibrium chemistry prediction. This provided initially high temperatures in thin regions, thus providing a 'spark' for the reaction. The model's predictions for the filtered product mass fraction and reaction rate are shown in Figure 7.4. The Equilibrium Chemistry Limit (ECL) predictions for the product and the Means Closure (MC) predictions for the reaction rate are also shown for comparison. The Means Closure is given by

$$\overline{\dot{w}_f} = Da\overline{Y_f}\overline{Y_o} e^{-T_a/\overline{T}} .$$

The accuracy of the model is quantified by applying a least squares fit to the data in Figure 7.4. The slope of the best-fit line, i.e., m , where $y = mx$, is given in Table 7.2 for $\overline{Y_p}$ and $\overline{\dot{w}_f}$.

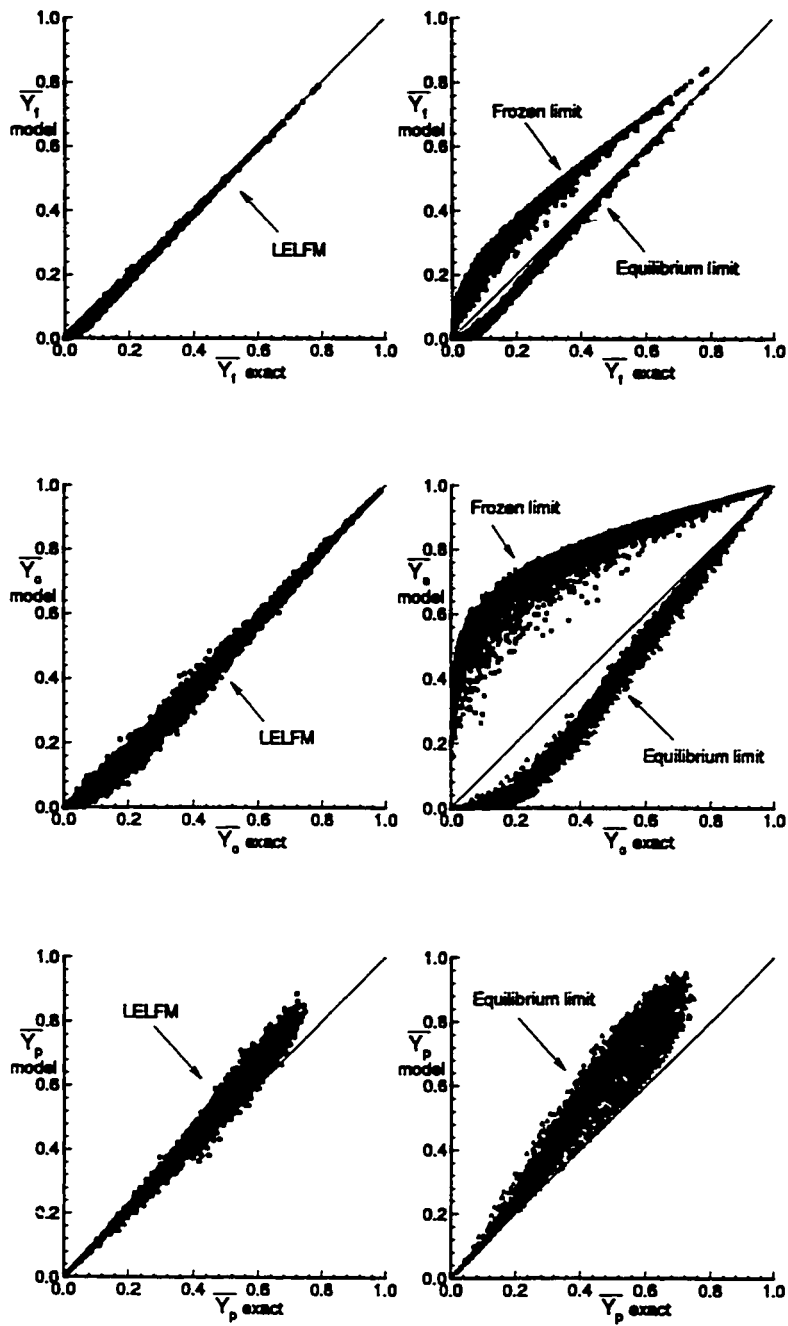


Figure 7.2: Correlation of exact and model species mass-fractions for case T2.

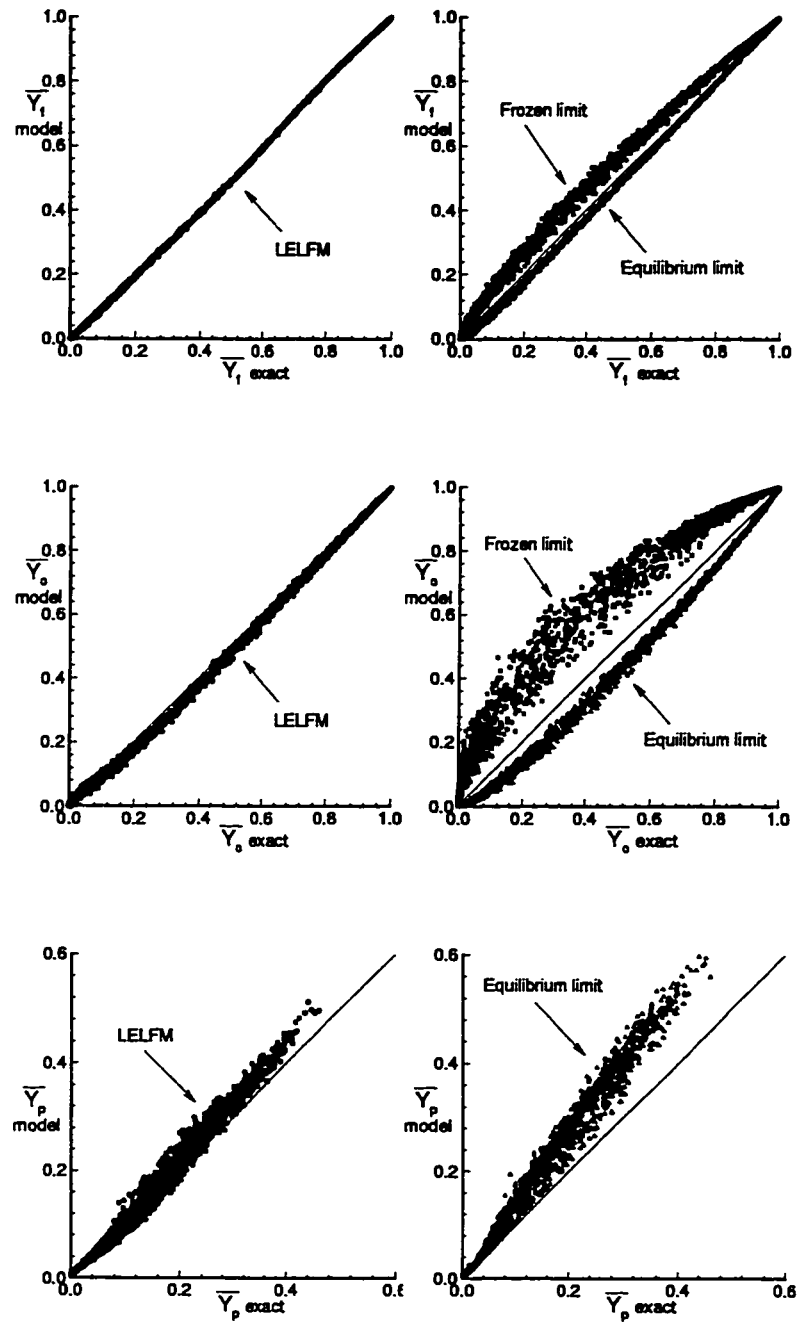


Figure 7.3: Correlation of exact and model species mass-fractions for case T3.

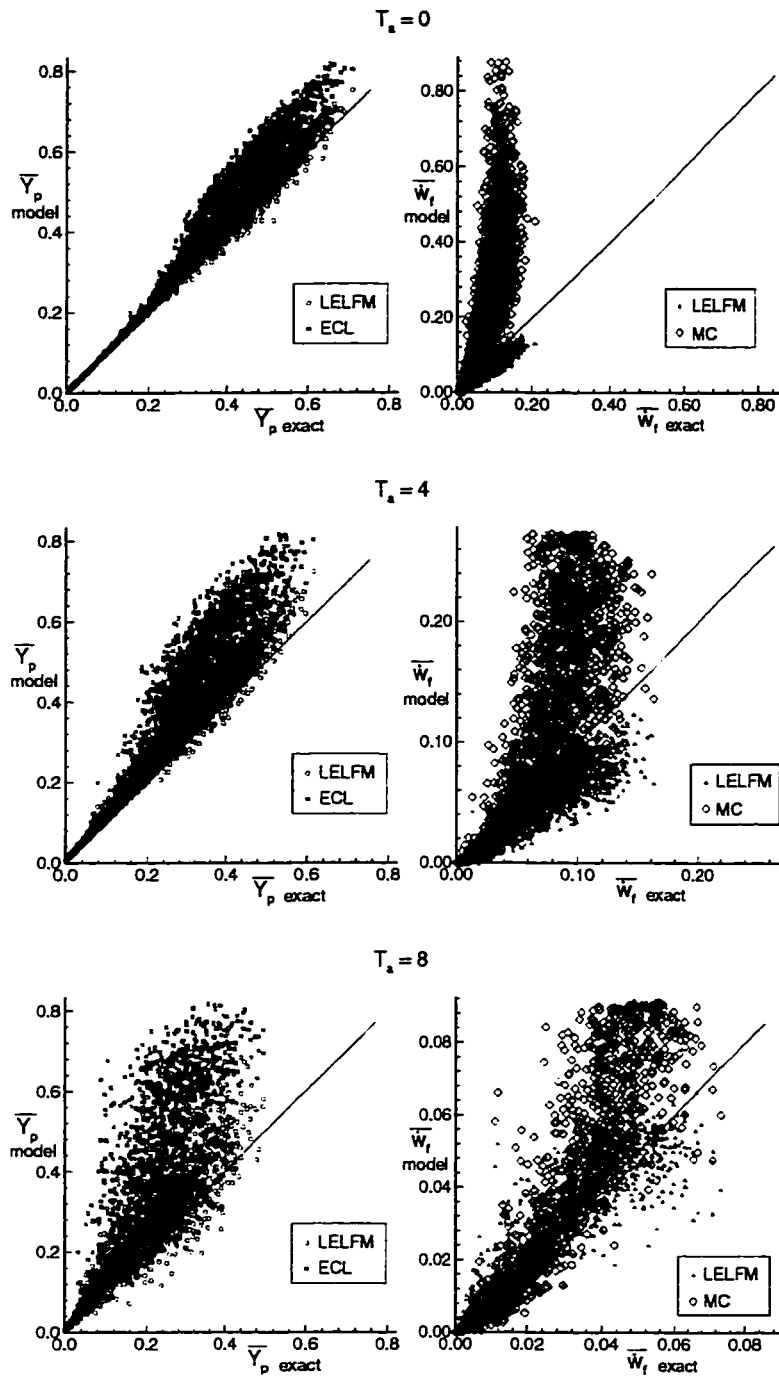


Figure 7.4: Correlation of exact and modeled values for product and reaction rate at various activation temperatures.

Table 7.2: Slope of straight line corresponding to least squares fit of the data for cases T4, T5 and T6.

	$T_a = 0$	$T_a = 4$	$T_a = 8$
\overline{Y}_p LELFM	1.037	1.113	1.145
\overline{Y}_p ECL	1.221	1.438	1.820
\overline{w}_f LELFM	0.770	0.718	0.976
\overline{w}_f MC	3.503	1.804	1.480

Regarding \overline{Y}_p , as T_a is increased, the slope of the ECL prediction increases much more than the slope of the LELFM prediction. The LELFM and MC predictions for \overline{w}_f are seen to improve with increasing T_a . In every case, the LELFM prediction for \overline{w}_f is much better than the MC prediction.

The scatter about the best fit line is defined as

$$\text{scatter} \equiv \frac{1}{N_p} \sum_{i=1}^{N_p} (y_i - mx_i)^2$$

where N_p is the number of data points. The scatter of the data for cases T4, T5 and T6 is listed in Table 7.3.

Table 7.3: Scatter of data about a straight-line fit for cases T4, T5 and T6.

	$T_a = 0$	$T_a = 4$	$T_a = 8$
\overline{Y}_p LELFM	0.289×10^{-3}	0.783×10^{-3}	2.639×10^{-3}
\overline{Y}_p ECL	1.025×10^{-3}	3.504×10^{-3}	10.29×10^{-3}
\overline{w}_f LELFM	9.715×10^{-5}	13.57×10^{-5}	4.121×10^{-5}
\overline{w}_f MC	12.78×10^{-3}	1.897×10^{-3}	0.118×10^{-3}

In an absolute sense, the LELFM prediction for $\overline{Y_p}$ degrades with increasing activation temperature. This may be due to the fact that the reaction rate is slower at higher values of T_a so that the neglect of $\partial Y_f / \partial t$ in (6.1) becomes less valid. However, relative to the ECL prediction, the accuracy of the model appears to improve with increasing T_a . At higher T_a , the reaction zones are narrower, thus the assumption of laminar flamelets should be more valid. The model also appears quite accurate for predicting $\overline{w_f}$ at high activation temperatures, although the low degree of scatter for $\overline{w_f}$ at $T_a = 8$ is partly due to the fact that the reaction rates are much smaller in this case.

The model was also applied to (128)³ Arrhenius-rate fields at a Reynolds number of $Re_t = 135$, with virtually identical results. This suggests that the performance of the model may be insensitive to Reynolds number. In high Reynolds number flows the scalar gradients increase, however, for a given Schmidt number, the scalar diffusivity decreases; thus variations in χ_o within an LES grid cell may not change much with Reynolds number.

7.4 *The Dependence of χ on ξ*

Bray and Peters [7] note that, in recent applications of laminar flamelet modeling, χ has been customarily replaced by its average. Both Bray and Peters [7] and Kuznetsov and Sabel'nikov [44] agree that this procedure is misleading. Indeed, using DNS data of incompressible turbulence with constant scalar diffusivity, it has been found that if χ is replaced in (6.1), either by $\overline{\chi}$ or by $\overline{\chi_{st}} \equiv \overline{\chi_o} F(\xi_{st})$, significant errors result. This is due to the fact that, in reality, χ is zero in regions of pure fuel or oxidizer. If unmixed fuel and/or oxidizer are present in the subgrid-scale volume, then $P(\xi)$ will approach a delta function at 0 and/or 1. Therefore, the integral in (6.14), and hence the modeled value for $\overline{\chi_o}$, will be incorrect unless the assumed form for χ has the properties $\chi(\xi = 0) = \chi(\xi = 1) = 0$.

The success of the counterflow model, as stated in (6.3) with $\xi^- = 0$ and $\xi^+ = 1$, appears to be due to the fact that it accurately predicts the subgrid-scale conditional average of χ for the range of ξ where $P(\xi)$ is large. Using (6.2) and (6.14) the following model is obtained for the conditional dissipation rate,

$$\frac{\overline{\chi|\xi}}{\bar{\chi}} = \frac{F(\xi)}{\int_0^1 F(\xi)P(\xi)d\xi}. \quad (7.3)$$

Figure 7.5 compares $\overline{\chi|\xi}/\bar{\chi}$, computed directly from the DNS data, with $F(\xi)/\int_0^1 F(\xi)P(\xi)d\xi$. Also shown are $P(\xi)$ obtained directly from the data and $P(\xi)$ from the Beta-function model.

The plots on the left hand side are for LES grid cells, taken from case T1, at three different spatial locations. It can be seen that ξ takes on the values of 0 and 1 within the cells, and that $F(\xi)$ and $P(\xi)$ match the DNS data quite well. The plots on the right hand side show results from the same grid cells later in time (case T2). It can be seen that ξ no longer takes on the values of 0 and 1, meaning that $\xi^- > 0$ and $\xi^+ < 1$. The plots show that $F(\xi)$ is reasonably accurate where $P(\xi)$ is large and that $F(\xi)$ overpredicts $\overline{\chi|\xi}$ only where $P(\xi)$ is small. Note that LELFM was found to be more accurate for case T2 than case T1, even though $F(\xi)$ is seen here to be more accurate for case T1 than case T2. These results suggest that, in modeling the ξ dependence of χ , a necessary and sufficient set of boundary conditions are $\chi(\xi = 0) = 0$ and $\chi(\xi = 1) = 0$.

7.5 Sources of Error

There are several possibilities as to why the chemistry model is least accurate for the early stages of mixing: In case T1, there may be some remaining effects of the initialization since Y_f was initially set to the frozen chemistry value. It is also possible that, due to random initialization, the surfaces of constant ξ have not had sufficient time to align orthogonal to the maximum compressive strain axis. Another possibility is that the neglected time derivative in (6.1) is important. If this is the case, then in

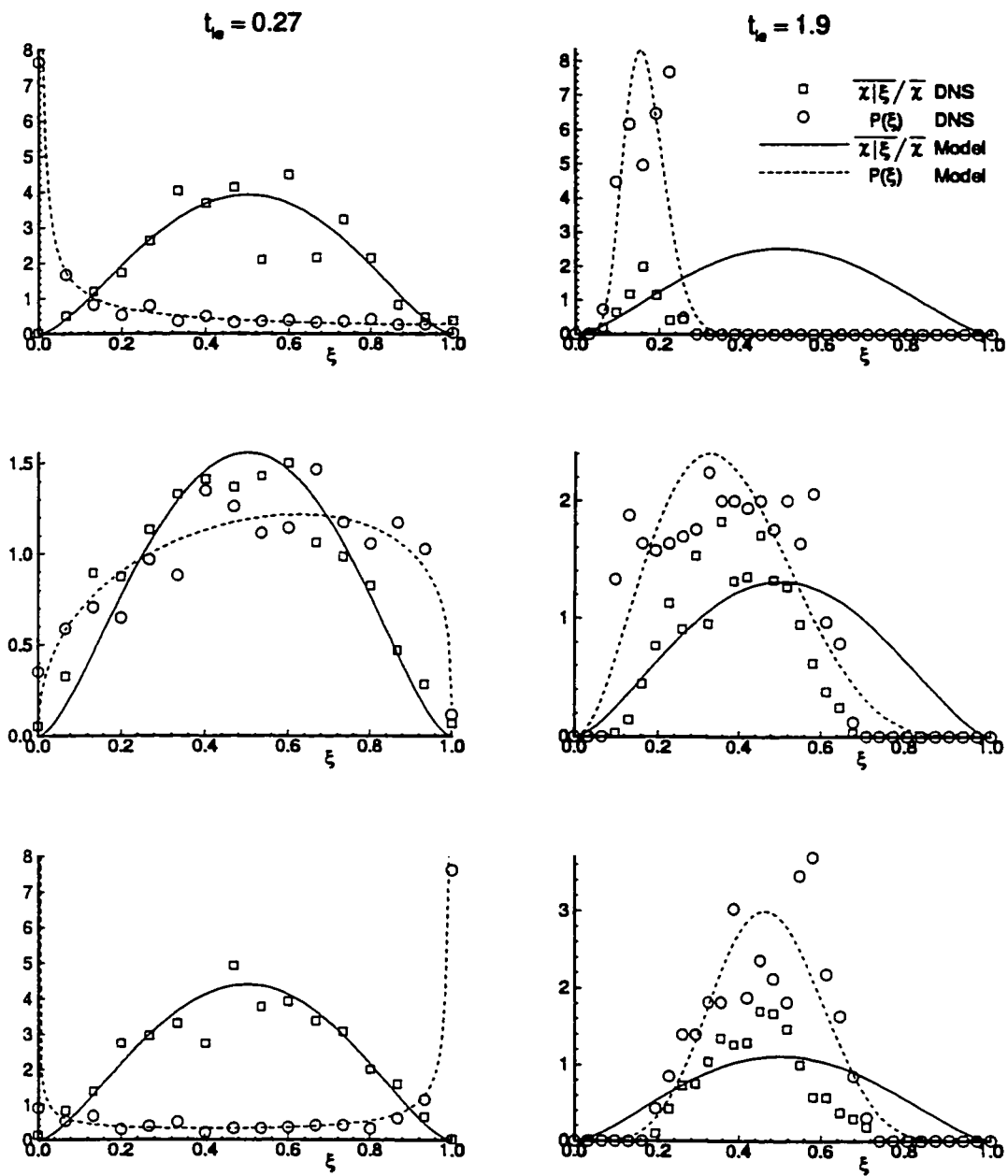


Figure 7.5: Comparison of the counterflow model for χ and the Beta model for the LEPDF with data from DNS cases T1 and T2.

simulating multi-step chemistry, if the reaction sequence involves both fast and slow reactions, the accuracy of the LELFM might be dictated by the slowest reaction. Bish and Dahm [6] have suggested that errors in laminar flamelet theory can be removed at low Da if the probability densities of ξ^- and ξ^+ are taken into account. This seeming contradiction may be due to differences in the flows from which the data are taken. Bish and Dahm examined a small region downstream in a turbulent jet where the unsteady term may be less important, and where the layer-like structure of ξ appears to be more prominent than in the DNS.

Regarding the LELFM prediction for $\overline{Y_p}$, it appears that the slope of the best fit line (Figure 7.4 and Table 7.2) moves toward the exact value of 1.0 as the reaction time is decreased relative to the fluid mixing time. This suggests that the effect of neglecting the time derivative in (6.1) is to move the slope of the best fit line above 1.0. The scatter about the best fit line (Figure 7.4 and Table 7.3) may be partly due to neglect of subgrid-scale fluctuations in χ . Kuznetsov and Sabel'nikov [44] showed that $\overline{Y_i}$ varies like $\chi^{(1/3)}$, which means that (6.11) is a good approximation. However, (6.11) would be expected to be less valid for modeling the reaction rate, since, for isothermal chemistry, $\overline{w_f} \sim \chi^{(2/3)}$. This conclusion seems justified by the DNS data, since the scatter in $\overline{w_f}$ was observed to be greater than the scatter in $\overline{Y_i}$. For Arrhenius-rate chemistry, as T_a is increased the scatter in $\overline{w_f}$ appears to decrease. This may be partly a result of the fact that reaction is occurring in thinner layers, i.e., over a smaller range of χ . It should be noted that if T_a is increased above T_f , then (6.1) becomes very stiff and hence difficult to solve numerically. The stiffness is likely due to nearness to the extinction regime [85].

Some additional scatter occurs if ξ_{st} is either very high or very low. Extreme values of ξ_{st} mean that the integral in (6.12) is essentially determined over a very small range of ξ (e.g., consider the equilibrium curve for Y_o with ξ_{st} very small).

In order to observe this effect, equilibrium values for Y_p were computed from the (256)³ scalar field used in cases T4 - T6, i.e., equilibrium values for the product were computed as

$$Y_p = \begin{cases} (r+1)Y_{f1}\xi & \text{if } \xi \leq \xi_{st} \\ (r+1)Y_{f1}\xi_{st}(1-\xi)/(1-\xi_{st}) & \text{if } \xi > \xi_{st} \end{cases} \quad (7.4)$$

Y_p was then filtered to obtain exact values for $\overline{Y_p}$. Modeled values were computed in the same manner as (7.2), i.e., by integrating (7.4) with the Beta-PDF (6.13), resulting in,

$$\overline{Y_p} = (r+1)Y_{f1}\xi_{st} \frac{I_{\xi_{st}}(a+1, b)}{\xi_{st}} \left[\frac{a}{a+b} \right] + \frac{I_{1-\xi_{st}}(b+1, a)}{1-\xi_{st}} \left[\frac{b}{a+b} \right]. \quad (7.5)$$

Model versus exact values are plotted in Figure 7.6, for equilibrium chemistry, using various values for ξ_{st} .

The value of $\xi_{st} = 0.0476$ corresponds to methane-air combustion and the value of $\xi_{st} = 0.0244$ corresponds to hydrogen-air combustion. The plots show that the correlation decreases as ξ_{st} becomes very low; however, the methane-air and hydrogen-air cases look quite reasonable. Therefore, the equilibrium and LELFM models should be applicable to 'real' combustion, albeit with some degradation of accuracy for reactions with a very low ξ_{st} .

Regarding the assumption of equal diffusivities of all species; Kerstein has suggested that the importance of differential diffusion goes like $Re^{(1/4)}$ and that it therefore may need to be considered, even at high Reynolds numbers. Hence, it may be necessary to apply a correction to the model for reactions involving hydrogen or some other fast-diffusing species [45].

Regarding flows with a high enthalpy of combustion; if the exothermicity causes very large density variations at small scales, then the test 'window' of the dynamic model may contain insufficient information for modeling the subgrid stress tensor

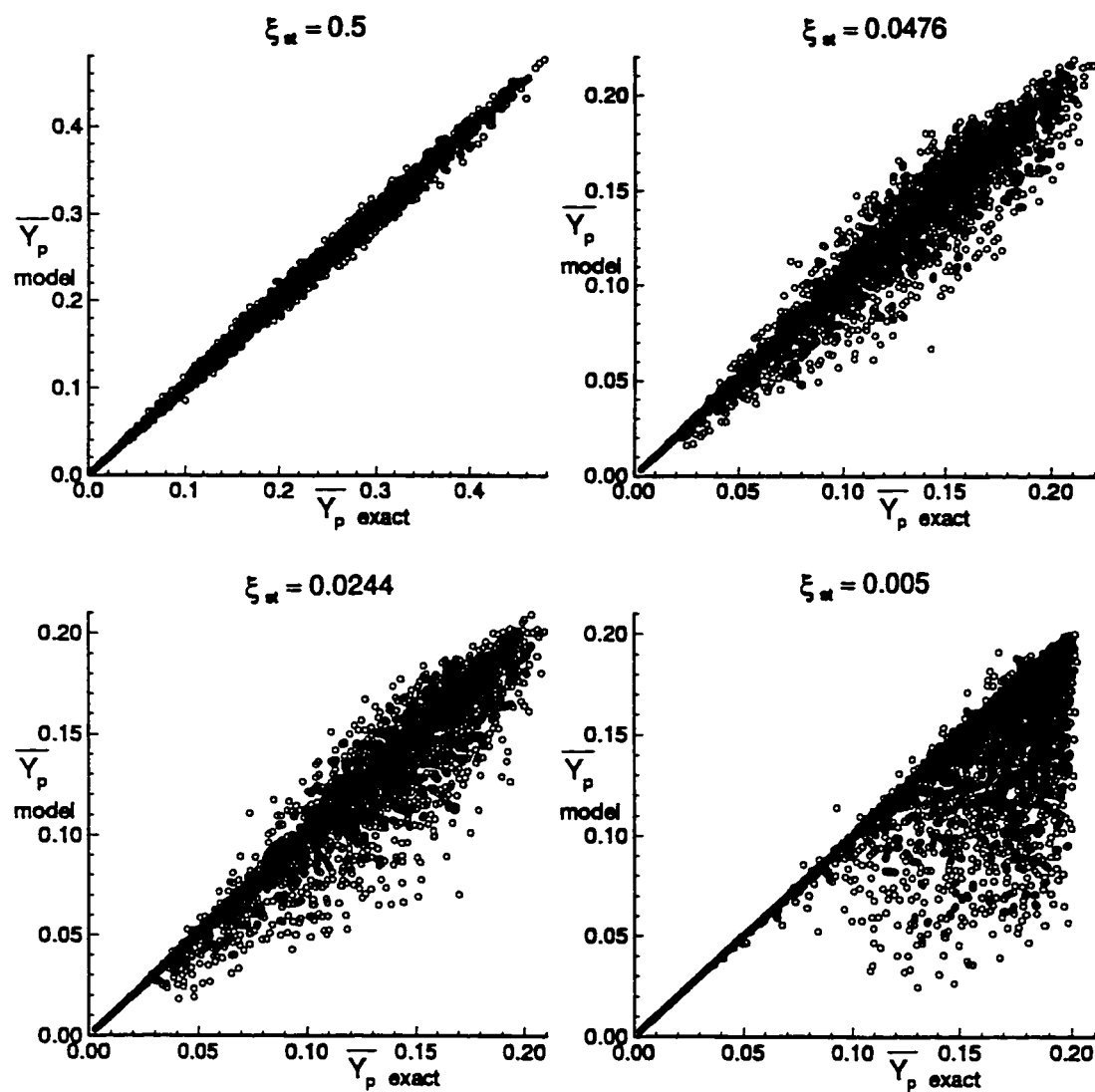


Figure 7.6: Performance of equilibrium chemistry model at various stoichiometries.

and related terms. Furthermore, density dilatation can cause errors in the models for the filtered reaction rates to propagate through to the velocity fields. These effects however, should only be a concern if density variations are very large, since Part I of this thesis demonstrated that moderate changes in density have little effect on the velocity statistics.

Chapter 8

CONCLUSIONS

8.1 Plume Simulations

Part I of this thesis established a methodology for simulating a reactive plume in spatially developing, grid turbulence. By applying a low Mach number approximation to the fully compressible Navier-Stokes equations, the computing time needed to integrate the governing equations is reduced by roughly a factor of $1/M$. A high degree of parallel efficiency was achieved by decomposing the three-dimensional computational domain into planar sections. The Compact scheme for computing spatial derivatives is a good alternative to spectral methods when the boundaries are nonperiodic. The global nature of the Compact scheme makes it sensitive to the boundary conditions. For the turbulent inflow and outflow boundaries of the simulation, a fifth-order Compact boundary scheme was developed and found to be stable. In solving the pressure Poisson equation, a second-order approximation to the density time derivative was found to be significantly more stable (allowing larger density variations) than a third-order approximation. The third-order Adams-Bashforth timestepping algorithm was found to be stable for maximum density changes up to about a factor of 3. For higher density ratios, a predictor-corrector or Runge-Kutta method should be used [69].

The technique of introducing mature turbulence at the inlet removes the need for a lengthy computational region in which turbulence must develop. Since the inlet turbulence is specified by scanning through an existing three-dimensional turbulent field, the interpolation between grid points (of the inlet field) can affect the solution.

Linear interpolation was found to be unacceptable since it results in discontinuous velocity derivatives, thereby causing the pressure term in the mechanical energy equation to oscillate. Cubic-spline interpolation produces inlet velocities with continuous derivatives and was found to help stabilize the calculation. A one-dimensional advective exit condition for the primitive variables, along with a Neumann/Dirichlet pressure condition at the inflow/outflow boundaries, was found to work well. The open nature of the streamwise boundaries allows for global expansion of the fluid due to chemical heat release. This allows the thermodynamic pressure (but not the dynamic pressure) to be assumed constant, which is the case in combustors vented to the atmosphere.

For the incompressible simulation, the downstream growth of Taylor microscales approximately followed the $1/2$ power law predicted from the turbulence energy budget. The decay of turbulent kinetic energy roughly followed the 1.25 empirical power law reported by Comte-Bellot and Corrsin. The centerline decay of mixture-fraction was in fair agreement with a -1 power law reported by Brown and Bilger. The centerline decay of the scalar rms also agreed with Brown and Bilger's reported 1.32 power law, albeit with a larger error bound. Furthermore, the spread of the plume agreed quite closely with a $1/2$ power law predicted from self similarity. The density dilatation in the exothermic simulations was seen to have little effect on the velocity statistics. Increasing the activation temperature moved the reaction toward the frozen limit as expected.

Resolution requirements of DNS restrict the range of turbulence and chemistry parameters that can be achieved; however, much of the important physics observed in experiments of grid turbulence was also observed here. Regarding the chemistry, it is doubtful whether DNS can be used to compute turbulent reacting flows with very low values of ξ_{st} , e.g., as with methane-air combustion. The primary purpose of DNS,

however, is to investigate the physics of turbulent flows so as to gain understanding that may be used to improve the turbulence models of engineering codes. In this context, the methodology presented herein may be considered as an additional tool for investigating the physics of turbulent reacting flows in open domains.

8.2 Chemistry Model for LES

Part II of this thesis described how to apply LES to non-premixed, turbulent, reacting flows. The newly derived chemistry model is based on laminar flamelet theory, and relies on presumed forms for the Large Eddy Probability Density Function and dissipation rate of a conserved scalar. The model predicts filtered chemical species and reaction rates given a filtered scalar, its subgrid-scale variance and dissipation rate. The model is employed by constructing tables for \bar{Y}_i and, if necessary, \bar{w}_f prior to running an LES.

For turbulent flows with finite-rate chemistry, the predictions of the model are substantially more accurate than what would be obtained by assuming equilibrium chemistry. The error in the model tends toward the equilibrium limit and the accuracy improves with increasing Damköhler number. Increasing the activation temperature increases the accuracy of the model relative to the equilibrium prediction. The assumed Beta-distribution for $P(\xi)$ and laminar counterflow form of χ were found to work well. Furthermore, in the counterflow model for χ , it was demonstrated that it is acceptable to choose ξ^- and ξ^+ as 0 and 1 respectively. This is equivalent to assuming that unmixed fuel and oxidizer are present in all LES grid cells. Finally, it was shown that the Beta-PDF is adequate for modeling reactions with very low values of ξ_{st} , but that errors in the model increase as ξ_{st} approaches zero. The chemistry model should be applicable to many common reactions, e.g., methane-air combustion.

8.3 Future Work

The chemistry model presented in Part II of this thesis was evaluated using exact values for $\bar{\xi}$, ξ_v^2 and $\bar{\chi}$. Future research should be aimed at determining the best methods for modeling ξ_v^2 and $\bar{\chi}$. *A priori* tests should be performed to evaluate the correlation between exact and modeled values for ξ_v^2 , using both scale similarity [16] and dynamic modeling, i.e., (6.15). The tests should utilize very high resolution DNS data, i.e., at least $(256)^3$ data points. *A posteriori* tests should be performed to determine if greater accuracy may be obtained by integrating (6.16) to obtain $\bar{\xi}^2$. DNS data should also be used to further investigate Girimaji and Zhou's model [35], i.e., (6.20), (6.21) and (6.22) for $\bar{\chi}$. It should be determined whether their model provides better correlation with DNS data than does Schmidt and Schumann's model [87], i.e., (6.19).

Once the best ways of modeling ξ_v^2 and $\bar{\chi}$ have been determined, an appropriate set of experimental data should be sought out, for the purpose of comparing with an LES. The experimental data should be for low Mach number combustion in an open domain, so that density and temperature can be eliminated as parameters in the chemistry model. The experimental flow should also be in a regime where differential diffusion and radiative heat transfer are negligible. The chemistry may involve multiple species undergoing multiple reactions; however, as the number of chemical species increases, the amount of effort required to construct the flamelet libraries also increases. If the chemistry involves very slow reactions, it may be possible to apply an empirical correction to the model in order to accurately predict the slowest forming species. A correction could also be applied to improve the prediction during the early stages of mixing, e.g., near the nozzle of a jet.

The model may be extended to flows at high Mach number with radiative heat transfer and to flows in closed domains, e.g., internal combustion engines. In these

cases however, extra expenses arise since density and temperature appear as additional parameters, thus making the model tables five-dimensional rather than three-dimensional. Furthermore, if the unity Lewis number assumption cannot be made, then subgrid-scale temperature fluctuations may need to be accounted for explicitly. Also, the importance of small scale temperature fluctuations, e.g., the bracketed term in (5.18), should be investigated for various levels of heat release, in order to determine the range of q for which (5.21), (5.22), (5.23) and (6.16) are valid.

BIBLIOGRAPHY

- [1] Anderson, D. A., Tannehill, J. C. and Pletcher, R. H., *Computational Fluid Mechanics and Heat Transfer*, (Hemisphere, 1984).
- [2] Antonopoulos-Domis, M., "Large-eddy simulation of a passive scalar in isotropic turbulence," *J. Fluid Mech.* **104**, 55-79 (1981).
- [3] Bardina, J., Ferziger, J. H., and Reynolds, W. C., "Improved subgrid scale models for large eddy simulation," *AIAA Paper*, 80-1357 (1980).
- [4] Bilger, R. W., "Turbulent flows with nonpremixed reactants," in *Topics in Applied Physics*, Vol. 44, Ch. 3, edited by P. A. Libby and F. A. Williams (Springer-Verlag, Berlin, 1980).
- [5] Bilger, R. W., "Conditional moment closure for turbulent reacting flow," *Phys. Fluids A* **5**, 436 (1993).
- [6] Bish, E. S. and Dahm, W. J. A. "Strained dissipation and reaction layer analyses of nonequilibrium chemistry in turbulent reacting flows," *Combust. Flame* **100**, 457 (1995).
- [7] Bray, K. N. C. and Peters, N., "Laminar flamelets in turbulent flames," in *Turbulent Reacting Flows*, edited by P. A. Libby and F. A. Williams (Academic Press, London, 1994), p. 63-113.
- [8] Brown, R. J. and Bilger, R. W., "An experimental study of a reactive plume in grid turbulence," *J. Fluid Mech.* **312**, 373-407 (1996).

- [9] Brown, R. J. *Private Communication*, (1995).
- [10] Buell, J. C. and Huerre, P., "Inflow/Outflow Boundary Conditions and Global Dynamics of Spatial Mixing Layers," *CTR Proceedings of the Summer Program*, (1988).
- [11] Buell, J. C., "A Hybrid Numerical Method for Three-Dimensional Spatially-Developing Free-Shear Flows," *J. Comput. Phys.* **95**, 313-338 (1991).
- [12] Carati, D., Jansen, K., and Lund, T., "A family of dynamic models for large-eddy simulation," *Center for Turbulence Research, Annual Research Briefs* 35-40 (Dec. 1995).
- [13] Chen, J. H., Mahalingam, S., Puri, I. K. and Vervish, L., "Effect of finite-rate chemistry and unequal Schmidt numbers on turbulent non-premixed flames modeled with single-step chemistry," Presented at the WSS/CI Fall Meeting, Berkeley, California, October 12, (1992).
- [14] Chorin, A. J., "A Numerical Method for Solving Incompressible Viscous Flow Problems," *J. Comput. Phys.* **2**, 12-26 (1967).
- [15] Comte-Bellot, G. and Corrsin, S., "Simple Eulerian time correlation of full- and narrow-band velocity signals in grid-generated, 'isotropic' turbulence," *J. Fluid Mech.* **48**, 273-337 (1971).
- [16] Cook, A. W. and Riley, J. J., "A subgrid model for equilibrium chemistry in turbulent flows," *Phys. Fluids A* **6**, 2868-2870 (1994).
- [17] Cook, A. W., and Riley, J. J., "Direct Numerical Simulation of a Turbulent Reactive Plume on a Parallel Computer," *J. Comput. Phys.*, In Press.

- [18] Cook, A. W., Riley, J. J., and Kosály, G., "A laminar flamelet approach to subgrid-scale chemistry in turbulent flows," *Combustion and Flame*, In Press.
- [19] Corrsin, S., "Turbulence: Experimental Methods," *Handbuch der Physik* Vol. VIII/2, edited by C. Truesdell (Springer-Verlag, 1963).
- [20] Dahm, W. J. A., Southerland, K. B. and Buch, K. A., "Direct, high-resolution, four-dimensional measurements of the fine scale structure of $Sc \gg 1$ molecular mixing in turbulent flows," *Phys. Fluids A* **3**, 1115-1127 (1991).
- [21] Deardorff, J. W., "A numerical study of three-dimensional turbulent channel flow at large reynolds numbers," *J. Fluid Mech.* **41**, 453 (1970).
- [22] Deardorff, J. W., "Three-dimensional numerical study of the height and mean structure of a heated planetary boundary layer," *Bound. Lay. Met.* **71**, 81 (1974).
- [23] Dongarra, J. J., "Performance of Various Computers Using Standard Linear Equations Software," Report no. CS - 89 - 85, Computer Science Department, University of Tennessee and Mathematical Sciences Section, Oak Ridge National Laboratory, (31 January 1994).
- [24] Durran, D. R., "The third-order Adams-Bashforth method: an attractive alternative to leapfrog time differencing," *Monthly Weather Review* **119**, No. 3, (March 1991).
- [25] Durran, D. R., Yang, M.-J., Slinn, D. N. and Brown, R. G., "Toward more accurate wave-permeable boundary conditions," *Monthly Weather Review* **121**, No. 2, (February 1993).
- [26] Erlebacher, G., Hussaini, M. Y., Speziale, C. G., and Zang, T. A., ICASE Report 90-76, ICASE/NASA Langley Research Center, (1990).

- [27] Ferziger, J. H., "Subgrid-Scale Modeling," in *Large Eddy Simulation of Complex Engineering and Geophysical Flows*, edited by B. Galperin, and S. A. Orszag (Cambridge University Press, 1993), p. 37-54.
- [28] Frankel, S. H., V. Adumitroaie, C. K. Madnia, and P. Givi, "Large-eddy simulation of turbulent reacting flows by assumed pdf methods," *Engineering Applications of Large Eddy Simulations (ASME Fluids Engineering Division)* **126**, 81-101 (1993).
- [29] Friedrich, R. and Arnal, M., "Analyzing turbulent backward-facing step flow with the lowpass-filtered Navier-Stokes equations," *J. Wind Eng. Ind. Aerodyn.* **35**, 101-128 (1990).
- [30] Gad-El-Hak, M. and Morton, J. B., "Experiments on the diffusion of smoke in isotropic turbulent flow," *AIAA J.* **12**, 558-562 (1979).
- [31] Gao, F. and O'Brien, E. E., "A large-eddy simulation scheme for turbulent reacting flows," *Phys. Fluids A* **5**, 1282 (1993).
- [32] Germano, M., Piomelli, U., Moin, P., and Cabot, W., "A dynamic subgrid-scale eddy-viscosity model," *Phys. Fluids A* **3**, 1760 (1991).
- [33] Germano, M., "Turbulence: the filtering approach," *J. Fluid Mech.* **238**, 325 (1992).
- [34] Ghaddar, N. K., Karniadakis, G. E. and Patera, A. T., "A Conservative Isoparametric Spectral Element Method for Forced Convection: Application to Fully Developed and Periodic Geometries," *Numerical Heat Transfer* **9**, 277-300 (1986).
- [35] Girimaji, S. S. and Zhou, Y., "Analysis and modeling of subrid scalar mixing using numerical data," *Phys Fluids A* **8**, 1224-1236 (1996).

- [36] Givi, P., Jou, W.-H. and Metcalfe, R. W., "Flame Extinction in a Temporally Developing Mixing Layer," *Proceedings of the 21st Symposium (International) on Combustion*, The Combustion Institute, Pittsburgh, PA, (1986).
- [37] Gresho, P. M., "On the theory of semi-implicit projection methods for viscous incompressible flow and its implementation via a finite element method that also introduces a nearly consistent mass matrix. Part1: Theory," *International Journal for Numerical Methods in Fluids* **11**, 587-620 (1990).
- [38] Grinstein, F. F., "Open boundary conditions in the simulation of subsonic turbulent shear flows," *J. Comput. Phys.* **115**, 43 (1994).
- [39] Haidvogel, D. B., Robinson, A. R. and Schulman, E. D., "The Accuracy, Efficiency, and Stability of Three Numerical Models with Application to Open Ocean Problems," *J. Comput. Phys.* **34**, 1 (1980).
- [40] Jou, W. H. and Riley, J. J., "Progress in direct numerical simulations of turbulent, reacting flows," *AIAA J.* **27**, (11), 1543 (1989).
- [41] Kerstein, A. R., "Linear-eddy model of turbulent scalar transport and mixing," *Comb. Sci. Tech.* **60**, 391-421 (1988).
- [42] Komori, S. and Ueda, H., "Turbulent effects on the chemical reaction for a jet in a nonturbulent stream and for a plume in a grid-generated turbulence," *Phys. Fluids A* **27**, 77-86 (1984).
- [43] Korczak, K. Z. and Patera, A. T., "An Isoparametric Spectral Element Method for Solution of the Navier-Stokes Equations in Complex Geometry," *J. Comput. Phys.* **62**, 361-382 (1986).

- [44] Kuznetsov, V. R., and Sabel'nikov, V. A., "Turbulence and Combustion," in *Combustion: An International Series*, edited by Norman Chigier (Hemisphere Publishing Corp. 1990).
- [45] Lentini, D., "Assessment of The Stretched Laminar Flamelet Approach For Non-premixed Turbulent Combustion," *Combust. Sci. and Tech.* **100**, 95-122 (1994).
- [46] Leonard, A. D. and Hill, J. C., "A Simple Chemical Reaction in Numerically Simulated Homogeneous Turbulence," AIAA Paper 87-0134, (Jan. 1987).
- [47] Le, H. and Moin, P., "Direct numerical simulation of turbulent flow over a backward-facing step," Stanford Report No. TF-58, (December 1994).
- [48] Lee, S., Lele, S. K. and Moin, P., "Eddy shocklets in decaying compressible turbulence," *Phys. Fluids A* **3**, 657-664 (1991).
- [49] Lee, S., Lele, S. K. and Moin, P., "Simulation of spatially evolving turbulence and the applicability of Taylor's hypothesis in compressible flow," *Phys. Fluids A* **4**, 1521-1530 (1992).
- [50] Lele, S. K., "Compact finite difference schemes with spectral-like resolution," *J. Comput. Phys.* **103**, 16-42 (1992).
- [51] Libby, P. A. and Williams, F. A., "Turbulent Reacting Flows," in *Topics in Applied Physics*, Vol. 44, Ch. 1, edited by P. A. Libby and F. A. Williams (Springer-Verlag, Berlin, 1980).
- [52] Lilly, D. K., "On the Application of the Eddy Viscosity concept in the inertial subrange of turbulence," National Center for Atmospheric Research, Boulder, CO., Manuscript 123, (1966).

- [53] Lilly, D. K., "A proposed modification of the Germano subgrid-scale closure method," *Phys. Fluids A* **4**, 633-635 (1992).
- [54] Liñán, A., "The asymptotic structure of counterflow diffusion flames for large activation energies," *Acta Astronautica* **1**, 1007-1039 (1974).
- [55] Liu, S., Meneveau, C., and Katz, J., "On the properties of similarity subgrid-scale models as deduced from measurements in a turbulent jet," *J. Fluid Mech.* **275**, 83-119 (1994).
- [56] Lowery, P. S. and Reynolds, W. C., "Numerical simulation of a spatially-developing, forced plane mixing layer," Stanford Report No. TF-26, (September 1986).
- [57] Madnia, C. K., and Givi, P., "Direct Numerical Simulation and Large Eddy Simulation of Reacting Homogeneous Turbulence," in *Large Eddy Simulation of Complex Engineering and Geophysical Flows*, edited by B. Galperin, and S. A. Orszag (Cambridge University Press, 1993), p. 315-346.
- [58] Mansour, N. N., Moin, P., Ferziger, J. H., and Reynolds, W. C., in *Turbulent Shear Flows I*, edited by F. Durst, B. E. Launder, F. W. Schmidt, and J. H. Whitelaw (Springer-Verlag, Berlin, 1979), p. 386-401.
- [59] McMurtry, P. A., Jou, W.-H., Riley, J. J. and Metcalfe, R. W., "Direct Numerical Simulations of a Reacting Mixing Layer with Chemical Heat Release," *AIAA J.* **24**, No. 6, 962 (1986).
- [60] McMurtry, P. A., Menon, S. and Kerstein, A. R., "A linear eddy sub-grid model for turbulent reacting flows: applications to hydrogen-air combustion," *Proceedings of the 24th International Symposium on Combustion*, p. 271-278, (The Combustion Institute, Pittsburg, (1992).

- [61] Mell, W. E., Nilsen, V., Kosály, G. and Riley, J. J., "Direct numerical simulation investigation of the conditional moment closure model for nonpremixed turbulent reacting flows," *Comb. Sci. Tech.* **91**, 179 (1993).
- [62] Mell, W. E., Kosály, G. and Riley, J. J., "Investigation of closure models for nonpremixed turbulent reacting flows," *Phys. Fluids A* **6**, 1331 (1994).
- [63] Meneveau, C., Lund, T. S., and Cabot, W., "A Lagrangian dynamic subgrid-scale model of turbulence," *Proceedings of the 1994 Summer Program*, Center for Turbulence Research, 271-299 (1994).
- [64] Menon, S., McMurtry, P. A., and Kerstein, A. R., "A Linear-Eddy Mixing Model for Large Eddy Simulation of Reacting Homogeneous Turbulence," in *Large Eddy Simulations of Complex Engineering and Geophysical Flows* edited by B. Galperin, and S. Orszag (Cambridge University Press 1993), p. 287-314.
- [65] Mickelsen, W. R., "Measurements of the effect of molecular diffusivity in turbulent diffusion," *J. Fluid Mech.* **1**, 397-400 (1960).
- [66] Moin, P. and Kim, J., "Numerical investigations of turbulent channel flow," *J. Fluid Mech.* **118**, 341 (1982).
- [67] Moin, P., Squires, K., Cabot, W. and Lee, S., "A dynamic subgrid-scale model for compressible turbulence and scalar transport," *Phys. Fluids A* **3**, 2746 (1991).
- [68] Montgomery, C. J., Kosály, G. and Riley, J. J., "Direct numerical simulation of turbulent reacting flow using a reduced hydrogen-oxygen mechanism," *Combustion and Flame* **95**, 247 (1993).
- [69] Najm, H. N., "A predictor-corrector projection method for modeling low Mach number reacting flow," Submitted to *AIAA J.*, (1996).

- [70] Nakamura, I., Sakai, Y. and Miyata, M., "Diffusion of matter by a non-buoyant plume in grid-generated turbulence," *J. Fluid Mech.* **178**, 379-403 (1987).
- [71] Nomura, K. K. and Elghobashi, S. E., "Mixing characteristics of an inhomogeneous scalar in isotropic and homogeneous sheared turbulence," *Phy. Fluids A* **4**, 606 (1992).
- [72] Nomura, K. K. and Elghobashi, S. E., "The structure of inhomogeneous turbulence in variable density nonpremixed flames," *Theoret. Comput. Fluid Dynamics* **5**, 153-175 (1993).
- [73] Peters, N., "Laminar diffusion flamelet models in non-premixed turbulent combustion," *Prog. in Energy and Comb. Sci.* **10**, 319-339 (1984).
- [74] Peyret, P. and Taylor, T. D., *Computational Methods for Fluid Flows*, Springer-Verlag, (1983).
- [75] Piomelli, U. and Liu, J., "Large-eddy simulation of rotating channel flows using a localized dynamic model," *Phys. Fluids* **7**, 839-848 (1995).
- [76] Poinso, T. J. and Lele, S. K., "Boundary conditions for direct simulations of compressible viscous flows," *J. Comput. Phys.* **101**, 104-129 (1992).
- [77] Pope, S. B., "Computations of turbulent combustion: progress and challenges," *Prog. Energy Comb. Sci.* **11**, 119 (1985).
- [78] Press, W. H., Flannery, B. P., Teukolsky, S. A. and Vetterling, W. T., *Numerical Recipes*, (Cambridge, 1989).
- [79] Prosser, R., *Private Communication*, (1996).

- [80] Ragab, S. A. and Sheen, S.-C., "Large Eddy Simulation of Mixing Layers," in *Large Eddy Simulation of Complex Engineering and Geophysical Flows*, edited by B. Galperin, and S. A. Orszag (Cambridge University Press, 1993), p. 255-285.
- [81] Réveillon, J. and Vervisch, L., "Response of the dynamic LES model to heat release induced effects," *Phys. Fluids* **8**, (1996).
- [82] Riley, J. J., Metcalfe, R. W. and Orszag, S. A., "Direct numerical simulation of chemically reacting turbulent mixing layers," *Phys. Fluids* **29**, 406 (1986).
- [83] Riley, J. J., *Private Communication*, (1995).
- [84] Rogallo, R. W. and Moin, P., "Numerical simulation of turbulent flows," *Annu. Rev. Fluid Mech.* **16**, 99 (1984).
- [85] Sanders, J. P. H. and Lamers, A. P. G. G., "Modeling and Calculation of Turbulent Lifted Diffusion Flames," *Combustion and Flame* **96**, 22-33 (1994).
- [86] Sandoval, D. L., "The Dynamics of Variable-Density Turbulence," *Ph.D. Thesis*, University of Washington, (1995).
- [87] Schmidt, H. and Schumann, U., "Coherent structure of the convective boundary layer derived from large-eddy simulations," *J. Fluid Mech.* **200**, 511 (1989).
- [88] Schumann, U., "Results of a Numerical Simulation of Turbulent Channel Flows," in *Int'l. Meeting on Reactor Heat Transfer* edited by M. Dalle-Donne (1973), p. 230-251.
- [89] Smagorinsky, J. "Some Historical Remarks on the Use of Nonlinear Viscosities," in *Large Eddy Simulation of Complex Engineering and Geophysical Flows*, edited by B. Galperin, and S. A. Orszag (Cambridge University Press, 1993), p. 2-36.

- [90] Southerland, K. B., and Dahm, W. J. A. Report No. 026779-12, The University of Michigan, Ann Arbor, MI (1994).
- [91] Taylor, G. I., "The spectrum of turbulence," *Proc. R. Soc. London Ser. A* **164**, 476 (1938).
- [92] Tennekes H. and Lumley, J. L., *A First Course in Turbulence*, (MIT Press, Cambridge, 1972).
- [93] Williams, F. A., *Combustion Theory* 2nd ed., (Addison-Wesley, 1985).
- [94] Yee, H. C., "Construction of Explicit and Implicit Symmetric TVD Schemes and Their Applications," *J. Comput. Phys.* **68**, 151-179 (1987).
- [95] Yoshizawa, A., "Statistical theory for compressible turbulent shear flows, with the application to subgrid modeling," *Phys. Fluids* **29**, 2152 (1986).
- [96] Zang, T. A., Drummond, J. P., Erlebacher, G., Speziale, C. and Hussaini, M. Y., "Numerical Simulation of Transition, Compressible Turbulence, and Reacting Flows," AIAA Paper 87-0130, (Jan. 1987).

CURRICULUM VITAE

August 1996

NAME: Andrew William Cook
TITLE: Doctoral Candidate

MAILING ADDRESS: 1077 E. 75 S.
Bountiful, Utah 84010
phone: (801) 295-6800
email: cookaw@cm5.ncsa.uiuc.edu

DATE OF BIRTH: 3 February 1966
PLACE OF BIRTH: Bountiful, Utah USA

EDUCATION:

INSTITUTION	DEGREE	FIELD	DATE	GPA
Univ. of Utah	B.S.	Mech. Eng.	3/90	3.97
	(Magna Cum Laude)			
Univ. of Utah	Minor	Math	3/90	3.97
Univ. of Wash.	M.S.	Mech. Eng.	12/91	3.80
Univ. of Wash.	Ph.D.	Mech. Eng.	8/96	3.78

JOURNAL PUBLICATIONS:

Cook, A. W., and Riley, J. J., "A Subgrid Model for Equilibrium Chemistry in Turbulent Flows," *Physics of Fluids* 6, 2868 (1994).

Cook, A. W., and Riley, J. J., "Direct Numerical Simulation of a Turbulent Reactive Plume on a Parallel Computer," *Journal of Computational Physics*, In press.

Cook, A. W., Riley, J. J., and Kosaly, G., "A Laminar Flamelet Approach to Subgrid-Scale Chemistry in Turbulent Flows," *Combustion and Flame*, In press.

Cook, A. W., and Riley, J. J., "Subgrid-Scale Models for Reacting Large Eddy Simulation," In preparation for *Combustion and Flame*.